Commissioning and Characterization of a GEM Stand for Testing the HVMAPS of the MOLLER Experiment

by

Noel Alberto Cruz Venegas

A Thesis submitted to the
Faculty of Graduate and Postdoctoral Studies
of The University of Manitoba
in partial fulfillment of the requirements of the degree of

MASTER OF SCIENCE

Department of Physics and Astronomy
The University of Manitoba
Winnipeg, Manitoba, Canada
September, 2025

Abstract

Commissioning and Characterization of a GEM Stand for Testing the HVMAPS of the MOLLER Experiment

To search for signs of new neutral currents beyond the Standard Model of Particle Physics, the Measurement Of a Lepton Lepton Electroweak Reaction (MOLLER) experiment aims to make a high-precision measurement of the electroweak mixing angle, $\sin^2\theta_W$, at a momentum transfer squared of $Q^2 = 0.0056$ GeV^2 by determining the parity-violating asymmetry (A_{PV}) in electron-electron (Møller) scattering at 32 ± 0.8 (*ppb*). Achieving this precision requires tracking detectors with excellent spatial resolution and fast readout capabilities. To meet these requirements, the MOLLER experiment plans to employ High Voltage Monolithic Active Pixel Sensors (HVMAPS) in its main integrating detector. To evaluate their spatial resolution, a dedicated test stand has been developed using two identical commercial triple Gas Electron Multiplier (triple-GEM) detectors, which provide high tracking precision and reconstruction accuracy at the micrometer scale. The GEM stand consists of two 10×10 cm^2 active area triple-GEMs, operated in tracking mode with an Ar/CO_2 (80/20) gas mixture at 18 °C and 1 atm. Using the 5.9 keV photopeak from an Fe-55 source and cosmic muons, a common operational voltage range between 3240 V and 3300 V was identified, corresponding to the proportional region of gas amplification. Operation in this region ensures stable GEM stand performance with sufficient gain for reliable signal detection. These results establish the standard operating conditions of the GEM stand and lay the foundation for future measurements of the spatial resolution of HVMAPS, thereby supporting the development of the main integrating detector for the MOLLER experiment.

Dedicated to my family,
for all their love and support

Acknowledgements

I would like to express my gratitude to Dr. Juliette Mammei. I am also deeply grateful to Dr. Sakib Rahman for introducing me to the computing resources available at Compute Canada and Jefferson Lab. My sincere thanks go to Dr. Sean Hansen-Ramu for his assistance in designing and constructing the mechanical and electronic components of the experiment, as well as for providing valuable feedback on my analysis.

I would also like to extend my deepest thanks to the members of my thesis committee, Dr. Michael Gericke and Dr. Gerald Gwinner, for their time spent reading this thesis, and for their insightful comments and corrections on the first draft of this work.

I would also like to acknowledge Michal Babij, and Piotr Bielowka from Techtra® company, for their patience and guidance while I was learning about the triple-GEM technology. Their help and resources were instrumental in advancing my work.

I am thankful to the University of Manitoba's Department of Physics, the local MOLLER group, and the MOLLER Collaboration for providing me with numerous opportunities to grow as a scientist during my studies.

Finally, but by no means least, I wish to thank my parents, family, and friends for their unwavering support and love throughout my journey in Winnipeg, through both the ups and downs.

Statement of Originality

I certify that this thesis was composed entirely by myself and that the work presented herein is my own, except where explicitly stated otherwise. All figures and data are original unless otherwise indicated.

I declare that this work has not been submitted for any other degree or professional qualification, except as explicitly specified.

Contribution of Authors

This thesis is a single-authored work. My main contribution to this work was the commissioning of the Gas Electron Multiplier (GEM) stand, consisting of two triple-GEMs. I was responsible for the experimental design, including the soldering of the electronic components from one of the high-voltage dividers for one of the triple-GEM. I also participated in the wiring, gas piping, and the development of the instrumentation diagram for the GEM stand. This work was carried out within the local MOLLER group at the University of Manitoba and was developed in the context of the MOLLER experiment.

The black box on which the triple-GEMs are mounted, along with the associated gas panel, was previously constructed by Dr. Sakib Rahman.

I conducted the characterization and data analysis of the triple-GEM' response to cosmic muons and Fe-55 X-rays. For data processing and figure generation, I employed Python and various freely available libraries and packages: `PIL`, `pytesseract`, `sklearn`, `seaborn`, `os`, `re`, `landaupy`, `numpy`, `scipy`, `matplotlib`, and `pandas`. I developed the algorithm for data processing, ensured data quality, and contributed to the implementation of the Density-Based Spatial Clustering of Applications with Noise (DBSCAN) algorithm used for defining events corresponding to sparks, cosmic muons, and 5.9 keV X-ray interactions. The activities described here directly supported detector development and commissioning efforts for the MOLLER experiment.

This document was prepared using the LaTeX typesetting system and compiled using the cloud-based Overleaf editor (free version).

Contents

List of Tables

List of Figures

Chapter 1

Introduction

The Measurement of a Lepton-Lepton Electroweak Reaction (MOLLER) experiment is designed to be a precision test of the electroweak theory of the Standard Model of Particle Physics. This experiment aims to make a low energy determination of the mixing angle ($\sin^2\theta_W$) with 0.1% uncertainty. Significant deviations from this value could suggest the existence of new physics beyond the Standard Model.

This chapter introduces the Standard Model of Particle Physics and explores its incompleteness. Later, the foundations of the weak interaction and the importance of the mixing angle ($\sin^2\theta_W$) are described in the context of the MOLLER experiment.

Finally, this chapter outlines the thesis objectives. It focuses on justifying the construction of the Gas Electron Multipliers (GEM) stand to characterize the High Voltage Monolithic Active Pixel Sensors (HVMAPS) in the MOLLER main integrating detector.

1.1 The Standard Model of Particle Physics

The Standard Model (SM) of Particle Physics is an extraordinarily successful theoretical framework that precisely describes the elementary particles and their interactions (force carriers) —excluding gravity (see Figure 1.1). It unifies the electromagnetic, weak, and strong interactions, accurately predicting particle properties and interaction strengths. These predictions have been rigorously confirmed by numerous experiments over several decades [1].

A cornerstone of the Standard Model is the electroweak interaction (described in detail at section 1.2), which unifies the electromagnetic and weak forces within a single theoretical framework known as the Glashow–Weinberg–Salam (GWS) theory.

This unification represents a major conceptual achievement, and its validity has been reinforced by key experimental milestones: the observation of the weak neutral current in 1973 [2], the discovery of the $W^{\pm}$ and Z^0 bosons at CERN in 1983 [3], and the detection of the Higgs boson in 2012 [4], [5]. In addition, precision measurements at both high-energy colliders and low-energy experiments have consistently confirmed the Standard Model's predictions, underscoring its status as the most successful theory of fundamental particles and their interactions [6].

.

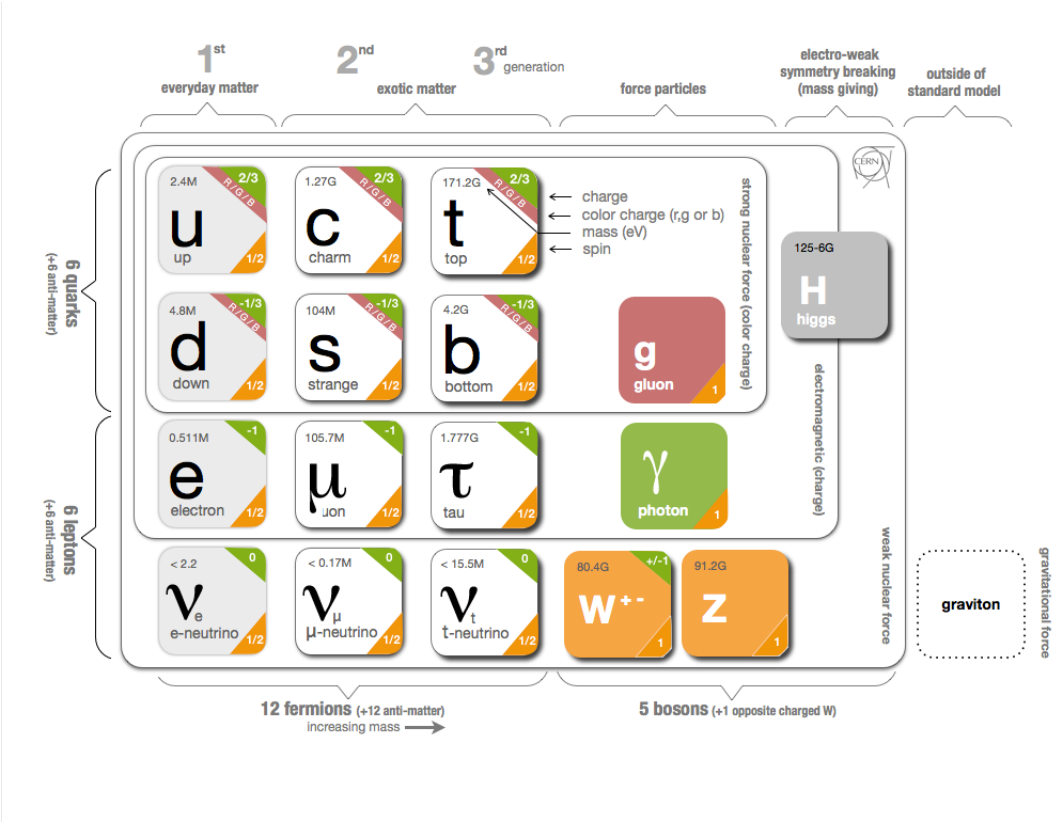

Figure 1.1: The elementary particles (12 fermions) and their gauge bosons (five bosons) in the Standard Model of Particle Physics [7].

Despite these achievements, the SM is incomplete. It fails to explain several fundamental phenomena, compelling physicists to search for new physics beyond the Standard Model (BSM). For instance, the ΛCDM cosmological model—the prevailing paradigm in modern cosmology—predicts the existence of cold dark matter (27% of the Universe), an unknown form of matter not accounted for by any SM particle [8]. The SM also cannot explain why neutrinos have mass [9] or the dominance of matter over antimatter in the Universe [10].

Furthermore, several experimental anomalies hint at the existence of BSM physics. These include deviations in the muon's anomalous magnetic moment [11], rare flavor-changing processes, and results from high-precision experiments. On the theoretical side, the SM does not resolve the hierarchy problem nor unify the strong force with the electroweak interaction, motivating the need for Grand Unified Theories (GUTs). GUTs aim to merge the three gauge interactions of the Standard Model into a single framework [12].

To search for effects beyond the Standard Model, physicists employ several complementary strategies [13]: probing the high-energy frontier through direct production of new particles at colliders; advancing the precision frontier via extremely sensitive measurements of known processes to reveal subtle deviations; exploring the intensity frontier by investigating rare or forbidden processes with high statistics; and utilizing astroparticle and cosmological observations to uncover evidence of new physics in the universe. Among these strategies, the precision frontier plays a particularly crucial role in probing BSM physics. By leveraging the exceptional agreement between electroweak theory predictions and experimental results, even the smallest deviations in precisely measured observables can hint at new interactions or undiscovered particles.

1.2 The Electroweak Interaction

The electroweak interaction unifies two of the fundamental interactions — the electromagnetic and weak interactions — within a consistent and successful theoretical framework. This unification resolved longstanding conceptual challenges regarding the nature of these interactions and enabled precise predictions that have been experimentally confirmed with remarkable accuracy [14]. In the following sections, we explore the historical development and theoretical foundations of electroweak unification, along with its key experimental verifications.

The study of weak forces began with Henry Becquerel in 1900 with the discovery of β radiation [15]. In 1914, Chadwick discovered that the energy of the β radiation was not a single value, but a continuum [16]. This fact indicated that the β decay did not conserve energy. To remedy this situation, Pauli theorized the existence of another particle emitted in β decay (neutrino ν), along with the electron, carrying off the missing energy,

$$X \longrightarrow X^{'} + e^{-} + \nu. \tag{1.1}$$

The particle had to be weakly interacting to have avoided detection. It was clear that the ν particle could not interact electromagnetically but only through a new interaction, called the weak interaction. Enrico Fermi introduced the new particle (neutrino) into the Standard Model to fully describe theoretically the β-decay (with a strength coupling constant denoted as G_F).

In 1949, Lee, Yang and Rosenbluth [17] postulated that all weak interactions are mediated by a massive boson, named the W^- (or anti-particle, the W^+).

Parity Violation

In 1956, Lee and Yang proposed a revolutionary hypothesis regarding parity symmetry in the weak interaction [18]. Lee and Yang proposed a break in the parity symmetry in the electroweak interaction to explain the decay processes of the particles known as τ and θ. Although these particles appeared identical, their decay modes exhibited opposite parities.

Parity, denoted by the operator P, corresponds to spatial inversion of a physical system; that is, it transforms spatial coordinates $\mathbf{r}$ into $-\mathbf{r}$. If a physical process is invariant under this inversion, it is said to conserve parity. Until that time, it was known that strong and electromagnetic interactions respected parity symmetry. However, Lee and Yang noted that there was no direct experimental evidence confirming parity conservation in weak interactions.

To further explore this idea experimentally, in 1957 Chien-Shiung Wu performed a pioneering experiment using polarized Co-60 nuclei undergoing beta decay (see Figure 1.2). By aligning the nuclear spins with a strong magnetic field, Wu measured the angular distribution of emitted electrons relative to the direction of the nuclear spin [19]. The results revealed a surprising asymmetry (A_{PV}): electrons were preferentially emitted opposite to the nuclear spin direction, indicating a clear violation of parity symmetry in weak interactions. This was the first definitive evidence that the weak force violates parity.

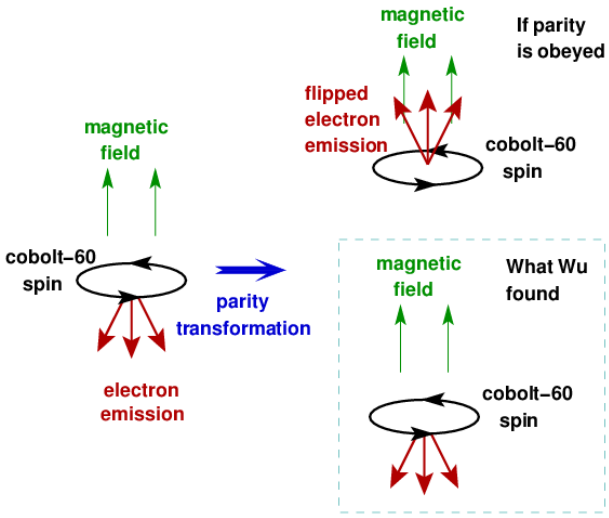

Figure 1.2: Cartoon of the Wu experiment. Wu observed that electrons were emitted preferentially in one direction - opposite to the spin of the Co-60 nuclei atoms - regardless of the magnetic field orientation [20].

The concept of helicity is key to understanding this phenomenon observed in Wu's experiment. Helicity is the projection of a particle's spin onto its direction of motion; it can be thought of as the particle's "handedness." In the case of the electrons emitted during the beta decay of polarized Co-60 nuclei, Wu found that these electrons were predominantly left-handed—that is, their spin was oriented opposite to their direction of motion (negative helicity). This preference for left-handed electrons implies that the weak interaction selectively couples to particles with a specific helicity. Since parity transformation flips the spatial coordinates and thus reverses helicity (turning left-handed particles into right-handed ones), the observation that only left-handed electrons participate signals a fundamental violation of parity symmetry. The weak interaction does not treat left- and right-handed electrons equivalently, a groundbreaking insight from Wu's measurements. Nowadays, with modern particle accelerator technology, physicists can now precisely control and manipulate the helicity of electrons—effectively simulating a parity transformation in the laboratory. By flipping the electron's helicity, experiments can directly probe the asymmetries predicted by the electroweak theory, providing deeper insight into the fundamental violation of parity symmetry.

Electromagnetic and Weak Interactions Unification

The first attempt to unify the electromagnetic and weak interactions was presented by Sheldon Glashow [21]. This theory predicted, in addition to the charged weak interaction mediators ($W^{\pm}$), the existence of a weak neutral current mediated by the Z^0 boson. In 1967, Steven Weinberg and Abdus Salam expanded upon this by proposing the unified electroweak theory, formulated as a gauge theory based on the symmetry group $SU(2)_L \times U(1)_Y$, which undergoes spontaneous symmetry breaking via the Higgs mechanism. This mechanism explains the difference in masses between the weak mediators ($W^{\pm}$ and Z^0) and the massless photon γ [22], [23].

The Glashow–Weinberg–Salam (GWS) theory introduces the concept of electroweak mixing, characterized by a single free parameter θ_W, that governs the relative strengths of the weak and electromagnetic interactions. θ_W also quantifies the mixing between the $SU(2)_L$ and $U(1)_Y$ gauge fields to produce the physical Z^0 boson and the photon. The coupling constants of this theory are g_e: electromagnetic coupling constant (related to the electric charge), g_W: weak coupling constant for the $W^{\pm}$ bosons, and g_Z, the weak coupling constant for the Z^0 boson.

These couplings constants arise in the $SU(2)_L \times U(1)_Y$ electroweak gauge theory from the physical fields A_μ (photon) and Z_μ that can be expressed as the linear combinations of the neutral gauge fields B_μ (hypercharge) and W_μ^3 (weak isospin) after electroweak symmetry breaking,

$$\begin{aligned} A_\mu &= B_\mu \cos\theta_W + W_\mu^3 \sin\theta_W, \\ Z_\mu &= -B_\mu \sin\theta_W + W_\mu^3 \cos\theta_W. \end{aligned} \tag{1.2}$$

The weak mixing angle is defined in terms of the original gauge couplings g (for $SU(2)_L$) and g' (for $U(1)_Y$) as:

$$\sin\theta_W = \frac{g'}{\sqrt{g^2 + g'^2}}, \qquad \cos\theta_W = \frac{g}{\sqrt{g^2 + g'^2}}. \tag{1.3}$$

The electric charge e arises from the unbroken $U(1)_{\text{em}}$ symmetry and is related to the gauge couplings through

$$e = g \sin\theta_W = g' \cos\theta_W. \tag{1.4}$$

From these relations, one obtains the couplings:

$$g = \frac{e}{\sin\theta_W}, \qquad g' = \frac{e}{\cos\theta_W}. \tag{1.5}$$

The charged weak interaction is mediated by $W^{\pm}$ bosons with coupling strength,

$$g_W = g = \frac{e}{\sin\theta_W}, \tag{1.6}$$

and the neutral current mediated by the Z^0 boson involves the coupling,

$$g_Z = \frac{g}{\cos\theta_W} = \frac{e}{\sin\theta_W \cos\theta_W}. \tag{1.7}$$

Thus, the weak and neutral couplings are:

$$g_W = \frac{g_e}{\sin\theta_W}, \qquad g_Z = \frac{g_e}{\sin\theta_W \cos\theta_W}. \tag{1.8}$$

These relations arise from the structure of the electroweak Lagrangian after spontaneous symmetry breaking, where the gauge fields mix to yield the physical bosons.

More importantly, the electroweak theory makes a testable prediction relating the masses of the weak bosons:

$$\cos\theta_W = \frac{M_W}{M_Z}, \tag{1.9}$$

where M_W and M_Z are the masses of the $W^{\pm}$ and Z^0 bosons, respectively. This expression provides a powerful connection between the abstract theoretical framework of the electroweak theory and experimentally measurable quantities.

The discovery of the weak neutral current in 1973 by the Gargamelle collaboration [2], and the subsequent observation of the $W^{\pm}$ and Z^0 bosons in 1983 at CERN [3], provided strong experimental confirmation of the GWS electroweak theory.

In the electroweak theory, the weak mixing angle, θ_W, stands out as one of the most precisely measured and theoretically important parameters. It quantifies the extent to which the neutral gauge bosons from the $SU(2)_L$ and $U(1)_Y$ symmetries mix to form the physical photon and Z^0 boson. The form quantity $\sin^2\theta_W$ appears in numerous cross-sections and asymmetry measurements involving electroweak processes. In fact, the knowledge of $\sin^2\theta_W$ and G_F are sufficient to calculate the mass of the W and Z^0 particles.

In 1978, the E122 experiment at SLAC measured $\sin^2\theta_W = 0.20 \pm 0.03$, using the parity-violating electron scattering (PVES) in a deuterium target [24]. The Parity-Violating Electron Scattering (PVES) is a precision technique used to probe the weak neutral current by measuring the tiny asymmetry in the scattering cross section of longitudinally polarized electrons off unpolarized targets. More recently, the SLAC E158 experiment measured $\sin^2\theta_W$ through parity-violating Møller scattering (PVES) using a liquid hydrogen target, where longitudinally polarized electrons scattered off unpolarized electrons [25]. This provided the world's most precise low-energy determination of the weak mixing angle at the time. Building on this technique, the MOLLER experiment aims to improve the precision of $\sin^2\theta_W$ by a factor of five relative to this measurement, offering a powerful probe for potential physics beyond the Standard Model. The value of $\sin^2\theta_W$ has also been extracted using atomic parity violation [26], electron-proton scattering [27], and more recently in hadron colliders [27].

1.3 The MOLLER Experiment

The MOLLER (Measurement of a Lepton-Lepton Electroweak Reaction) experiment is an international collaboration that will extract the weak mixing angle $\sin^2\theta_W$, at a momentum transfer of $Q^2 = 0.0056$ GeV^2. Here, Q^2 represents the negative of the squared four-momentum transferred in the scattering process and serves as a measure of the energy scale at which the interaction is probed. The value of $\sin^2\theta_W$ will be determined by measuring the parity-violating asymmetry, A_{PV} (32 ± 0.8 ppb), in electron-electron (Møller) scattering. The A_{PV} is given by the following expression [28],

$$A_{PV} = \underbrace{\frac{(\sigma_R - \sigma_L)}{(\sigma_R + \sigma_L)}}_{\text{Observable}} = \underbrace{mE\frac{G_F}{\sqrt{2}\pi\alpha}\frac{4\sin^2\theta}{(3+\cos^2\theta)^2}Q_W^e}_{\text{Standard Model prediction}}, \tag{1.10}$$

where σ_R and σ_L are the cross sections for incident right-handed (positive helicity) and left-handed electrons (negative helicity), respectively; Q_W^e is the weak charge of the electron, m is the electron mass, E is the incident beam energy, G_F is the Fermi constant, α is the fine structure constant, and θ is the angle of deflection of the electron with respect to its initial direction. In Equation 1.10, the weak charge Q_W is expressed at tree level as

$$Q_W^e = 1 - 4\sin^2\theta_W, \tag{1.11}$$

MOLLER expects to measure this with a precision of 2.4 % [29].

As with other coupling constants in the Standard Model, $\sin^2\theta_W$ evolves with the energy scale μ due to quantum corrections, including renormalization effects and loop contributions from all particles participating in the interaction. This energy dependence, often referred to as the"running" of the weak mixing angle, is a direct consequence of the electroweak unification and can be precisely predicted within the Standard Model. The predicted running is illustrated as a dark blue line in Figure 1.3. Any experimental deviation from this value is sensitive to the existence of particles and interactions via quantum loop corrections [29].

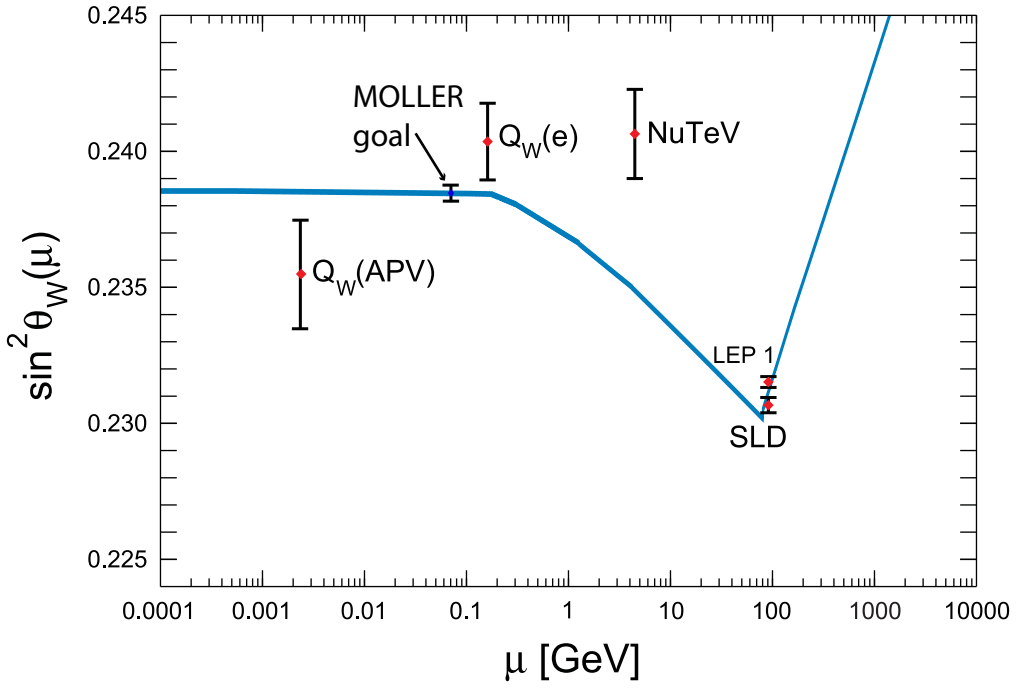

Figure 1.3: The running of $\sin^2\theta_W$ with energy scale μ. Figure taken from [29].

1.3.1 MOLLER Apparatus

The MOLLER experiment will utilize the upgraded 11 GeV polarized electron beam provided by the Continuous Electron Beam Accelerator Facility (CEBAF) at the Thomas Jefferson National Accelerator Facility (JLab) in Virginia, USA. The apparatus is planned to be installed in Hall A at JLab.

Figure 1.4 illustrates the fundamental concept and layout of the MOLLER experiment, highlighting the key components. In this figure, an helicity alternating longitudinally polarized *electron beam* scatters off a fixed unpolarized *liquid hydrogen target chamber*.

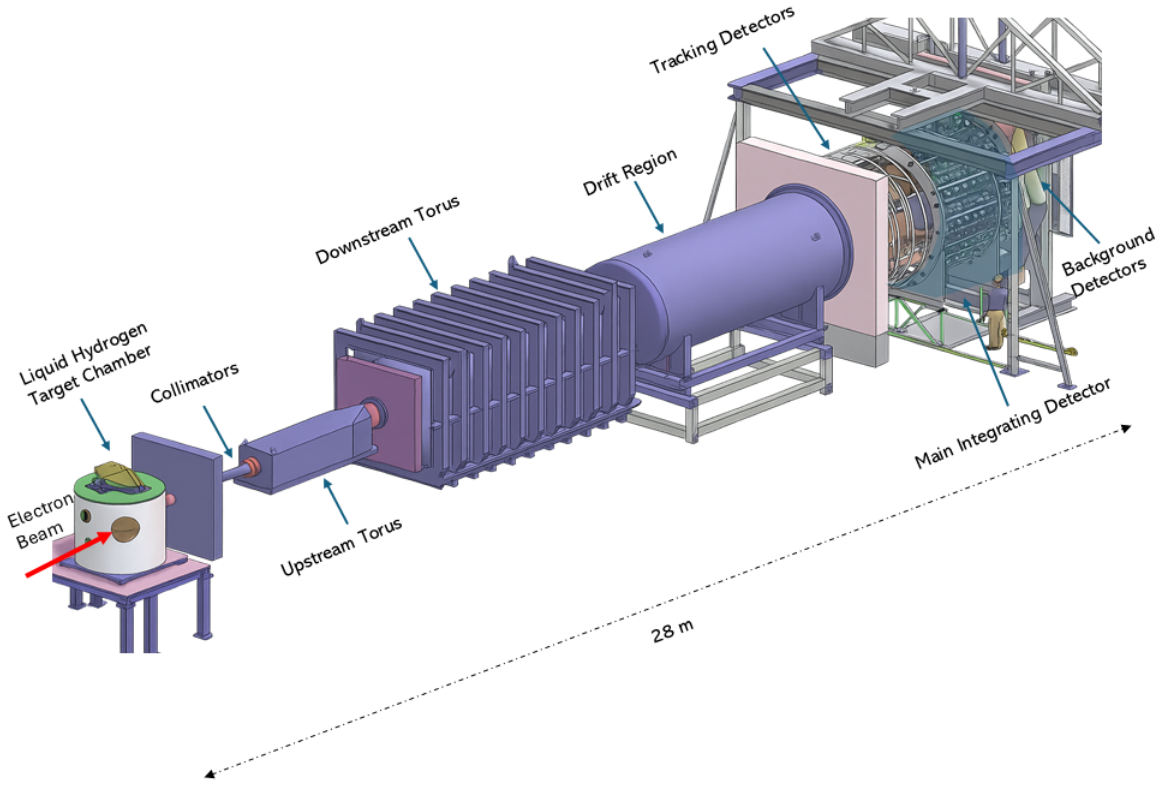

Figure 1.4: General diagram of the MOLLER apparatus. Figure adapted from [30].

A system of *collimators* and toroidal magnets—referred to as the *upstream* and *downstream torus*—separates the Møller-scattered electrons from background particles and directs them toward the detectors located at the focal plane. This magnetic spectrometer configuration enables precise selection of the scattering angle and momentum of the electrons, which is essential for an accurate measurement of the parity-violating asymmetry.

At the end of the beamline, a set of *tracking detectors* based on Gas Electron Multiplication (GEM) and trigger scintillators are used to improve background subtraction and kinematic reconstruction. The *main integrating detector* collects the Møller scattering rates and performs the primary measurement of A_{PV}. An additional *shower-max detector* (not shown in the figure) provides a complementary measurement of A_{PV}. Finally, a set of *background detectors* is used to validate and correct for systematic uncertainties in the measurement.

1.3.2 Main Integrating Detector

The main integrating detector is shown in Figure 1.5. It consists of an array of 224 thin quartz air-core light-guide Cherenkov detectors (modules). These are arranged into 28 azimuthal segments and divided radially into 6 concentric rings. Each azimuthal segment contains 8 detector modules, except for ring five, which includes three modules per segment. The high segmentation of the main integrating detector allows for radial and azimuthal binning of the scattered Møller event profile [see Figure 1.7]. This enables the separation of irreducible backgrounds from the Møller signal, improves statistical sampling, and facilitates control over systematic effects such as electron beam motion and background contributions.

Each module of the main integrating detector has three main parts, a fused silica *quartz tile*, a *photomultiplier tube (PMT)*, and a *light guide (LG)*. The quartz tile acts as a Cherenkov radiator when hit with electrons whose speed are greater than the speed of light in the quartz medium. The light guide (LG), made of a highly ultraviolet reflective material, channels light from the quartz tile to the photomultiplier tube (PMT), which can operate in both event (measuring individual events) and current (integrating) modes. In current mode, after amplification, the PMT signal is integrated to measure the raw asymmetry A_{raw},

$$A_{raw} = \frac{I^+ + I^-}{I^+ - I^-}, \tag{1.12}$$

where I is the average anode current in the PMT expressed as $I = R < n_{PE} > e^{-G_{PMT}[C/s]}$, where R is the number of electrons received by the quartz tile per unit of time, $< n_{PE} >$ the mean number of cathode photo-electrons, and G_{PMT} the gain of the PMT. The sign of I, represents the helicity state measured.

The A_{raw} obtained from Equation 1.12 is subsequently used to determine the parity-violating asymmetry A_{PV} using the detector modules located in ring five, where the Møller peak is centered (see Figure 1.6). However, this raw asymmetry must be corrected for additional sources of asymmetry and various background contributions (see [31] for details).

In contrast, the remaining radial rings of the main integrating detector—rings one, two, three, four, and six—are primarily used for background suppression, beam diagnostics, and systematic uncertainty studies.

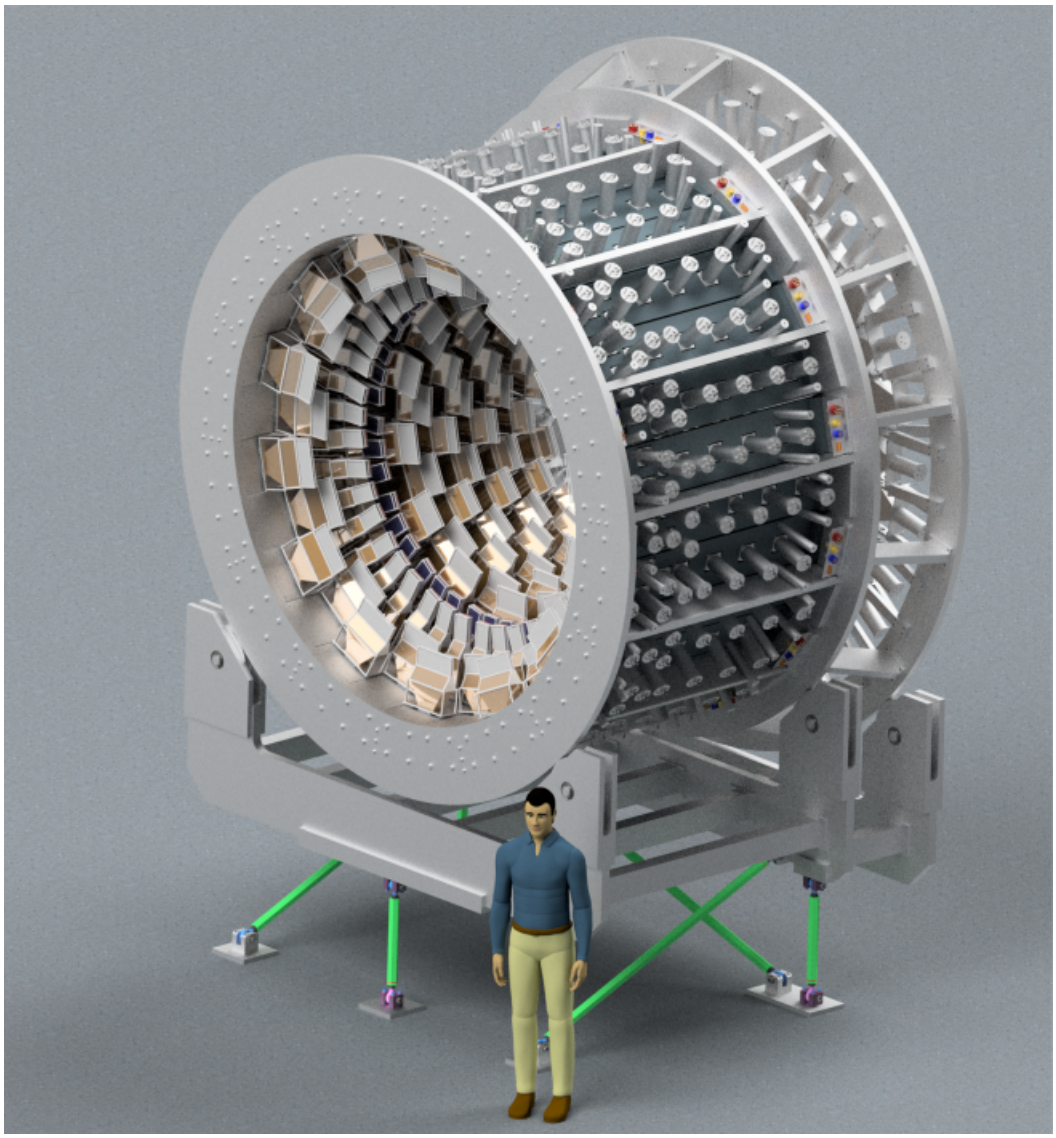

Figure 1.5: CAD illustration of the entire main integrating detector, including the 224 thin quartz air-core light guide Cherenkov detectors. [31].

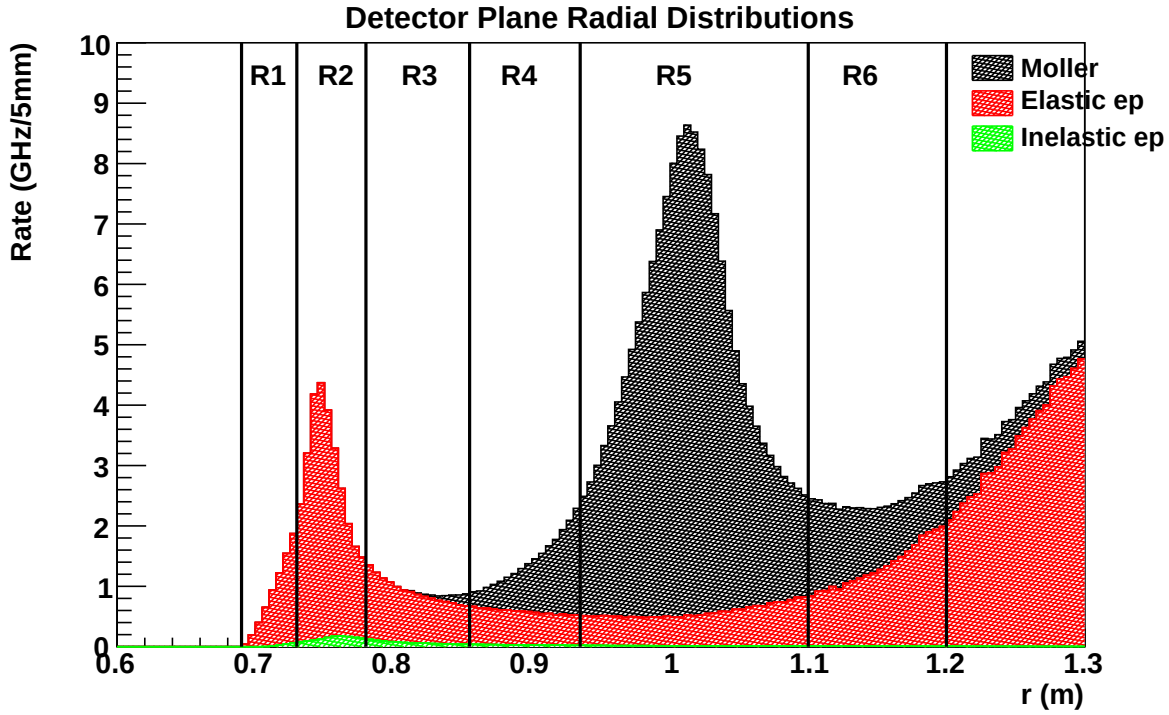

Figure 1.6: Radial distribution of the detector rates for Møller (black), elastic (red) and inelastic (green) electron scattering with protons. Figure taken from [29].

1.3.3 Ring Five HVMAPS Profile Detectors

The 84 modules in ring five of the main integrating detector is where the Møller-scattered electrons are expected to be focused, as determined by the spectrometer design. To verify the spatial distribution of the scattered electrons (see Figure 1.7) and to monitor the modules performance, each module in this ring will be equipped with an array of twenty-eight 2x2 cm^2 High Voltage Monolithic Active Pixel Sensor (HVMAPS) positioned directly behind the corresponding quartz tile (see Figure 1.8). In addition, the HVMAPS can also be used for tracking by matching the spatial information gathered by the *tracking detectors*.

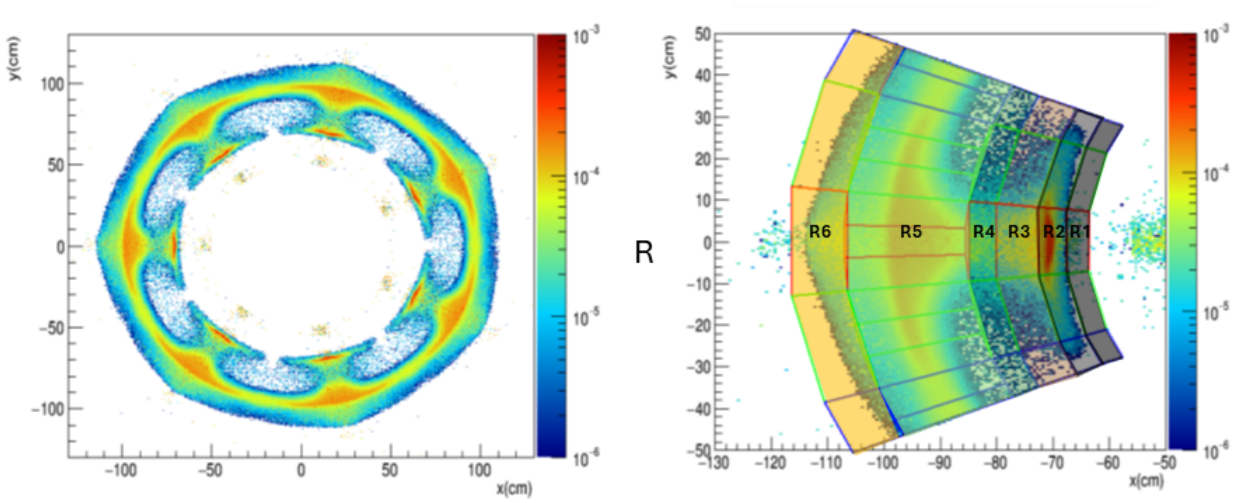

Figure 1.7: Simulation of the cross-section-weighted rates for Møller scattering, elastic electron-proton, and inelastic electron-proton interactions, in units of GHz/μA/0.5 cm^2. *Left:* Full detector plane view. *Right:* Binned view approximating the segmentation of the main integrating detector modules, with slices corresponding to the radial ring structure. Figure adapted from [32].

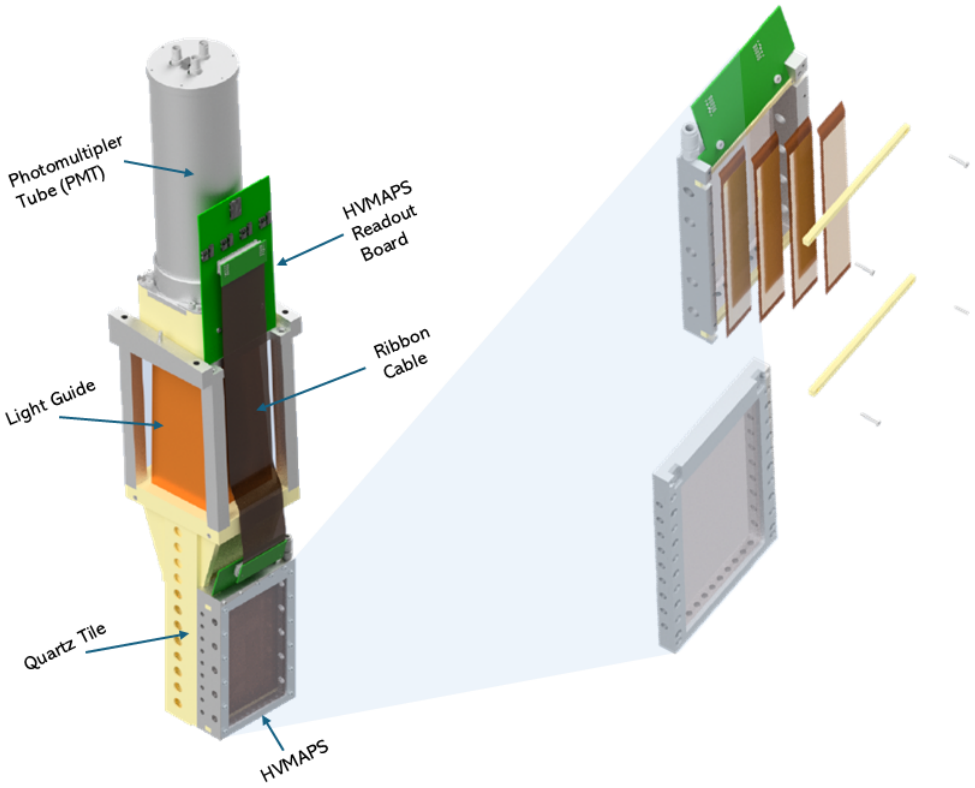

Figure 1.8: Conceptual design of the ring five assembly and its main features. To the right, an exploded view illustrates the components of the HVMAPS assembly. Figure adaptated from [32].

The High Voltage Monolithic Active Pixel Sensors (HVMAPS) are based on the High-Voltage Complementary Metal-Oxide Semiconductor (HV-CMOS) process, which integrates both the analog and digital readout electronics within the same die as the silicon detector [33]. Their high spatial resolution, high rates operability (up to 30 MHz), low material budget, and radiation hardness make them particularly well-suited for harsh environments like those found at the MOLLER experiment site (Jefferson Lab).

1.4 Thesis Objective and Structure

To meet the specific requirements of the MOLLER experiment, a modified version of the MuPix 10 HVMAPS chip, known as P2Pix, is currently under development and implementation [34]. The MOLLER local group at the University of Manitoba has addressed several major challenges associated with this technology, such as the engineering of a dedicated cooling system to manage the heat generated during operation [35], and the development of an HVMAPS assembly station [36].

To obtain key performance metrics of the HVMAPS—namely, spatial resolution, detector efficiency, and angular response—a reference tracking system is required. As a preparatory step toward this goal, a GEM stand, consisting of two triple-GEM detectors operating in tracking mode, has been commissioned and characterized using cosmic muons and an Fe-55 X-ray source. This setup will eventually enable cross-comparison (track matching) between GEM-reconstructed tracks and the signals recorded by the HVMAPS sensors under test.

The commissioning and characterization of the GEM stand presented in this work are distributed throughout the thesis as follows:

- **Chapter 2:** Introduces the theory behind gaseous detectors—specifically, the Gas Electron Multiplier (GEM)—and their operating principles.
- **Chapter 3:** Describes the commissioning of the GEM stand made of two triple-GEMs, and the supporting subsystems required for its successful operation.
- **Chapter 4:** Details the response of the GEM stand to cosmic muons and an Fe-55 source to evaluate sensitivity, and optimal operating conditions.
- **Chapter 5:** Summarizes the main findings of this work and outlines directions for further improvements.

Chapter 2

Principles of Gas Filled Detectors

Gas-filled detectors play a fundamental role in particle physics experiments due to their ability to cover large areas and provide spatial resolution at relatively low cost. Their operating principles rely on the physical processes by which charged particles, electrons, and photons lose energy as they traverse a gaseous medium, resulting in the production of free electron-ion pairs, which can subsequently be drifted and amplified when immersed in an electric field. This chapter introduces the theoretical background and operational principles underpinning gaseous detectors. Section 2.1 outlines the mechanisms of energy loss for different types of radiation interacting with matter, including heavy charged particles, electrons, and photons. Section 2.2 focuses on the response of gaseous media to ionizing radiation, covering the processes of primary ionization, charge drift and diffusion, and avalanche multiplication, as well as the influence of gas composition. Section 2.3 introduces the triple Gas Electron Multiplier (triple-GEM), a gaseous detector widely used for high-precision tracking and timing applications. Finally, Section 2.4 discusses methods for characterizing the performance of gas-filled detectors, including gain measurements and response uniformity. Together, these topics provide the foundation necessary to understand the behavior and optimization of the triple-GEM detector pair employed in this work.

2.1 Theory of Particle Energy Loss in Gases

2.1.1 Interaction of Heavy Charged Particles with Matter

Coulomb interactions between the electromagnetic fields of the incoming charged particles and the medium produce ionization and excitation of the atoms of the medium. These two processes are the most relevant to the total energy loss of the incoming particles.

Bremsstrahlung, Cherenkov and transition radiation are negligible in gas detectors.

The passage of charged particles through matter expressed in average loss energy per unit length is given by the Bethe-Bloch equation [37], [38],

$$-\frac{dE}{dx} = KZ_1^2 \frac{Z_2}{A_2} \frac{\rho}{\beta^2} \left[\frac{1}{2} \ln \left(\frac{2m_e c^2 \gamma^2 \beta^2 T_{max}}{I} \right) - \beta^2 - \frac{\delta(\beta)}{2} - \frac{C(\beta)}{Z_2} \right], \tag{2.1}$$

where,

- T_{max} : The maximum kinetic energy that can be imparted to a free electron in a single collision
- $K = 4\pi N_A r_e^2 m_e c^2 = 0.307\ MeV\ cm^2/mol$, with classical electron radius $r_e \approx 2.8\ fm$
- Z_1, β are charge and velocity of the projectile particle
- Z_2, A_2 and ρ are the atomic number, atomic mass and density of the medium respectively
- I is the mean excitation energy
- δ is the density correction (relevant for high energies)
- $\frac{C}{Z_2}$ is the shell correction (relevant for small β values)
- Note: A detailed summary of additional corrections can be found in [39]

Figure 2.1 describes a rapid decrease as a function of β. It reaches a minimum value around $\beta\gamma = 1.2$. Muons created in the upper atmosphere by cosmic rays interactions have mean energy loss rates close to the minimum, and are said to be minimum ionizing particles, or MIP. After that, it starts to rise following the so-called relativistic rise ($\beta\gamma \to \infty$).

It should be noted that equation 2.1 is valid for all particles except electrons e^- and positrons e^+. In such cases, the equation should be modified.

2.1.2 Interaction of Electrons with Matter

As depicted in Figure 2.2, the behaviour of electrons going through matter depends on their energy. At low to moderate energies, the primary modes of interaction are: ionization, Møller scattering, Bhabha scattering and electron-positron annihilation. The ionization mode has the highest probability to happen inside a gaseous detector.

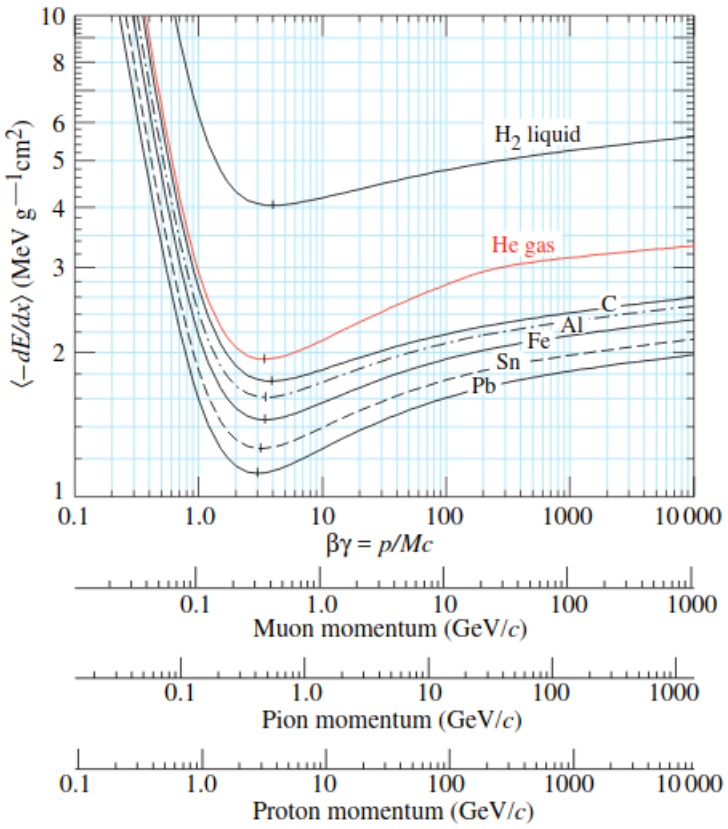

Figure 2.1: Mean energy loss rate in different target materials for muons, pions and protons (radiative effects for those particles are not taken into account). Figure taken from [37].

During the ionization, if an incident electron imparts enough energy to an atom it may eject one of its loosely bound electrons resulting in the ionization of the atom. The energy of the ejected electron depends on its binding energy as well as the energy transferred by the incident electron. This process can continue until the energy of the incident electron is less than the ionization potential of the atom (primary and tertiary ionization).

The rest of interaction modes present a low probability of interaction in comparison to the ionization. A description of those are beyond the scope of this work.

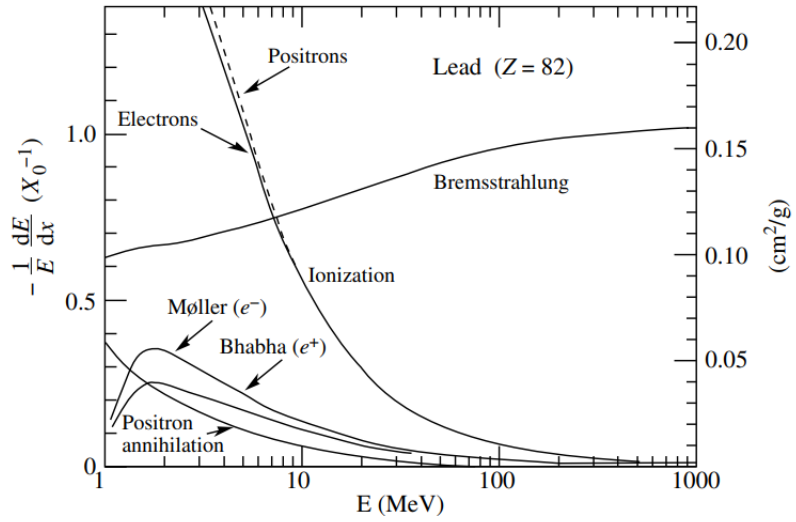

Figure 2.2: Fractional energy loss of electrons and positrons per radiation length as a function of energy. Figure taken from [40].

2.1.3 Interaction of Photons with Matter

Photons can interact with either bound electrons or the nucleus. The probability of photon absorption through matter (I), can be written in terms of the mass attenuation coefficient μ:

$$I = I_0 e^{-\sigma N x} = I_0 e^{-\mu x}, \tag{2.2}$$

where σ is the cross section of a photon beam traversing a medium, x is the thickness of the medium, and N the number of molecules per volume unit.

When the energy of an incident photon equals or exceeds the ionization energy of an electron bound to an atom within the medium, there exists a finite probability that the electron will be ejected—an interaction governed by the ionization cross section (σ in equation 2.2). Any excess energy is transferred to the ejected electron as kinetic energy. The total photon cross section per atom σ_T is given by:

$$\sigma_T = \sigma_{pe} + \sigma_R + Z\sigma_C + \sigma_{pp}, \tag{2.3}$$

where Z denotes the atomic number, representing the number of protons in an atom's nucleus. The remaining parameters in the equation are described in the following list.

- σ_{pe} : **Photoelectric effect**

  This process occurs when an incident photon interacts with an electron whose binding energy is comparable to, but less than, the photon's energy. As a result, the photon is absorbed, and the electron is ejected with a kinetic energy equal to the difference between the photon's energy and the electron's binding energy. The photoelectric effect is particularly relevant in gaseous detectors, as many radioisotopes emit X-rays in the keV range, which are sufficiently energetic to induce ionization through this mechanism.

- σ_R : **Rayleigh scattering**

  In this process, no energy is transferred between the incident photon and the bound orbital electrons because the electrons binding energy is too high compared to the photon's energy. As a result, the photon undergoes a change in direction while retaining its initial energy. The primary effect of Rayleigh scattering in matter is the reduction of the intensity of the incident beam due to elastic scattering.

- σ_C : **Compton scattering**

  The Compton scattering refers to the inelastic scattering of photons from free or loosely bound electrons which are at rest. Since the electron is almost free, it may also get scattered as a result of the collision. In general, for orbital electrons, the Compton effect is more probable than the photoelectric effect if the energy of the incident photon is higher that then binding energy of the innermost electron in the target atom. By applying energy and linear momentum conservation laws, the relation between wavelengths of incident and scatter photons,

  $$\lambda = \lambda_0 + \frac{h}{m_0 c}[1 - \cos\theta], \tag{2.4}$$

  where λ_0 and λ represent wavelengths of incident and scattered photons respectively, m_0 is the rest energy of electron, and θ is the angle between incident and scattered photons.

- σ_{pp} : **Pair production**

  In this process, a photon within matter is annihilated, producing an electron-positron pair. The photon is required to have an energy greater than twice the rest mass of an electron ($E_\gamma > 2m_e c^2$), so the photon energy can form the two masses.

2.2 Gaseous Ionizing Detectors

The operating principle of gaseous ionizing detectors is based on the direct collection of charges produced by ionization as particles pass through the gas. In comparison to liquid or solid detectors, the higher velocities of electrons and ions in gases enable faster charge collection in gaseous ionizing detectors. This characteristic improves the detector's temporal response, reduces charge recombination losses, and enhances overall signal efficiency [41]. For most gases, the minimum ionization energy ranges between 10 and 20 eV, but the average energy to ionize can be twice as big. There are three types of gaseous ionizing devices: ionizing chambers, proportional counters, and and Geiger-Müller counters. All of them work through the same principle.

2.2.1 Electron-ion Production within the Gas

As charged particles traverses a gas detector, it can produce electron-ion pairs —known as primary ionizations— provided its energy exceeds the ionization threshold of the gas. Under an external electric field, positive ions will be accelerated towards the cathode and electrons towards the anode, where they will be collected. Sometimes, the primary ionization may gain enough energy to produce secondary ionization (see Figure 2.3).

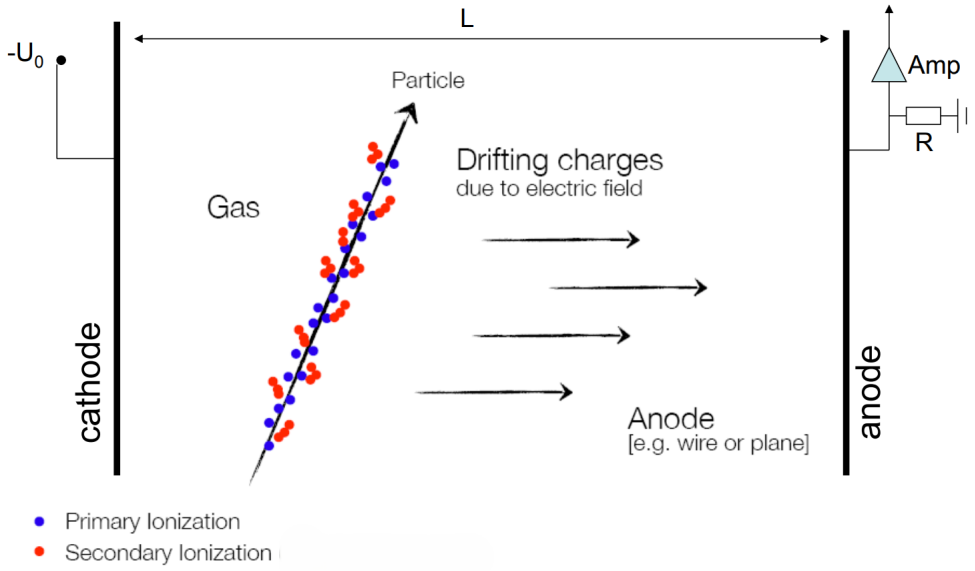

Figure 2.3: Basic operating principle of a gaseous ionization detector, showing ionization, drift, and charge amplification processes [42].

The number of ion pairs generated in the the gas n_{total} can be calculated through the following relation [41]

$$n_{total} = \frac{\Delta E}{W_i}, \tag{2.5}$$

where ΔE is the total energy loss in the gas by the charged particle, and W_i is the energy loss per created electron-ion pair. The Table 2.1 provides the W_i and dE/dx values for Ar and CO_2 gases.

Gas	W_i(eV)	$dE/dx(keV/cm)$	$\rho[g/cm^3]$ at 18° C
Ar	26	2.44	1.652×10^{-3}
CO_2	33	3.01	1.827×10^{-3}

Table 2.1: Energy loss per created electron-ion pair, and loss of energy per unit length for a minimum ionizing particle in Ar and CO_2.

To calculate the energy required to create an electron-ion pair in a specific gas mixture, such as Ar and CO_2, the following equation and data from table 2.1 are used:

$$\frac{1}{W_{Ar-CO_2}} = \frac{\%Ar}{W_{Ar}} + \frac{\%CO_2}{W_{CO_2}}. \tag{2.6}$$

Sometimes the resulting ion-electron pairs from the primary ionization do not produce secondary ionizations, so the electron escapes the medium and it is detected. These electrons produce the so-called "escape peak".

2.2.2 Diffusion and Drift of Charges in Gases

Thermal Diffusion

The kinetic theory of gases applied to electrons and ions describes how these particles spread uniformly away from their point of creation in the absence of an electric field. This random motion results from their thermal energy, defined as the average kinetic energy associated with the microscopic motion of particles due to temperature. At thermal equilibrium, each degree of freedom contributes $\frac{1}{2}kT$ to the average kinetic energy, where k is the Boltzmann constant and T the absolute temperature. For a particle in three dimensions, the average kinetic energy is $\frac{3}{2}kT$, and the corresponding mean thermal velocity v is given by:

$$v = \sqrt{\frac{8kT}{\pi m}}, \tag{2.7}$$

where m is the mass of the particle. Since ions are significantly more massive than electrons, their average thermal velocities are lower; therefore, electrons diffuse faster than ions under the same thermal conditions.

The spatial distribution of particles after a time t follows a Gaussian distribution, resulting from the central limit theorem applied to their random thermal motion. Assuming a one-dimensional case, the linear charge density dN/dx (i.e., the number of particles per unit length) at a distance x from the point of origin is given by:

$$\frac{dN}{dx} = \frac{N_0}{\sqrt{4\pi Dt}} \exp\left(-\frac{x^2}{4Dt}\right), \tag{2.8}$$

where N_0 is the total number of particles and D is the diffusion coefficient, which characterizes how fast particles spread due to thermal agitation.

Drift

The diffusion is a phenomena that happens in the presence of an electric field, when ions and electrons released from the ionizations generated by incoming radiation are accelerated along the electric field lines towards the anode and cathode. In fact, the average velocity is known as the drift velocity of each charge, v_d. The mobility of a charge, μ, can be defined as:

$$\mu = \frac{v_d}{E}, \tag{2.9}$$

where E is the strength of the electric field. In Table 2.2 the mobility values for Ar and CO_2 are shown. The mobility is also related to the diffusion coefficient as follows (Nernst–Townsend formula [41]):

$$\frac{D}{\mu} = \frac{kT}{e}, \tag{2.10}$$

this equation shows that the lower the temperature, the lower the electric field needs to be in order for the ions and electrons to move towards the electrodes.

Gas	Ion	Mobility ($cm^2V^{-1}s^{-1}$)
Ar	Ar^+	1.54
Ar	CO_2^+	1.72
CO_2	CO_2^+	1.09

Table 2.2: Mobility of ions for Ar and CO_2 gases. Table taken from [43].

2.2.3 Charge Multiplication in Gas Detectors

When the electric field strength inside a gas detector exceeds a certain value, the electrons that move in the electric field, between collisions, acquire sufficient energy to produce new ions. In other words, more electrons will be released, which will produce more ions. The net effect of this process is multiplication of the primary ionization (charge multiplication effect).

The positive ions drift slowly towards the cathode, while the electrons move quickly towards the anode due to the different mobilities for ions and electrons. The electrons pile up and make the resulting avalanche like a drop of water as shown in Figure 2.4 (Townsend avalanche [38]).

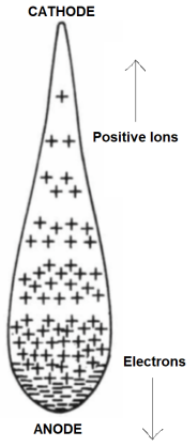

Figure 2.4: Avalanche formation. The electrons move faster than the positive ions producing an avalanche with the shape of a drop. Figure taken from [38].

For a given linear electron density n, the number of electrons in an infinitesimal length dx, will produce dn new electrons:

$$dn = n\alpha dx, \tag{2.11}$$

where α is the first Townsend coefficient. Integrating the above equation gives the total number of electrons n

$$n = n_0 e^{\alpha x} \qquad \Longrightarrow \qquad G = \frac{n}{n_0} e^{\alpha x}, \tag{2.12}$$

where n_0 is the initial number of electrons, x is the length of the path of ionization taken from the location of the primary ionization, and G is the multiplication factor or gain.

The gain G is proportional to the energy of incident particles in gaseous detectors operating as proportional counters. Due to space charge effects on the electric field, the value of G cannot be higher than 10^8 (also known as the Raether limit [41]).

2.2.4 Gas Mixture

Gaseous detectors filled with noble gases provide a high ionization probability and require only a low electric field to initiate avalanche multiplication (see the case for argon in Table 2.3). Argon gas is commonly used as a filling due to its relatively low ionization energy, low cost, wide availability, and chemical inertness, which makes it safe to handle.

Gas	**Excitation energy (eV)**	**Ionization energy (eV)**	**Mean electron-ion energy (eV)**
Ar	11.6	15.8	26
CO_2	10.0	13.4	33

Table 2.3: Characteristic energies for Ar and CO_2 gases [38].

Argon and other noble gases can emit ultraviolet photons during high amplification processes. To prevent these photons from generating spurious signals through secondary ionization, a second gas—known as a quencher—is added to absorb the ultraviolet light. Quenching gases have a large amount of non-radiative excited states (vibrational and rotational). Thus they act as inhibitors by absorbing photons of all energies being radiated by the de-excitations of the noble gas atoms. Some examples of quenchers are CO_2, CH_4, and C_4H_{10}.

2.3 Gas Electron Multiplier

The Gas Electron Multiplier (GEM) is a gaseous detector with a spatial resolution around 100 μm, excellent time resolution (ns), detection efficiency above 98 %, and a rate capability up to 10 MHz/cm^2. The GEM is a relatively recent technology developed for the first time at CERN in 1998 [44].

As depicted in Figure 2.5, a GEM is composed of an anode, a cathode, and a GEM foil in between. Unlike traditional gas detectors with an anode wire, the gas amplification (multiplication of electrons) in a GEM occurs inside narrow holes in a special foil. A GEM foil is composed of a thin insulating Kapton foil of 50 μm thickness, coated with 5 μm copper layers on each side. It is perforated with small holes made using photolitography processes, equally spaced on the GEM foil (See Figure 2.6).

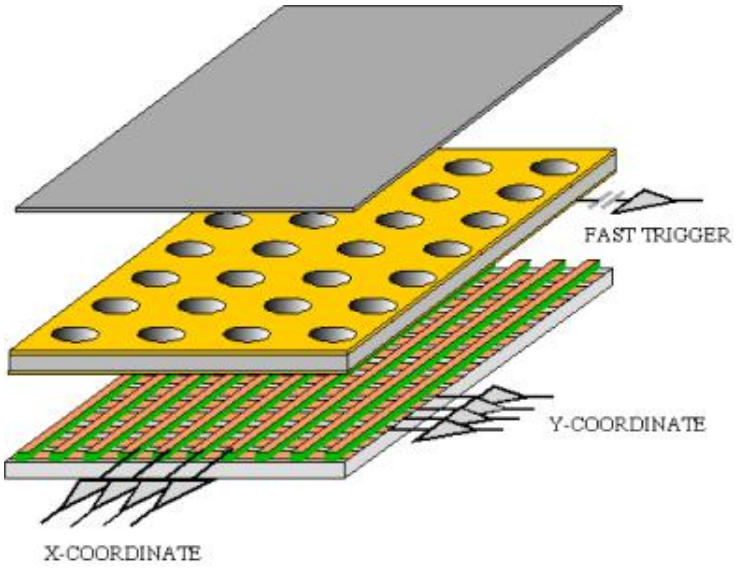

Figure 2.5: Schematic view of a single-GEM detector. Figure taken from [45].

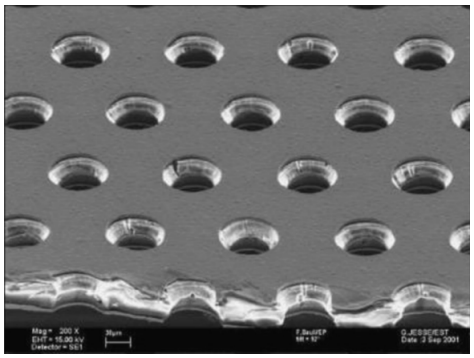

Figure 2.6: Electron microscope view of a GEM foil, 50 μm thick. The holes's pitch and diameter are 140 and 70 μm, respectively. Figure taken from [44].

To achieve a high gain, a high voltage is applied across the GEM. However, in this scenario, the probability of fatal discharge is relevant. Instead, multiple GEM foils are employed to reduce the discharge probability, allowing the amplification to be distributed across them. This configuration enables high total gain while maintaining a low voltage on each foil. A typical setup, called triple-GEM detector (see figure 2.7), consists of a drift zone—where the primary ionization occurs—followed by three GEM foils separated by a few millimeters, which form two transfer zones and a final induction zone. In each transfer zone, electrons are guided toward the next GEM foil to continue the amplification process, while the induction zone is where the readout strips collect the resulting signal.

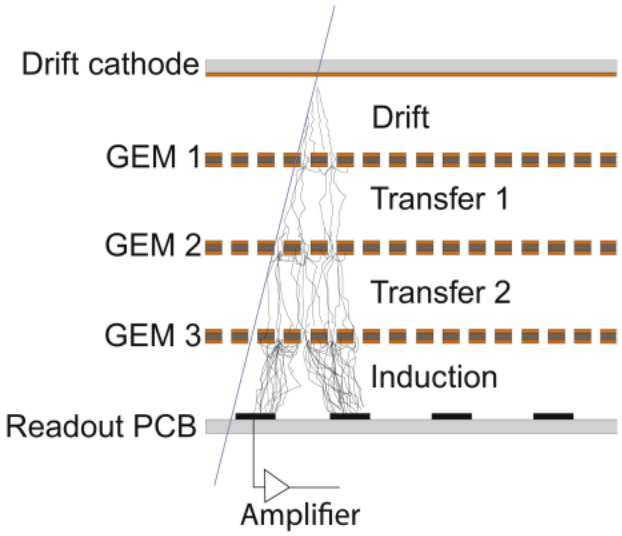

Figure 2.7: Drift, multiplication, and collection of charges in a triple-GEM detector. Figure taken from [44].

2.4 Characterization of a Gas Filled Detector

Characterizing a gas-filled detector focuses on evaluating its amplification performance, charge collection efficiency, and stability under varying operating conditions to ensure an optimal response to ionizing radiation in their range of functionality and applicability. Some of the most essential characterizations are as follows:

- **Sensitivity**

  Defined as the ability to produce a signal that can be measured for a given particle and energy range. It depends on the geometric cross section of the detector (physical area of the detector that is exposed to incoming radiation or particles) [46]. The physical cross section of the detector together with the mass determine to a great extent the probability of interaction of radiation within the detector medium. Volume, thickness, and segmentation of the detector also affect the sensitivity [38].

- **Response**

  The ratio between the energy deposited by an incident particle and the resulting output signal—expressed as charge—defines the detector response [46]. Ideally, this relation is linear; however, non-linearities can arise due to gain saturation or recombination effects. If a particle loses an amount of energy E_{rad} in the detector, the response r is defined as

  $$r = \frac{E_{rad}}{Q} \tag{2.13}$$

  where Q is the total collected charge after amplification. The detector signal is proportional to the number of ionization electrons created and multiplied by the gain G, so the charge Q reflects the deposited energy.

- **Energy resolution**

  The energy resolution of a detector quantifies how well it can distinguish between different amounts of energy deposited by incoming particles. It is usually determined from the shape of the energy spectrum, assuming a Gaussian distribution for the signal. In this case, the energy resolution is defined as the ratio between the Full Width at Half Maximum (FWHM) of the peak and its mean position μ_E, which represents the average deposited energy:

$$R = \frac{\text{FWHM}}{\mu_E} \tag{2.14}$$

  Since the width of the peak can vary with energy, the detector's energy resolution generally depends on the amount of energy deposited.

- **Gain**

  The gain is defined as the ratio between the charge measured at the readout anode and the charge initially generated by the incident particle. The typical procedure to calculate the gain G of a triple-GEM detector involves irradiating the detector with a source of known energy. This enables the estimation of the primary ionization charge $Q_{primary}$, corresponding to the electrons liberated in the drift gap due to the interaction of the incident radiation with the gas. By measuring the total charge Q_{total} collected at the readout, the absolute gas gain can be computed as:

$$G = \frac{Q_{total}}{Q_{primary}}. \tag{2.15}$$

  For a fixed detector geometry and drift field configuration, the gain G is primarily governed by the voltage applied across each GEM foil and by the properties of the gas mixture.

Chapter 3

Commissioning of the Test Stand

This chapter describes the commissioning of the experimental setup used to operate and characterize a pair of triple-GEM detectors within a dedicated stand. Section 3.1 outlines the specifications of the 10×10 cm^2 triple-GEM employed in this work, including the configuration of the high-voltage divider (Section 3.1.1) and the structure of the readout board (Section 3.1.2). Section 3.2 introduces the complete GEM stand setup including both detectors, along with a description of the data acquisition system (Section 3.2.1) and the gas panel used to supply and regulate the detector gas mixture (Section 3.2.2). Section 3.3 provides details on the gas mixture composition and its operational role. Finally, Section 3.4 summarizes the voltage configuration applied across the triple-GEM foils. Together, these sections provide the technical foundation for the detector performance studies and measurements presented in the next chapter.

3.1 The 10×10 cm^2 Triple-GEM

As indicated by its name, the 10×10 cm^2 triple-GEM detector shown in Figure 3.1 has an active area of 10 cm on a side. It is denoted as **active area** in the same figure. A pair of them were obtained through Techtra® company. Each of the triple-GEM detector includes a connection to a high voltage divider (see **high voltage divider** in figure 3.1, and figure 3.2), a gas input and output and an electronic readout system (figure 3.1:**readout board**).

The triple-GEM detector is equipped with 256 readout channels (128 channels along the X-direction and 128 along the Y-direction), providing a spatial segmentation of 128×128 orthogonal strips. The resulting strip pitch is $p = 781$ μm [47].

If the hit position is assigned to the centre of the strip that registers the signal under a binary readout (i.e., hit or no hit), and all hit locations x within a strip are equally probable, the spatial resolution is fundamentally limited by the inability to determine the exact hit position within a single strip.

This limitation can be quantified by modelling the hit positions as a uniform distribution over a strip of width p [48]. In this case, the spatial resolution R, defined as the standard deviation σ of the uniform distribution, is given by:

$$\sigma = \sqrt{\frac{1}{p}\int_{-p/2}^{p/2} x^2\,dx} = \sqrt{\frac{1}{p}\left[\frac{x^3}{3}\right]_{-p/2}^{p/2}} = \sqrt{\frac{1}{p}\cdot\left(\frac{(p/2)^3-(-p/2)^3}{3}\right)}$$
$$= \sqrt{\frac{1}{p}\cdot\frac{2(p/2)^3}{3}} = \sqrt{\frac{1}{p}\cdot\frac{2\cdot p^3}{24}} = \sqrt{\frac{p^2}{12}} = \frac{p}{\sqrt{12}}. \tag{3.1}$$

Thus, the spatial resolution R is [49], [50]:

$$R = \sigma = \frac{p}{\sqrt{12}}. \tag{3.2}$$

Substituting the pitch:

$$R = \frac{781\ \mu\text{m}}{\sqrt{12}} \approx 225.4\ \mu\text{m}.$$

This value denotes the intrinsic spatial resolution limit of the triple-GEM detector in the absence of charge-sharing or interpolation between adjacent readout strips. Nevertheless, by employing the barycenter reconstruction method, spatial resolutions as fine as $R = 140\ \mu$m have been demonstrated, based on fabrication measurements reported by Techtra®[47].

3.1.1 High Voltage Divider

The voltage distribution across the GEM foils in the triple-GEM detector is established by a resistive divider network, composed of the resistors listed in Table 3.1. For simplicity, the capacitors included in the divider to reduce high-voltage noise are not shown in this work. A detailed schematic of the voltage divider, including these components, can be found in [51].

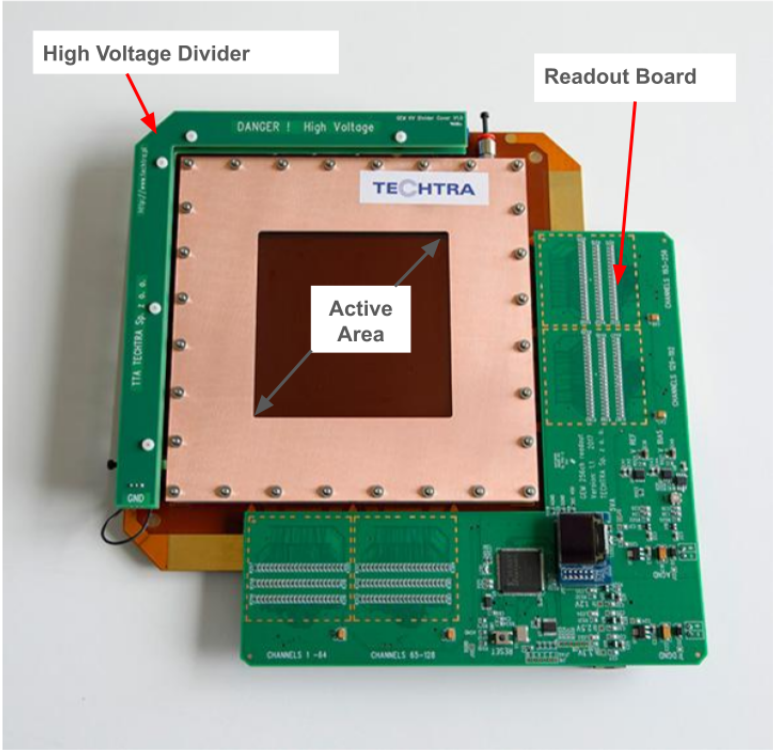

Figure 3.1: Schematic view of the triple-GEM detector main components.

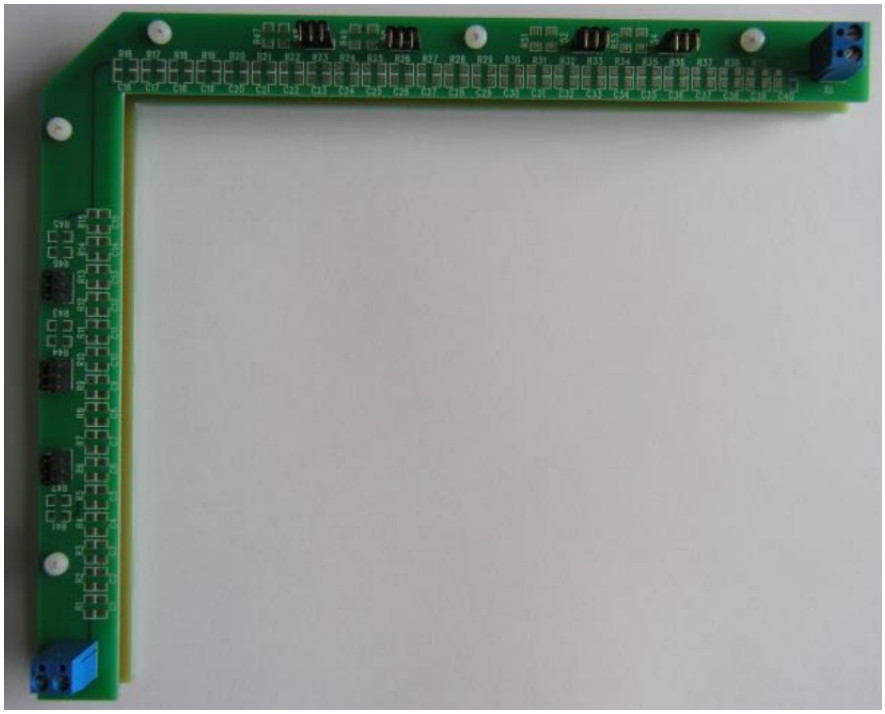

Figure 3.2: The high voltage divider PCB for each of the triple-GEM detectors.

Table 3.1: Design resistance values assigned to each stage of the triple-GEM detector's voltage divider chain.

Stage	**Resistance name**	**Voltage Drop (V)**
Drift	R_drift	12.0 MΩ
Drift Gap	R_drift_transfer	35.3 MΩ
GEM Foil 1	R_GEM_1	27.0 MΩ
Transfer Gap 1	R_transfer1	27.0 MΩ
GEM Foil 2	R_GEM_2	27.0 MΩ
Transfer Gap 2	R_transfer2	27.0 MΩ
GEM Foil 3	R_GEM_3	27.0 MΩ
Induction Gap	R_induction	35.3 MΩ
Node resistor (x7)	R_node	0.940 MΩ

In Figure 3.3, the node resistor (R_node) is added in series after each node (except after R_drift_transfer and R_induction), just before connecting to subsequent stages to protect against discharges. In this configuration, the total resistance R_{total} is

$$R_{total} = 12.0\,\mathrm{M\Omega} + (35.3\,\mathrm{M\Omega} + 0.940\,\mathrm{M\Omega}) + (27.0\,\mathrm{M\Omega} + 0.940\,\mathrm{M\Omega})\cdot 5 + 35.3\,\mathrm{M\Omega} \; = 223\,\mathrm{M\Omega}, \tag{3.3}$$

assuming an applied voltage of V = 3260 V, the current I through the chain is $I = V/R_{total} = 14.6\ \mu A$. For this example, the voltage drops V_i across each stage are given by $V_i = I \cdot R_i$. The table 3.2, summarizes the aforementioned voltage distribution.

Table 3.2: Voltage drops across each stage with node resistors included.

Stage	**Resistance (MΩ)**	**Voltage Drop (V)**
Drift	12.0	175.2
Drift Gap	36.24	529.0
GEM3	27.94	407.5
Transfer Gap 1	27.94	407.5
GEM2	27.94	407.5
Transfer Gap 2	27.94	407.5
GEM1	27.94	407.5
Induction Gap	35.3	515.4
Total	223.24	**3260 (approx.)**

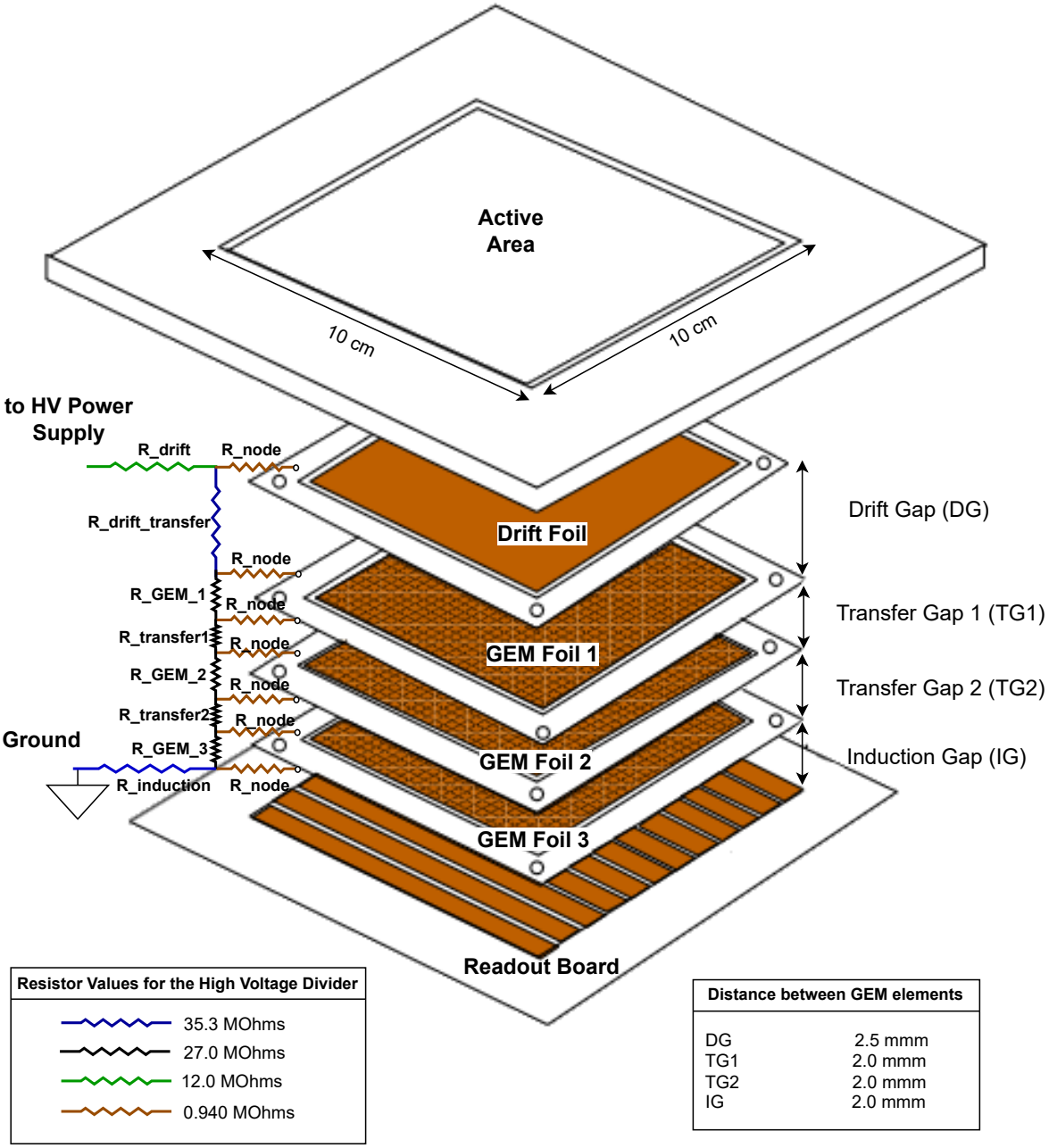

Figure 3.3: Schematic of the high voltage divider used in the triple-GEM detector, showing the resistor values assigned to each stage and the physical distances between the GEM foils. Image modified from [52].

3.1.2 Readout Board

The readout board or electronic data acquisition system of each of the triple-GEM detectors (shown in Figure 3.4) consists of low-noise multi-channel charge-to-digital converters, a Field-Programmable Gate Array (FPGA) that processes data and generates clock signals, and an Ethernet interface that communicates with a computer at 100 Mbit. It is directly plugged into X-Y readout strips via Panasonic connectors. Data collection occurs from 256 channels (128 x 128 orthogonal strips). The readout board sampling frequency is 4 kHz, with a resolution of 20 bits [47].

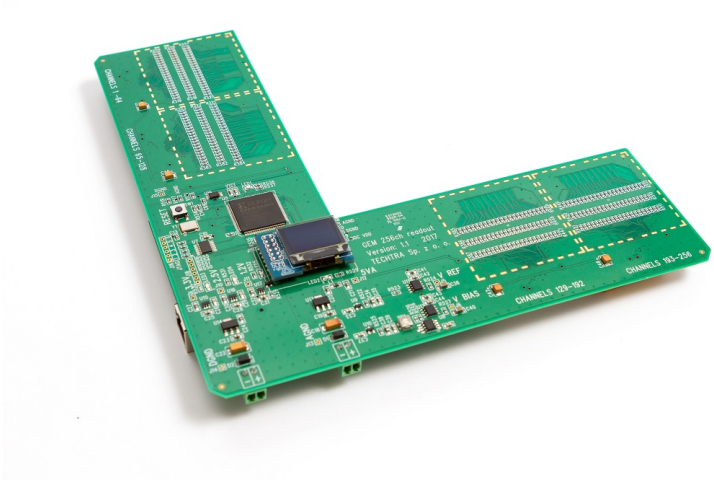

Figure 3.4: The readout board PCB for the triple-GEM detector (identical for both).

3.2 The Test Stand: Two Triple-GEM

The pair of triple-GEM detectors (see Figures 3.5 and 3.6) are aligned vertically in a dark box made of wood. For identification purposes, in Figure 3.5 they are named **top triple-GEM** and **bottom triple-GEM**. At the bottom left of the same figure, the high voltage supply used for both detectors is depicted as (**HV power supply**). The dark box gives structural support to the GEM stand and also will allow the testing the response of light sensitive sensors. The technical drawing of this part of the experiment can be checked in details in the figures of the Appendixes E.12 and B.2.

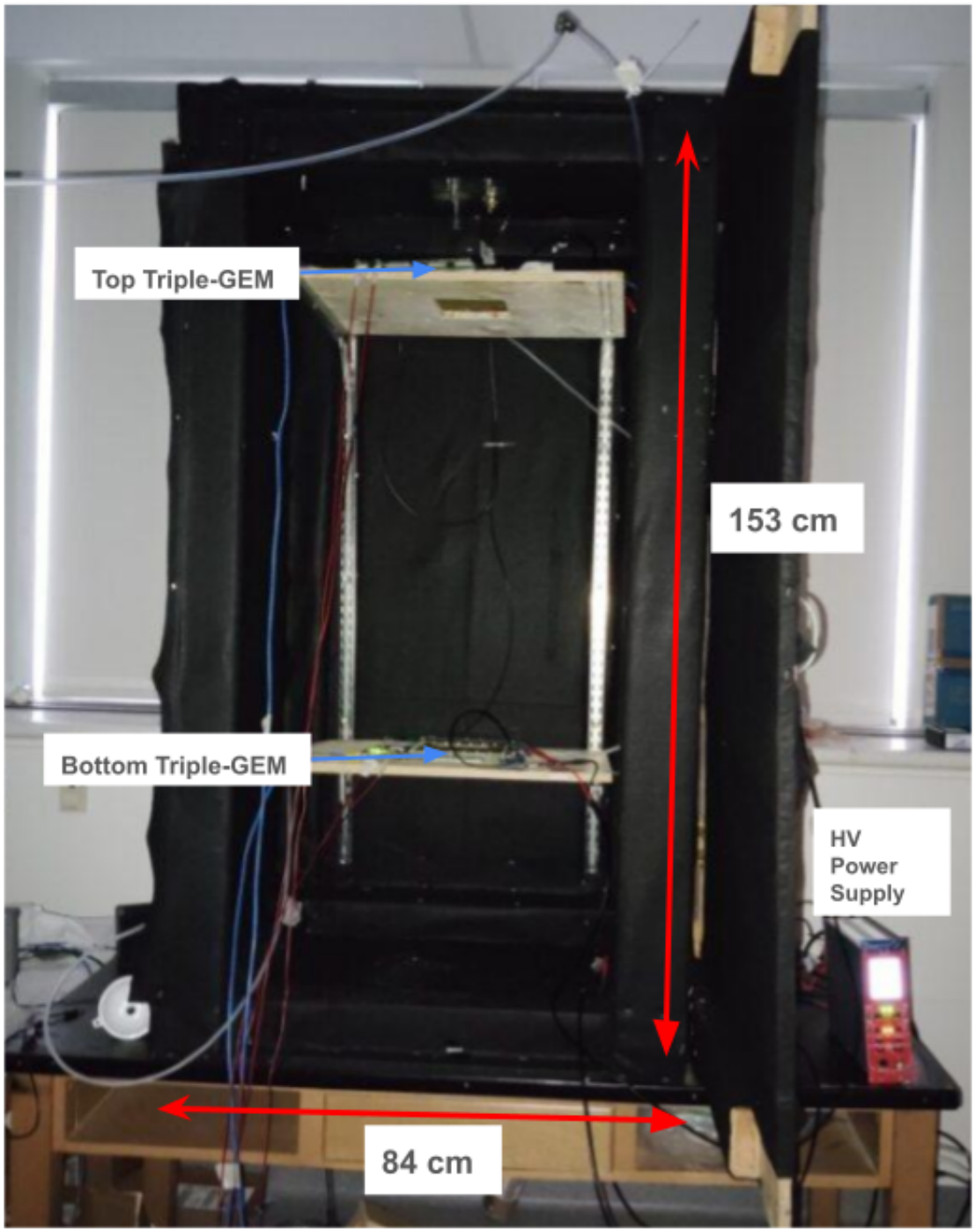

Figure 3.5: The GEM stand assembly consists mainly of a pair of commercial triple-GEM detectors housed inside a black box. The inner walls of the box are lined with black felt to prevent the intrusion of ambient light.

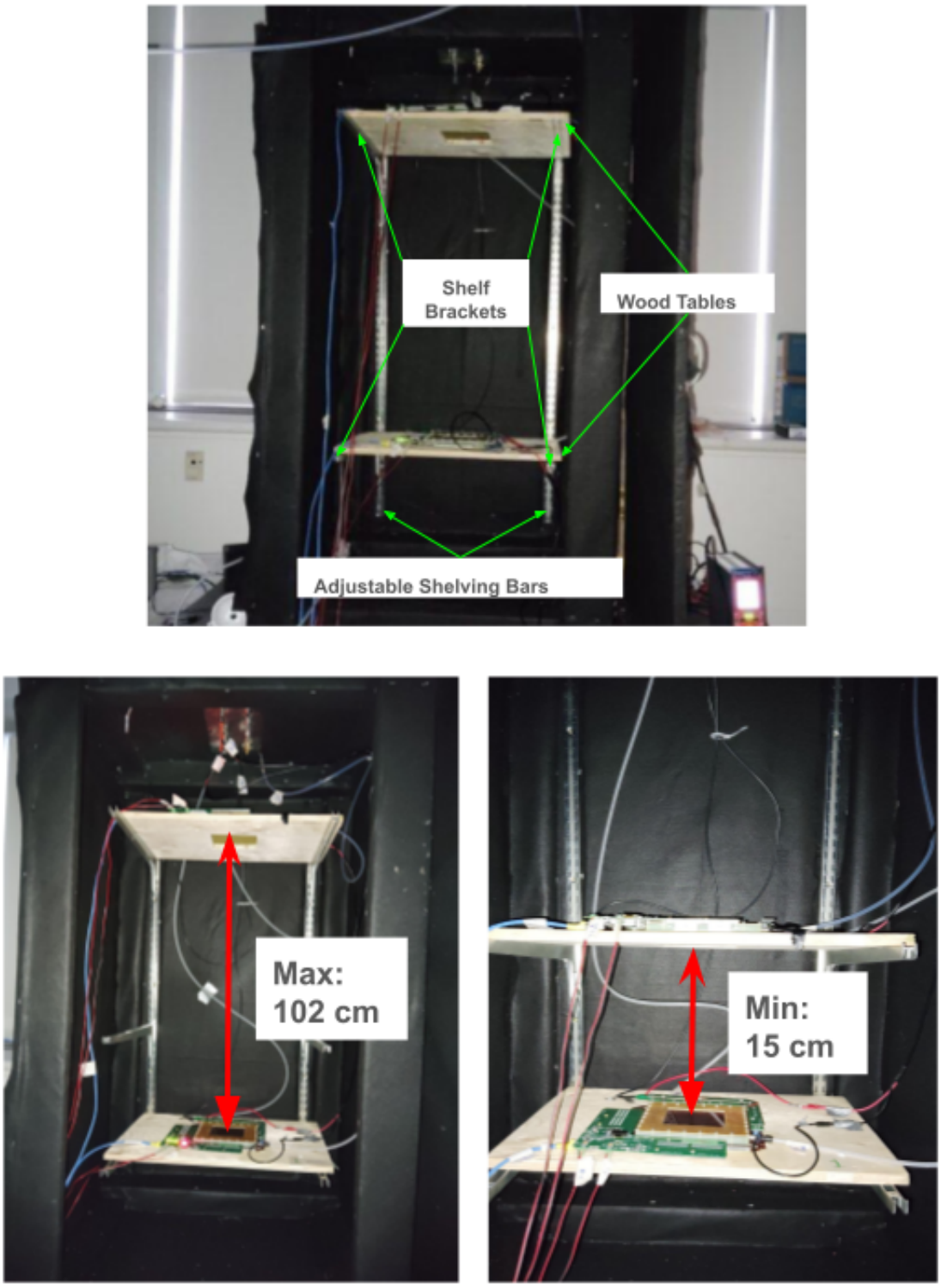

Figure 3.6: The mechanical structure of the GEM stand. Two vertical shelving bars support adjustable shelf brackets, allowing the horizontal wooden platforms holding the triple-GEM detectors to be freely positioned. The distance between the detectors can be adjusted from a minimum of 15 cm to a maximum of 102 cm, in 3 cm increments.

3.2.1 Data Acquisition (DAQ)

The data acquisition system consists of two readout boards, one per Triple-GEM. Each of the readout boards consists of four DDC264 current/charge-to-digital converters, an FPGA to control the device, and an Ethernet communication module for communication with a PC (see Figure 3.7). An Ethernet switcher helps with having both GEMs interface with the same PC (see Figure 3.8). The software setting to setup the DAQ can be found in the Appendix A.

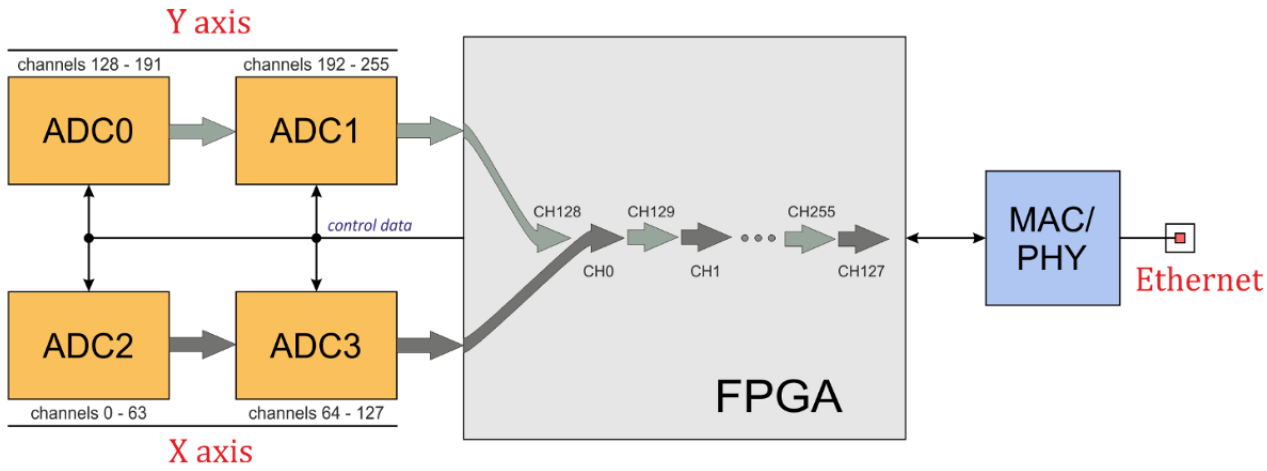

Figure 3.7: Simplified diagram of the DAQ data flow for each of the triple-GEM readout boards.

The DDC264 integrated circuits (Texas Instruments®) are four 64-channel 16/20-bit analog-to-digital converters (ADC), capable of digitizing charge signals. These are shown as ADC0, ADC1, ADC2, and ADC3 in Figure 3.7. The full-scale dynamic charge range of the DAQ can be adjusted through the Techtra® DDC software to the fixed values of 12.5 pC, 50 pC, 100 pC, and 150 pC [47]. The user can also define the integration time from 160 μs to 1 second. According to the readout board datasheet, the system offers a low-level linearity of $\pm$1.0 ppm, and noise of $\pm$ 6.3 ppm in the full-scale range [47]. To determine the full-scale dynamic range for operating the GEM stand, the expected collected charge should be calculated to avoid signal cutoff or noise event integration. This parameter, also set in the signal processing chain, is the maximum amount of charge the system can accurately measure without saturation. The following section describes the estimate of the typical signal generated by a minimum ionizing particle (MIP), such as a cosmic muon.

Charge collected by a Triple-GEM upon cosmic muon interaction

In the configuration used for this work, each of the triple-GEM detectors comprises a total effective gas-filled distance (Δx_{total}) of 0.85 mm[1]. A minimum ionizing particle (MIP), such as a muon, loses energy at a rate of approximately $\frac{dE}{dx} \approx 2\,\mathrm{MeV}/(\mathrm{g/cm^2})$ in gas [37]. For an Ar/CO_2 (80/20) mixture at atmospheric pressure, the gas density is approximately $\rho \approx 1.7 \times 10^{-3}\,\mathrm{g/cm^3}$. Therefore, the total energy deposited by a muon over the full gas path is:

$$\Delta E = \left(\frac{dE}{dx}\right) \cdot \rho \cdot \Delta x_{\text{total}} = 2 \cdot 1.7 \times 10^{-3} \cdot 0.85 \approx 2.89\,\mathrm{keV}. \tag{3.4}$$

Given an average ionization energy $W = 26\,\mathrm{eV}$ per electron-ion pair for the Ar/CO_2 mixture, the total number of primary electrons generated is:

$$N_{\text{primary}} = \frac{\Delta E}{W} = \frac{2.89 \times 10^3\,\mathrm{eV}}{26\,\mathrm{eV}} \approx 111\,\text{electrons}. \tag{3.5}$$

After amplification by the triple-GEM, the number of electrons collected at the readout plane is determined by the gain G. In this calculation, we consider a theoretical gain in the range $G = 10^3$ to 5×10^3. Assuming a primary ionization of $N_{\text{primary}} = 111$ electrons and using the elementary charge $e = 1.6 \times 10^{-19}$ C, the total collected charge Q lies within the following range:

- For $G = 10^3$:

$$Q = N_{\text{primary}} \cdot G \cdot e = 111 \cdot 10^3 \cdot 1.6 \times 10^{-19} = 17.8\ \text{pC} \tag{3.6}$$

- For $G = 5 \times 10^3$:

$$Q = 111 \cdot 5 \times 10^3 \cdot 1.6 \times 10^{-19} = 88.8\ \text{pC} \tag{3.7}$$

This result indicates that the expected signal lies within the dynamic range of the DDC264 at [17.8 - 88.8] pC. According to the device specifications, the most suitable range setting is 100 pC. This configuration provides sufficient headroom to accommodate moderate fluctuations in the muon signal due to path variations, gain uniformnesses, or charge sharing among adjacent pads, while preserving adequate resolution and avoiding saturation of the readout board.

[1]Sum of the drift gap, the transfer gaps, and the induction gap distances at Figure 3.3.

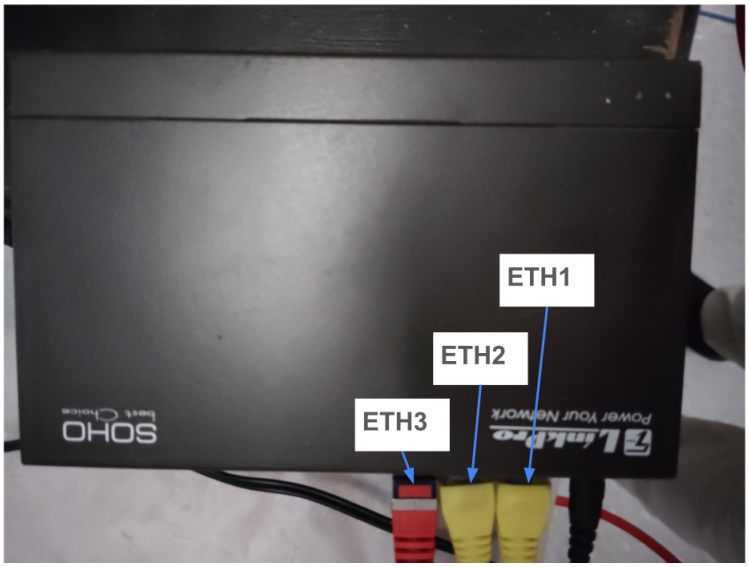

Figure 3.8: An Ethernet switch enables communication between the PC and the GEM stand by interfacing with the readout boards of each triple-GEM detector. As shown in this figure, **ETH1** connects directly to the computer's Ethernet port, while **ETH2** interfaces with the bottom triple-GEM, and **ETH3** with the top triple-GEM, enabling independent data acquisition and control for each module.

3.2.2 Gas Panel

The gas panel consists of argon (Ar) and carbon dioxide (CO_2) gas cylinders, which supply the detector with a predefined gas mixture. A schematic representation of the gas panel is shown in Figure 3.10. The gases pass through their respective outlet regulators (BR-01 and BR-02) and manual opening valves (V-01 and V-02), which are connected to pressure gauges (PG-01 and PG-02) for monitoring the input pressures. From there, the gases flow through 6 mm tubing into independent flow meters (FM-01 and FM-02), which allow the user to measure and adjust the flow rates precisely using control knobs.

The mixture of Ar and CO_2 is essential for the proper operation of the GEM detector. The two gases mix downstream of the flow meters and are then directed via plastic and stainless-steel piping to the triple-GEM chambers. The gas mixture enters the chambers through dedicated inlet ports and exits via gas bubblers (see Figure 4.9), which prevent atmospheric contamination and allow visual confirmation of gas flow.

Figure 3.9: Schematic view of the PC and DAQ electronics. A detailed schematic of the peripherals can be found in Appendix B.3.

Before each measurement,a pre-flush procedure is performed to ensure that the detector volume is fully purged of ambient air or previous gas mixtures. This is achieved by allowing the new mixture to flow through the chambers for several volume exchanges (20 min), ensuring the internal environment reaches a stable composition.

To maintain consistent performance, both pressure and flow must remain stable during operation. This is achieved by adjusting manually the outlet regulators in the gas panel and fine-tuning the control knobs in flow meters until the desired set-points are reached and maintained. During operation, the gas panel is monitored periodically to ensure there are no drifts or leaks. A detailed Piping and Instrumentation Diagram (P&ID) of the gas system is provided in Appendix B, showing the complete layout and control elements used in the gas handling system.

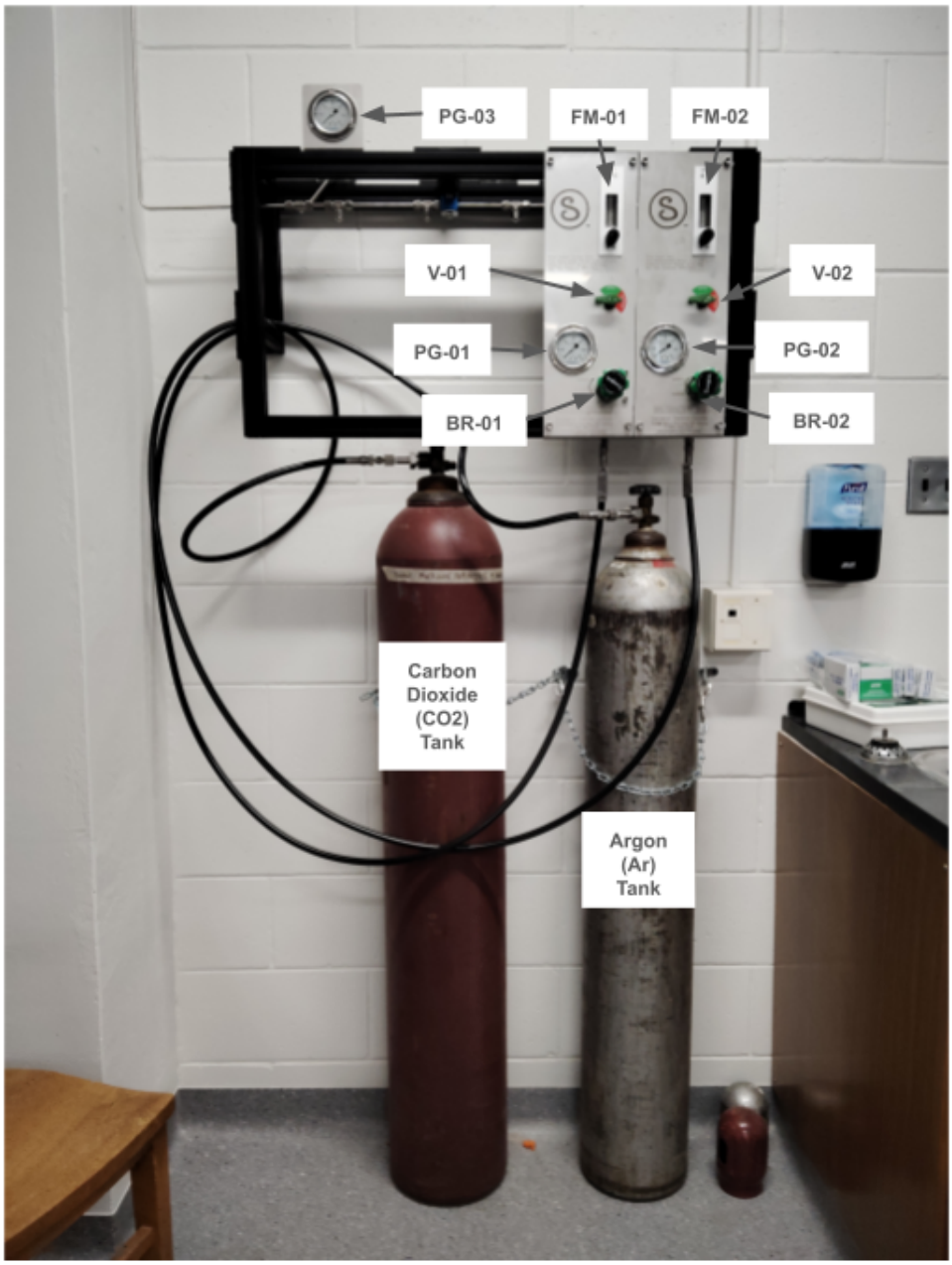

Figure 3.10: The gas panel, and the names of the piping and instrumentation devices.

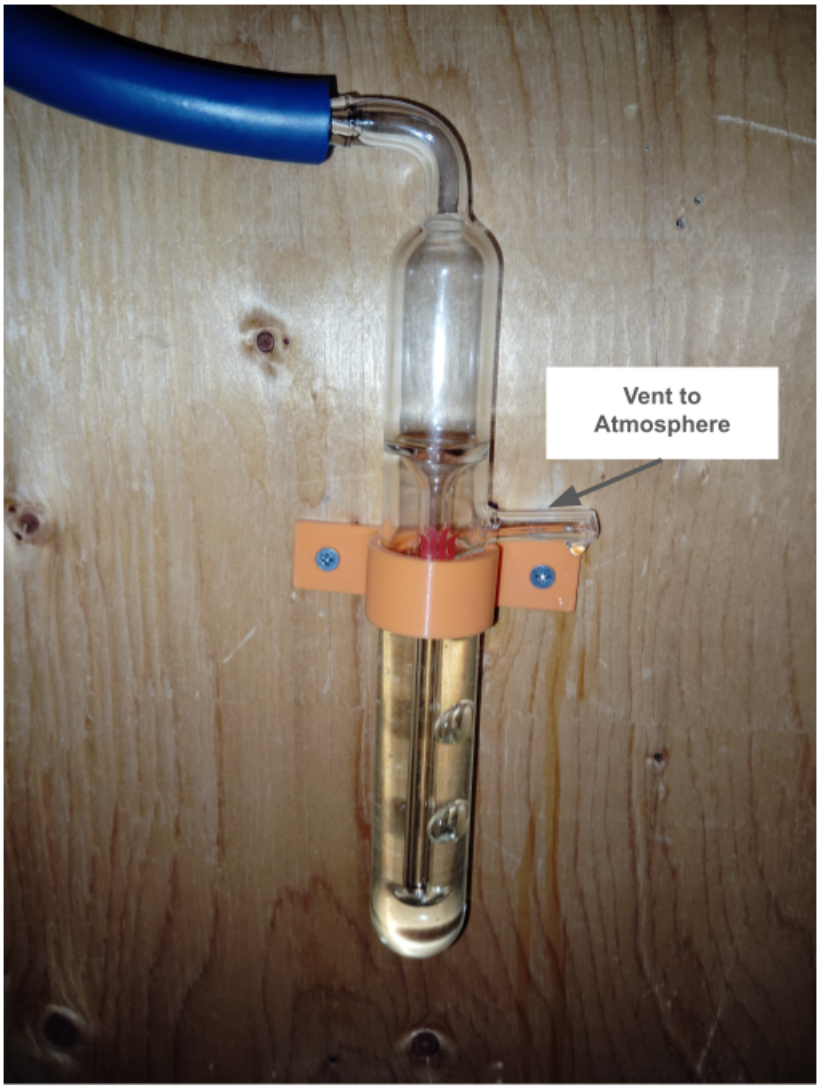

Figure 3.11: Gas bubbler filled with mineral oil to exclude the gas from each of the triple-GEM.

3.3 Gas Mixture

In gaseous detectors such as GEMs, the choice of gas mixture plays a critical role in determining key performance parameters, including gain, energy resolution, operational stability, and the likelihood of electrical discharges. The gas composition directly influences the ionization efficiency, electron transport properties, and quenching behaviour within the detector. Among the most commonly used gas mixtures reported in the literature are **Ar/CO_2 70/30** and **Ar/CO_2 80/20**, which offer a favourable balance between amplification performance and discharge suppression [41].

The target ratio is set by defining the individual flow rates of argon and carbon dioxide as follows:

- CO_2: 0.20 L/min, Ar: 0.50 L/min $\Rightarrow Ar/CO_2 \approx 71.4/28.6 \approx$ **70/30**
- CO_2: 0.12 L/min, Ar: 0.50 L/min $\Rightarrow Ar/CO_2 \approx 80.6/19.4 \approx$ **80/20**

These ratios are set manually using the control knobs of the flow meters located on the gas panel, and the resulting mixture is continuously supplied to the detector chambers under stable flow conditions. The dataset presented in this work was acquired using an **Ar/CO_2 80/20** gas mixture, maintained at a pressure of 15 psi ($\sim$1.02 atm) and a temperature of 18 °C.

Operating the detector at higher pressures is generally not recommended, as it increases the risk of electrical discharges or sparks and imposes additional mechanical stress on the GEM foils. Atmospheric pressure operation offers a safer and more stable configuration, minimizing the likelihood of damage and ensuring reliable detector performance.

3.4 Voltage

To determine the optimal voltage settings for both GEMs, the high voltage was initially set to -3100 V (negative polarity) in the HV power supply (see Figure 3.5) and increased in 20 V increments. At each voltage step, the system was allowed to stabilize for approximately 20 minutes before acquiring data. The current was fixed at 15 μA for all runs, as defined by the high-voltage divider configuration calculated in Section 3.1.1.

The voltage ramping was halted once audible sparks were detected, indicating the onset of electrical discharge and the operational limit of the detector (found at 3340 V). The voltage, current and run durations of the data analyzed in this work, is presented in tables 3.3, and 3.4.

Table 3.3: Summary of operating conditions during the voltage scan for each run in the top triple-GEM.

Run	**Voltage (V)**	**Current (μA)**	**Run duration (s)**
1	3099.8	15.405	603
2	3119.9	15.499	614
3	3139.8	15.597	615
4	3159.8	15.695	617
5	3179.8	15.794	621
6	3199.9	15.892	800
7	3220.0	15.988	613
8	3239.9	16.081	626
9	3259.9	16.181	654
10	3280.0	16.280	668
11	3299.8	16.717	803
12	3319.9	16.709	739
13	3339.9	16.675	846

Table 3.4: Summary of operating conditions during the voltage scan for each run in the bottom triple-GEM.

Run	**Voltage (V)**	**Current (μA)**	**Run duration (s)**
1	3100.0	15.684	716
2	3120.0	15.685	627
3	3140.0	15.686	618
4	3160.0	15.790	607
5	3179.8	15.888	729
6	3199.9	15.985	711
7	3220.0	16.084	779
8	3240.0	16.183	686
9	3260.0	16.282	727
10	3280.0	16.482	762
11	3300.1	16.482	786
12	3320.0	16.594	801
13	3340.0	16.856	770

Chapter 4

Characterization of the Test Stand

This chapter presents the characterization of the test stand comprising two triple-GEM detectors. Section 4.1 describes the data processing chain implemented for signal reconstruction and analysis, including the use of the Techtra® Vis software for event visualization and reconstruction (Section 4.1.1), and the application of the DBSCAN clustering algorithm to define and isolate events (Section 4.1.2). Section 4.2 evaluates the response of the GEM stand to minimum ionizing particles through the analysis of signals produced by cosmic muons. Section 4.3 investigates the response of the detectors to monochromatic X-rays emitted by a Fe-55 calibration source. Section 4.4 presents gas amplification curves obtained by scanning the high-voltage settings, identifying three distinct operational regions: the ionization region (Section 4.4.1), the proportional region (Section 4.4.2), and the Geiger–Müller region (Section 4.4.3). Finally, Section 4.5 discusses the observed limitations in detector performance.

4.1 Data Processing Chain

4.1.1 Event Reconstruction with Techtra® Vis Software

The data acquisition in this study is carried out using the Techtra® DDC software. This software interfaces with each triple-GEM detector via a 100 Mbit/s Ethernet protocol. Once the data is saved in a local computer, it is further processed and analyzed using a custom GEM detector data visualization application (Techtra® Vis Software).

The Techtra® Vis software performs digital triggering on the raw data, enabling the automatic identification of physical events. Each identified event is then reconstructed and localized spatially on the 100 x 100 mm^2 active area of the triple-GEMs (see Figure 4.1).

In addition to spatial reconstruction, the software allows the user to visualize the charge spectrum of the detected events. The processed data can be exported in CSV format for further processing, containing event-by-event information. Each entry includes the following parameters (note: timestamps are not recorded):

- `x_loc_min`: Position of the event along the X direction
- `y_loc_min`: Position of the event along the Y direction
- `x_baricenter`: Centroid of the charge distribution in X direction (Strip Number X $\in [1, 128]$)
- `y_barycenter`: Centroid of the charge distribution in Y direction (Strip Number Y $\in [1, 128]$)
- `charge`: Total charge collected for the event in [pC]
- `period`: Time period identifier or acquisition window index
- `width_x`: Estimated width of the event cluster in the X direction
- `width_y`: Estimated width of the event cluster in the Y direction

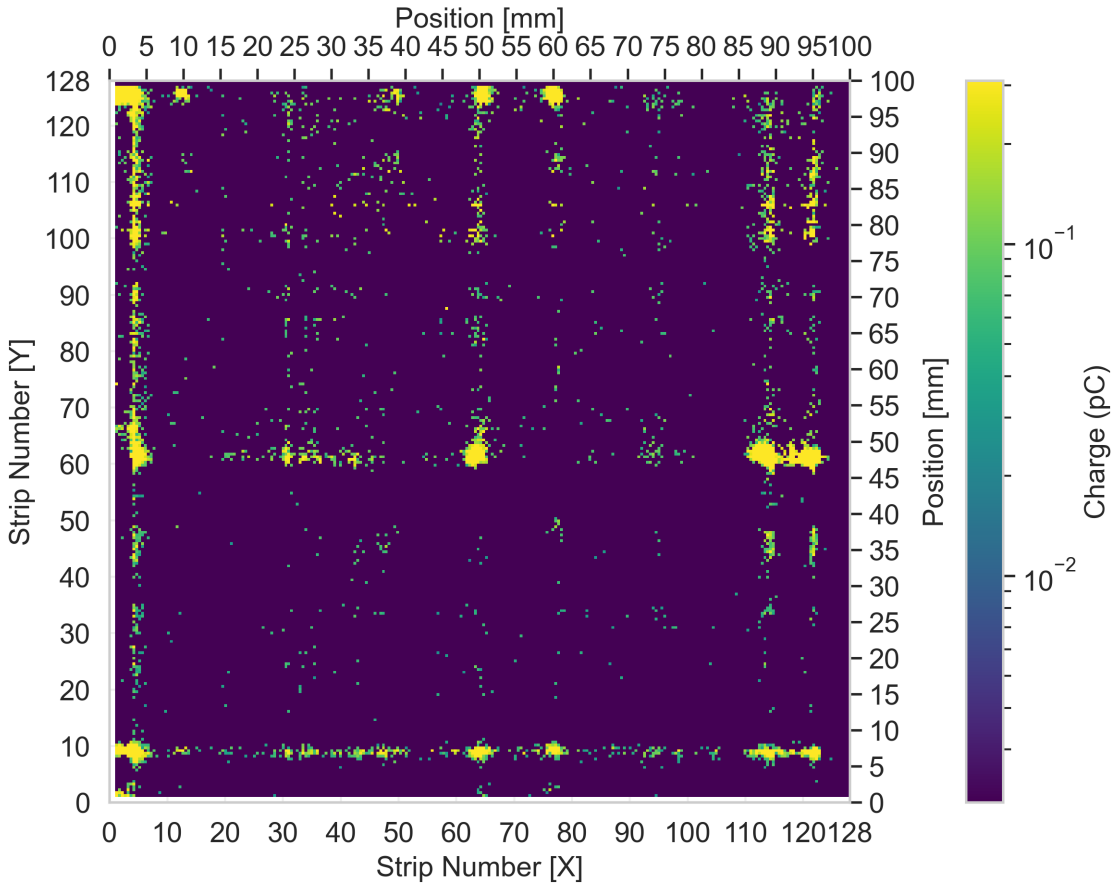

Figure 4.1: 2D spatial reconstruction of events obtained using Techtra® Vis Software. The vertical axis represents the `y_barycenter` (Strip Number [Y]), the horizontal axis the `x_barycenter` (Strip Number [X]), and the color scale reflects the `charge` associated with each reconstructed event.

4.1.2 Event Definition with DBSCAN Algorithm

As shown in Figure 4.1, the 2D spatial maps of the triple-GEM data revealed frequent occurrences of sparse sparks extending across multiple strips. These features made it difficult to distinguish them from events caused by cosmic muons, localized energy deposits such as X-rays, or electronic noise. To reconstruct such events in a robust and flexible manner—including those induced by muons and X-rays—we employed the Density-Based Spatial Clustering of Applications with Noise (DBSCAN) algorithm, as implemented in the scikit-learn machine learning library in Python [53].

DBSCAN is an unsupervised clustering algorithm that identifies clusters as regions of high point density separated by areas of lower density. It requires two input parameters: the neighborhood radius ϵ, which defines the spatial scale at which points are considered neighbors, and `min_samples`, the minimum number of points required to form a dense region. A point is labelled as a core point if it has at least `min_samples` neighbors within its ϵ-radius. Clusters are then formed by expanding from these core points, while isolated points that do not meet the criteria are labelled as noise.

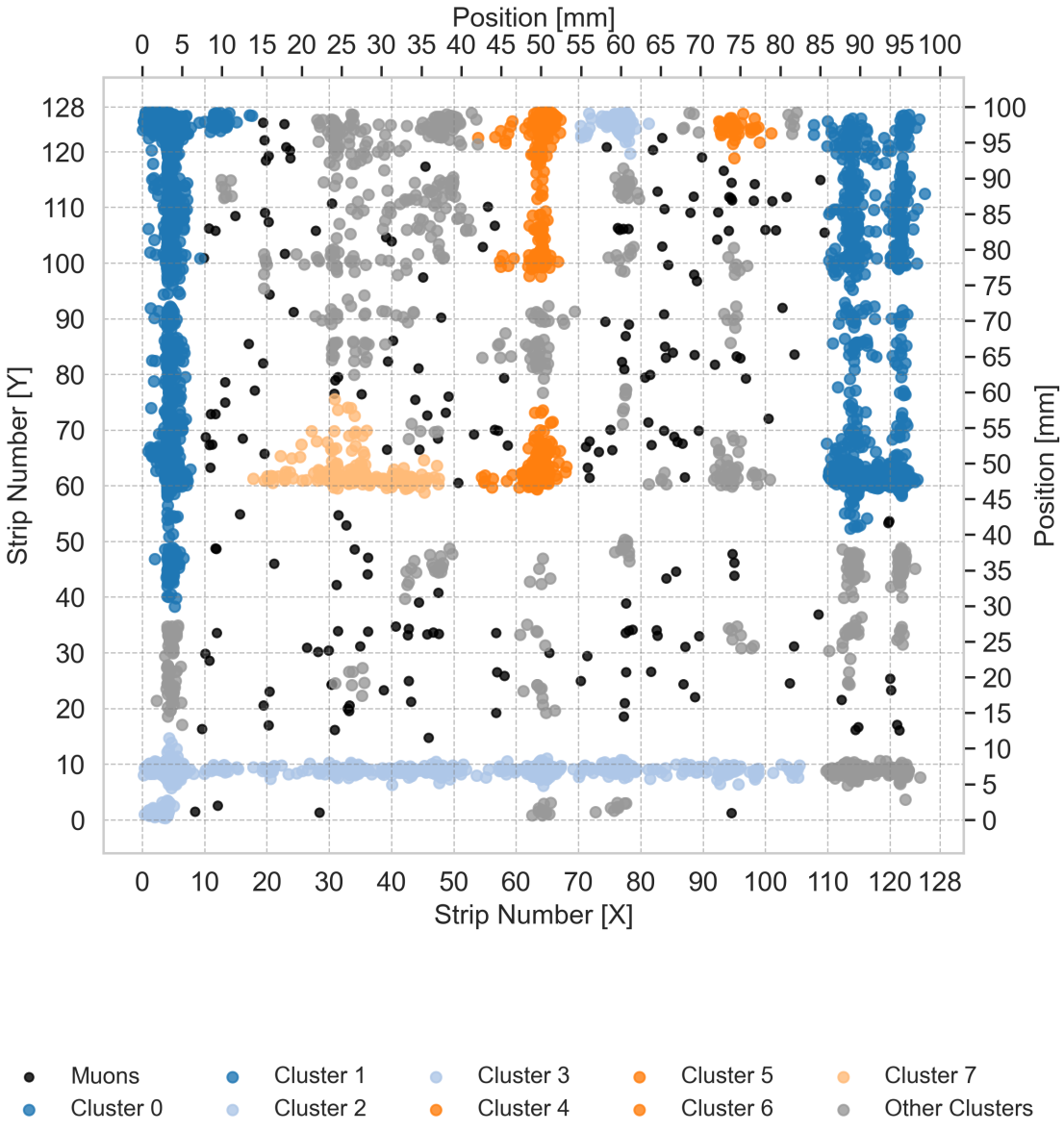

Figure 4.2: Spatial clustering of the data shown in Figure 4.1 after applying the DBSCAN algorithm. Each cluster corresponds to a group of spatially correlated events identified based on their local density in the `x_barycenter`–`y_barycenter` plane.

In our data processing chain, the `x_barycenter` and `y_barycenter` values from each processed data file are used as input features for the DBSCAN clustering algorithm (see Figure 4.2).

The DBSCAN parameters were selected following standard heuristics. For 2D data, the recommended `min_samples` is typically between $D + 1$ and $2D$ (i.e., 3–4 in our case) [53]; we chose `min_samples` $= \mathbf{5}$ to impose slightly stricter density requirements, which improves noise suppression. The neighborhood radius ϵ was selected using the 2D "rule of thumb" $(2D-1)$, yielding $\epsilon = 3$ [54]. With these settings, the algorithm effectively identified distinct spatial regions corresponding to spark-induced clusters, low-density but spatially coherent clusters, and high-density compact clusters.

Based on their spatial features, the low-density coherent clusters were classified as muon tracks (see muons 2D spatial plot in Figure 4.3). In contrast, the high-density compact clusters—located within a rectangular fiducial region enclosing the Fe-55 X-ray source disk positioned above the triple-GEM detector—were identified as X-ray events (see Fe-55 X-rays 2D spatial plot in Figure 4.3). The remaining clusters were associated with spark events due to their location near the detector edges and their significantly higher collected charge compared to regular ionization events (see Cluster 0, 1,2 & 3 in Figure 4.3 and Cluster 5,6,7,9 & 10 in Figure 4.4).

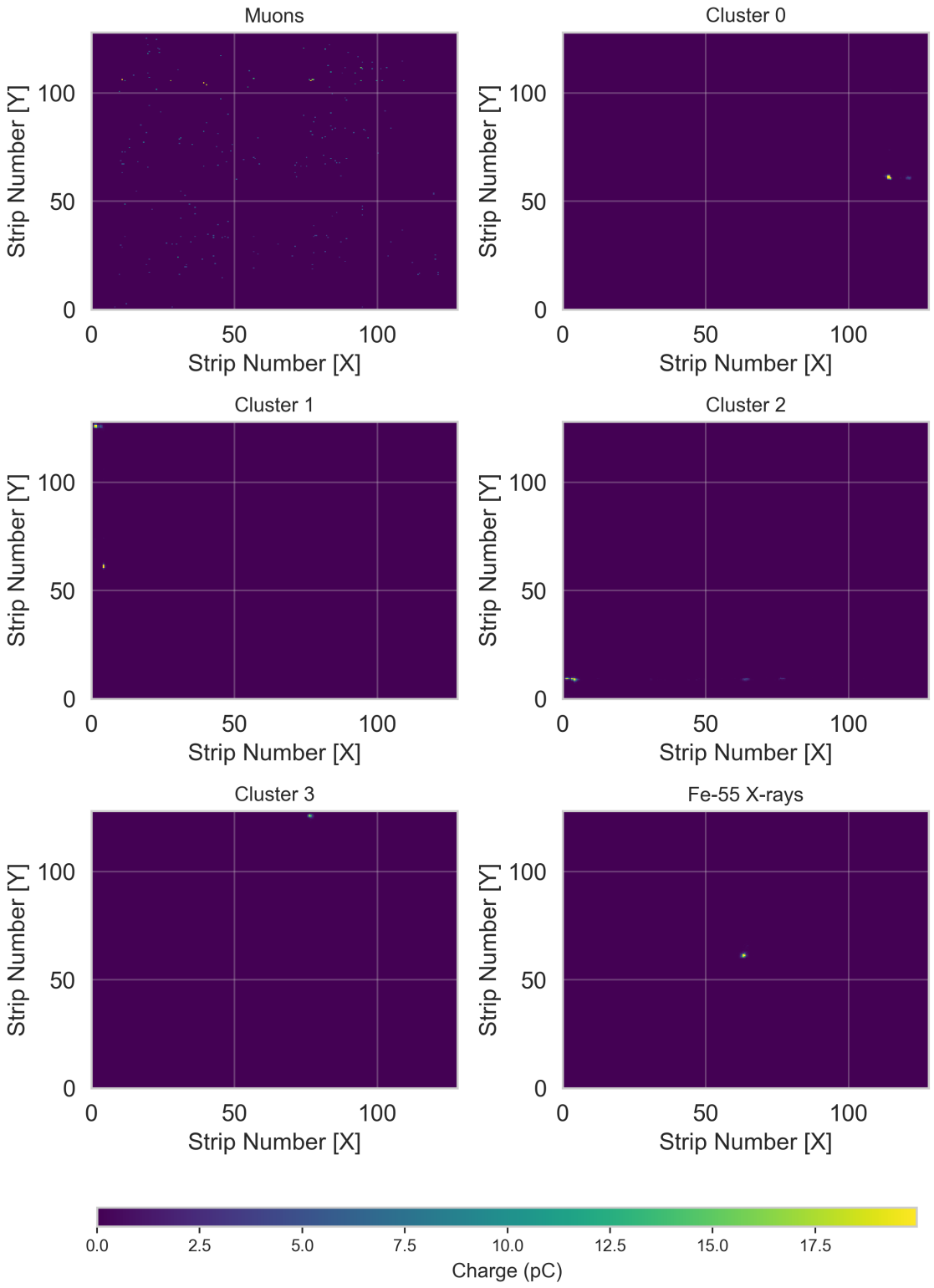

Figure 4.3: Each 2D spatial plot displays the reconstructed positions of event clusters identified by the DBSCAN algorithm in the given triple-GEM. The colorbar represents the total charge collected in each spatial region.

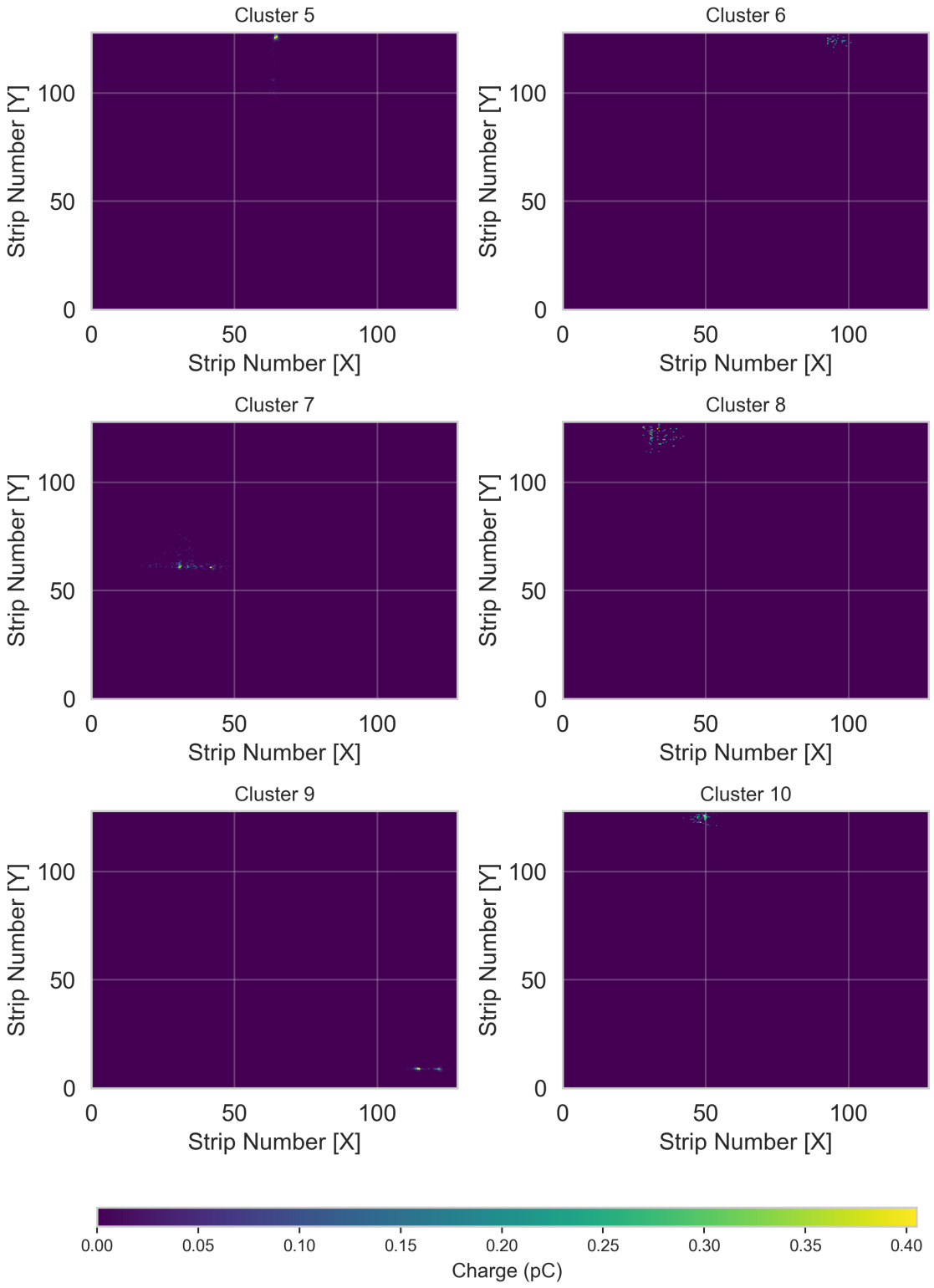

Figure 4.4: Each 2D spatial plot displays the reconstructed positions of event clusters identified by the DBSCAN algorithm in the given triple-GEM. The colorbar represents the total charge collected in each spatial region.

4.2 Response to Cosmic Muons

Cosmic muons are secondary particles produced in the upper atmosphere when high-energy primary cosmic rays —primarily protons and atomic nuclei— interact with atmospheric nuclei. These interactions generate extensive air showers, producing pions and kaons, which subsequently decay into muons. At sea level, the typical vertical flux of muons is approximately 1 muon per square centimeter per minute, with an average energy of about 3–4 GeV [55]. This makes cosmic muons a readily accessible and naturally occurring source of high-energy particles, useful for testing the GEM stand.

To estimate the primary charge produced by a muon in the GEM detector, we take into account the density of the Ar/CO_2 (80:20) gas mixture used in this work. On the other hand, the mass stopping power for muons in Ar/CO_2 (80:20) is approximately:

$$\left(\frac{dE}{dx}\right)_{\text{mass}} \approx 1.5\,\text{MeV}\,\text{g}^{-1}\,\text{cm}^2. \tag{4.1}$$

The density of the gas mixture at standard temperature and pressure (STP) is

$$\rho \approx 1.66\,\text{mg/cm}^3 = 1.66 \times 10^{-3}\,\text{g/cm}^3. \tag{4.2}$$

Thus, the energy loss per unit path length is:

$$\left(\frac{dE}{dx}\right) = \left(\frac{dE}{dx}\right)_{\text{mass}} \cdot \rho = 1.5 \times 1.66 \times 10^{-3} = 2.49 \times 10^{-3}\,\text{MeV/cm} = 2.49\,\text{keV/cm} \tag{4.3}$$

For a muon traversing vertically the triple-GEM chamber height ($x = 0.85$ cm), the total energy deposited is:

$$E_{\text{deposited}} = \left(\frac{dE}{dx}\right) \cdot x = 2.49\,\text{keV/cm} \cdot 0.85\,\text{cm} = 2.12\,\text{keV} \tag{4.4}$$

Assuming an average ionization energy of $W = 26\,\text{eV}$, the number of electron-ion pairs generated is:

$$N_{\text{pairs}} = \frac{E_{\text{deposited}}}{W} = \frac{2.12 \times 10^3\,\text{eV}}{26\,\text{eV}} \approx 82. \tag{4.5}$$

Each pair contributes an elementary charge $e = 1.602 \times 10^{-19}\,\mathrm{C}$, so the total primary charge is:

$$Q_{\mathrm{primary}} = N_{\mathrm{pairs}} \cdot e = 82 \cdot 1.602 \times 10^{-19}\,\mathrm{C} = 1.31 \times 10^{-17}\,\mathrm{C} = 0.013\,\mathrm{fC} \tag{4.6}$$

The amplified charge, also referred to as the total collected charge, corresponds to the sum of electrons produced after the initial ionization and their subsequent multiplication within the GEM detector. When the muon interacts with the gas, it generates primary ionization electrons which drift toward the GEM foils. As these electrons pass through the high-electric field regions within the GEM holes, they undergo avalanche multiplication, producing a much larger number of secondary electrons. This process results in a measured signal (see Figure 4.5). The total charge Q_{total} collected at the readout is related to the primary charge $Q_{primary}$ by the effective gas gain G, such that $Q_{total} = G \cdot Q_{primary}$. For instance, the $Q_{primary}$ calculated in Equation 4.6, when compared with the Q_{total} extracted from the MPV in Figure 4.6, yields a gain value of

$$G_{muons} = \left(\frac{Q_{total}}{Q_{primary}}\right) = \left(\frac{52.89 fC}{0.013 fC}\right) = 4.068 \times 10^{3}. \tag{4.7}$$

Similarly, G is extracted for all the charge distributions of muon events in each of the triple-GEM detectors under the voltage settings listed in Tables 3.3 and 3.4 (see Appendix D). These values are used in Section 4.4 to obtain the gas amplification curves for each detector.

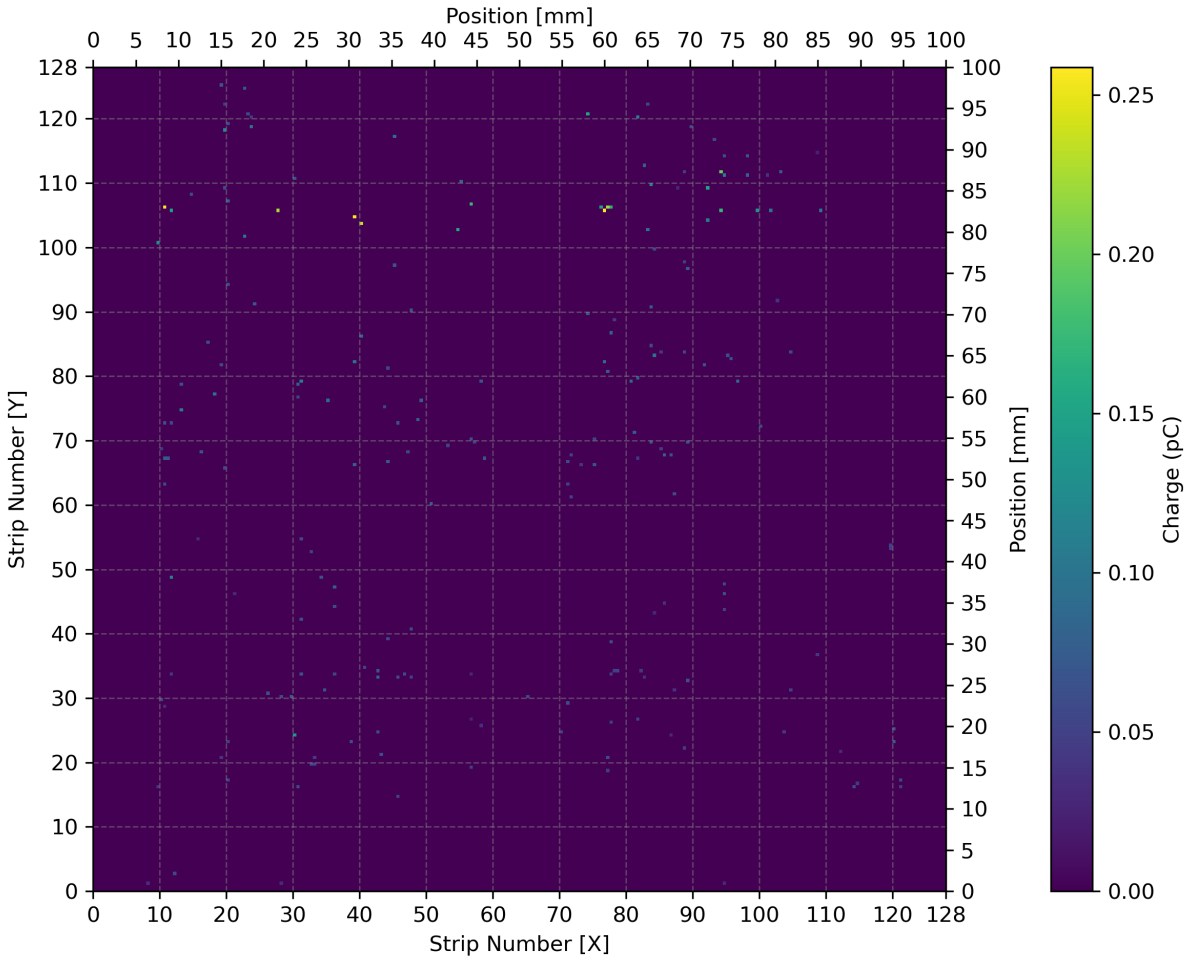

Figure 4.5: The heatmap illustrates the spatial distribution of muons, with color intensity representing the total accumulated charge in the triple-GEM active area.

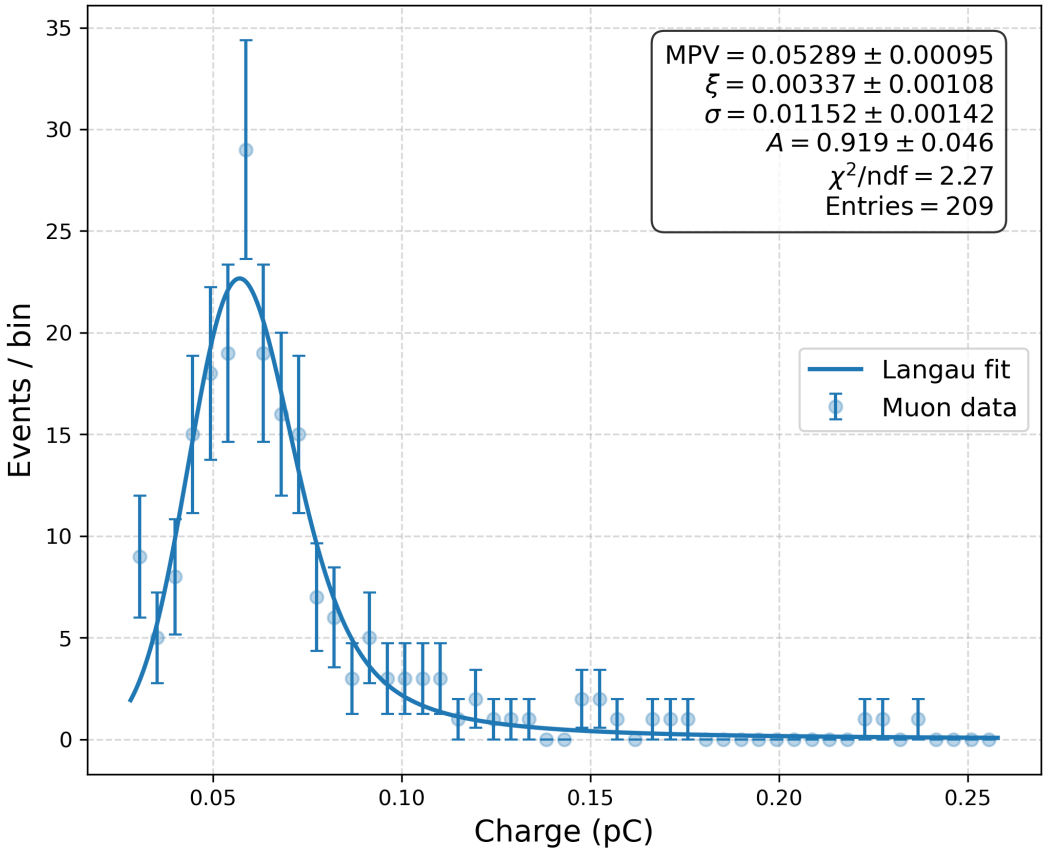

Figure 4.6: Charge distribution of the muon events registered by the triple-GEM, reflecting the typical energy deposition profile of muons traversing matter. The distribution follows a Landau function convoluted with a Gaussian (Langau function), accounting for both stochastic energy loss and the finite resolution of the detector.

4.3 Response to Fe-55 X-rays

Fe-55 or Iron-55 is a radioactive isotope used as a source of X-rays. Fe-55 undergoes electron capture, a process where an electron from the innermost shell is captured by the nucleus, leading to the emission of characteristic X-rays [56] [57]. With a half-life of approximately 2.73 years, the decay of Fe-55 results in the emission of monoenergetic X-rays of 5.9 keV, corresponding to transitions between the K and L electron shells. The decay equation is shown in equation 4.8,

$$^{55}_{26}\mathrm{Fe} + {}^{-1}_{0}\beta \longrightarrow {}^{55}_{25}\mathrm{Mn} + \text{X-Ray (5.9 keV)} \tag{4.8}$$

An Iron-55 source acquired with Canberra® in March 2020 with an activity of 100 μC was put on the top windows of the GEMs (see Figure 4.7).

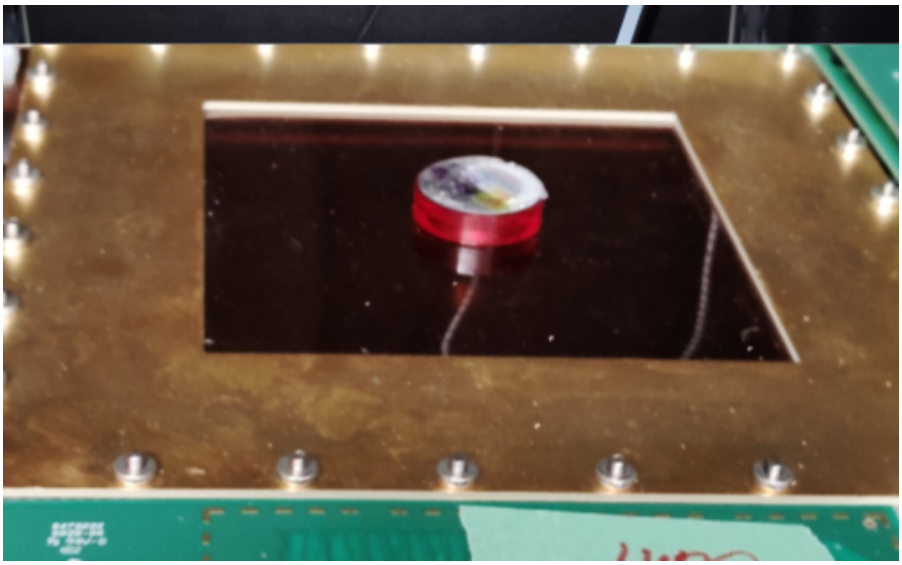

Figure 4.7: In the Figure, the Fe-55 source appears as a red disk of 1-inch diameter and is positioned approximately at the geometric centre of the top window of the triple-GEM detector's active area.

The primary charge produced in the triple-GEMs by the Fe-55 radioactive source can be estimated using the known energy of the emitted X-rays and the average ionization energy of the gas mixture.

The Fe-55 source emits photons with an energy of

$$E_{\mathrm{Fe-55}} = 5900\,\mathrm{eV}. \tag{4.9}$$

When these photons interact with the gas in the detector, they ionize gas molecules creating electron-ion pairs. The average energy required to produce a single electron-ion pair in the Ar/CO_2 (80/20) mixture is

$$W = 26\,\text{eV/pair}. \tag{4.10}$$

The number of primary electron-ion pairs generated by each Fe-55 photon can be calculated by dividing the photon energy by the ionization energy:

$$N_{primary} = \frac{E_{\text{Fe}-55}}{W} = \frac{5900}{26} \approx 227. \tag{4.11}$$

Each electron-ion pair carries an elementary charge given by

$$e = 1.602 \times 10^{-19}\,\text{C}. \tag{4.12}$$

Thus, the total primary charge Q_{primary} generated by the ionization from a single photon is the product of the number of pairs and the elementary charge:

$$Q_{primary} = N_{primary} \times e = 227 \times 1.602 \times 10^{-19}\ \text{C} = 3.63 \times 10^{-17}\ \text{C} = 0.0363\ \text{fC} \tag{4.13}$$

This primary charge represents the initial ionization charge deposited in the gas before any amplification occurs in the triple-GEM detector. Therefore, the gain G_{Fe-55} can be obtained from the $Q_{primary}$ calculated in equation 4.13 and the Q_{total} obtained from the μ value extracted from Figure 4.8. With these values the gain is:

$$G_{Fe-55} = \left(\frac{Q_{total}}{Q_{primary}}\right) = \left(\frac{176.8\ fC}{0.0363\ fC}\right) = 4.87 \times 10^3. \tag{4.14}$$

The differences between G_{Fe55} and G_{muons} arises because X-rays deposit their energy in a localized manner, resulting in a higher density of ionization and consequently a larger number of primary electron-ion pairs within the detector's sensitive volume. In contrast, muons, being minimum ionizing particles, lose energy more gradually along their tracks, leading to fewer ion pairs per unit length and thus a smaller primary charge.

Similarly, G_{Fe-55} is extracted from the charge distributions of Fe-55 X-rays in each of the triple-GEM detectors under the voltage settings listed in Tables 3.3 and 3.4 (see Appendix D). Unfortunately, the DBSCAN algorithm was unable to isolate the Fe-55 X-ray events in the top triple-GEM due to significant overlap with high-density spark events occurring in the region beneath the Fe-55 source disk.

The G_{Fe-55} values obtained for the bottom triple-GEM are used in Section 4.4 to construct the gas amplification curve for this specific detector and operating conditions.

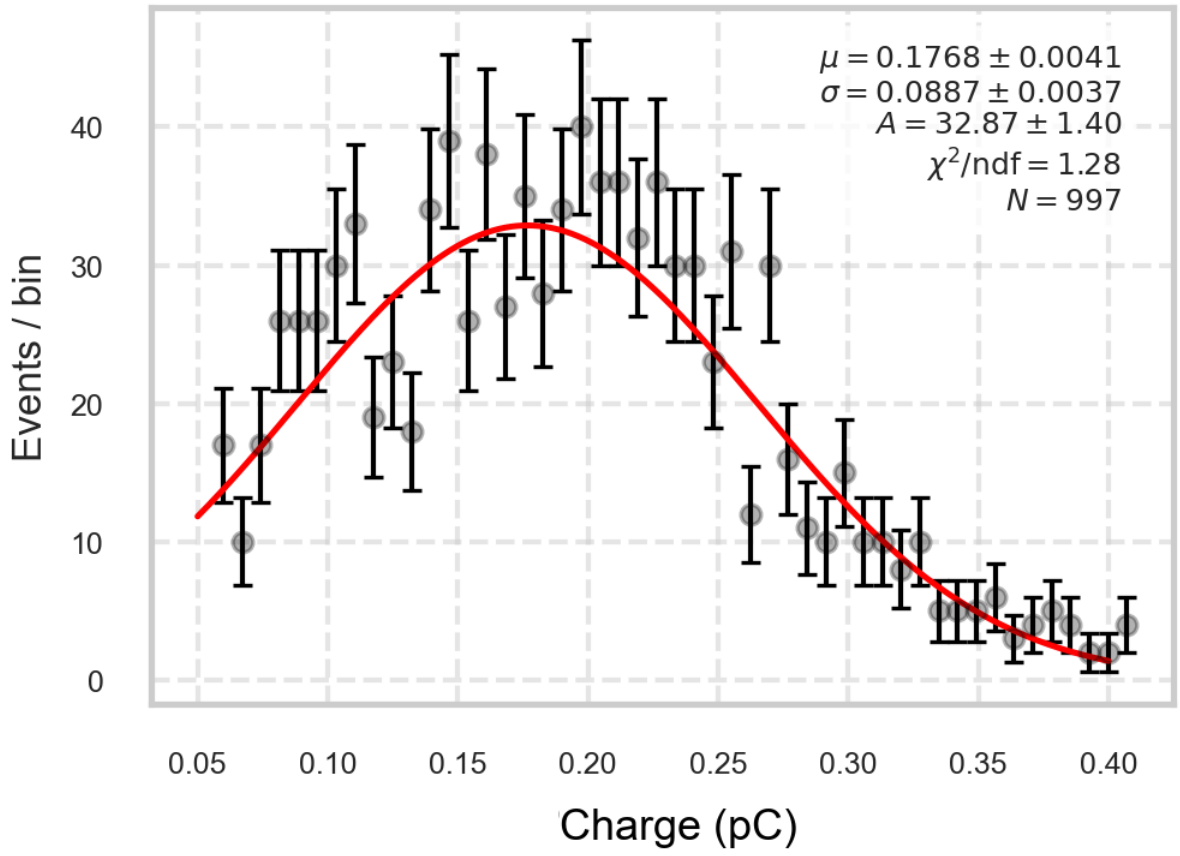

Figure 4.8: Charge distribution of Fe-55 events as registered by the triple-GEM. The distribution follows a Gaussian profile, with its mean value corresponding to the average charge collected from the 5.5 keV X-ray ionization within the triple-GEM chamber.

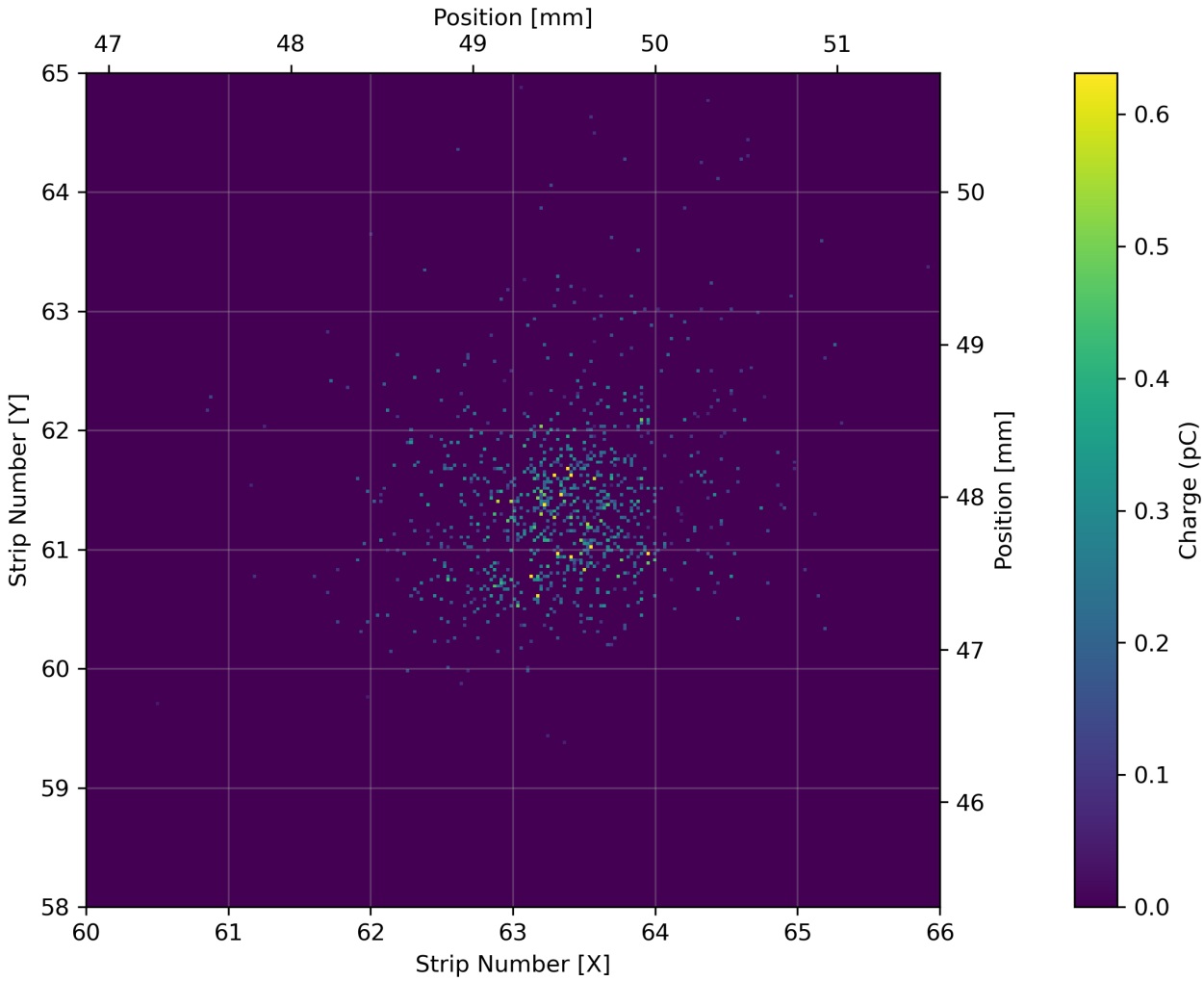

Figure 4.9: The heatmap illustrates the spatial distribution of interactions from monoenergetic 5.5 keV X-rays in the triple-GEM, forming a high-density, compact cluster. The color intensity represents the total accumulated charge in the region directly beneath the source. The overall central position of this cluster is consistent with the expected location of the source. For reference, see the 2D spatial plot of Fe-55 X-rays in Figure 4.3.

4.4 Gas Amplification Curves

The gas amplification curve of a triple-GEM detector characterizes the relationship between the applied voltage across the GEM foils and the number of ion-electron pairs created (i.e, the total collected charge or gain). For the pair of GEMs, three distinct regions were identified in the gas amplification curve (see Figure 4.10 for the top triple-GEM, and Figure 4.11 for the bottom triple-GEM).

4.4.1 Ionization Region (3100 - 3250 V):

In the ionization region, the gain in the triple-GEM detectors remains approximately constant because the fraction of ion-electron pairs that recombine before being collected—the so-called recombination region—is negligible. At these field strengths, the electric field is already sufficient to efficiently separate ion pairs, minimizing recombination and ensuring stable charge collection.

In this regime, muons exhibit a higher observed gain than Fe-55. As minimum ionizing particles (MIPs), muons traverse the entire active volume of the gas detector, continuously ionizing the medium along their path and generating a relatively large number of primary electrons. In contrast, Fe-55 emits monoenergetic 5.9 keV X-rays that interact locally, depositing their energy in a confined region and producing significantly fewer primary electrons.

4.4.2 Proportional Region (3240 - 3300 V):

As the applied voltage increases and the triple-GEM enters the proportional region, the collected charge (i.e., gain) begins to rise due to avalanche formation. In this regime, the electric field is strong enough that electrons from primary ionization acquire sufficient kinetic energy between collisions to produce additional ionization, leading to charge multiplication. Since the total collected charge becomes proportional to the initial ionization, this region enables both particle identification and energy measurement.

The gain in this proportional regime can be described by the exponential model [41]:

$$G(V) = G_0 e^{\alpha V}, \tag{4.15}$$

where G_0 is a model parameter constant and, α characterizes the rate at which gain increases with the applied voltage. In this study, the fitted values of α for muons were found to be $0.0079V^{-1}$ for the bottom triple-GEM and $0.0037V^{-1}$ for the top triple-GEM.

As gas amplification becomes the dominant contributor to signal amplitude, the response to different ionizing sources diverges. The localized ionization from Fe-55 becomes increasingly advantageous: the compact cluster of primary electrons experiences a more uniform and concentrated electric field, promoting efficient avalanche multiplication.

Moreover, Fe-55 interactions are more uniform and stable in energy deposition, resulting in a steeper gain curve compared to the distributed ionization from muons.

At an applied voltage of 3260 V in the bottom triple-GEM, the gain from Fe-55 surpasses that of muons. This crossover point marks the transition where the gas multiplication efficiency for the localized Fe-55 ionization overtakes the initially higher ionization yield of traversing muons. A similar conclusion could not be drawn for the top triple-GEM due to the inability to extract the Fe-55 signal from data contaminated by sparks.

4.4.3 Geiger–Müller Region (3300 - 3340 V):

In this region, the electric field inside the triple-GEM holes is sufficiently strong that a single electron-ion pair generated in the drift region can initiate an avalanche multiplication process. If the applied voltage is increased beyond this regime, the detector may enter a continuous discharge mode, rendering the triple-GEM non-functional. This upper limit was not explored beyond 3240 V in the present study in order to preserve the integrity and operational stability of the triple-GEMs.

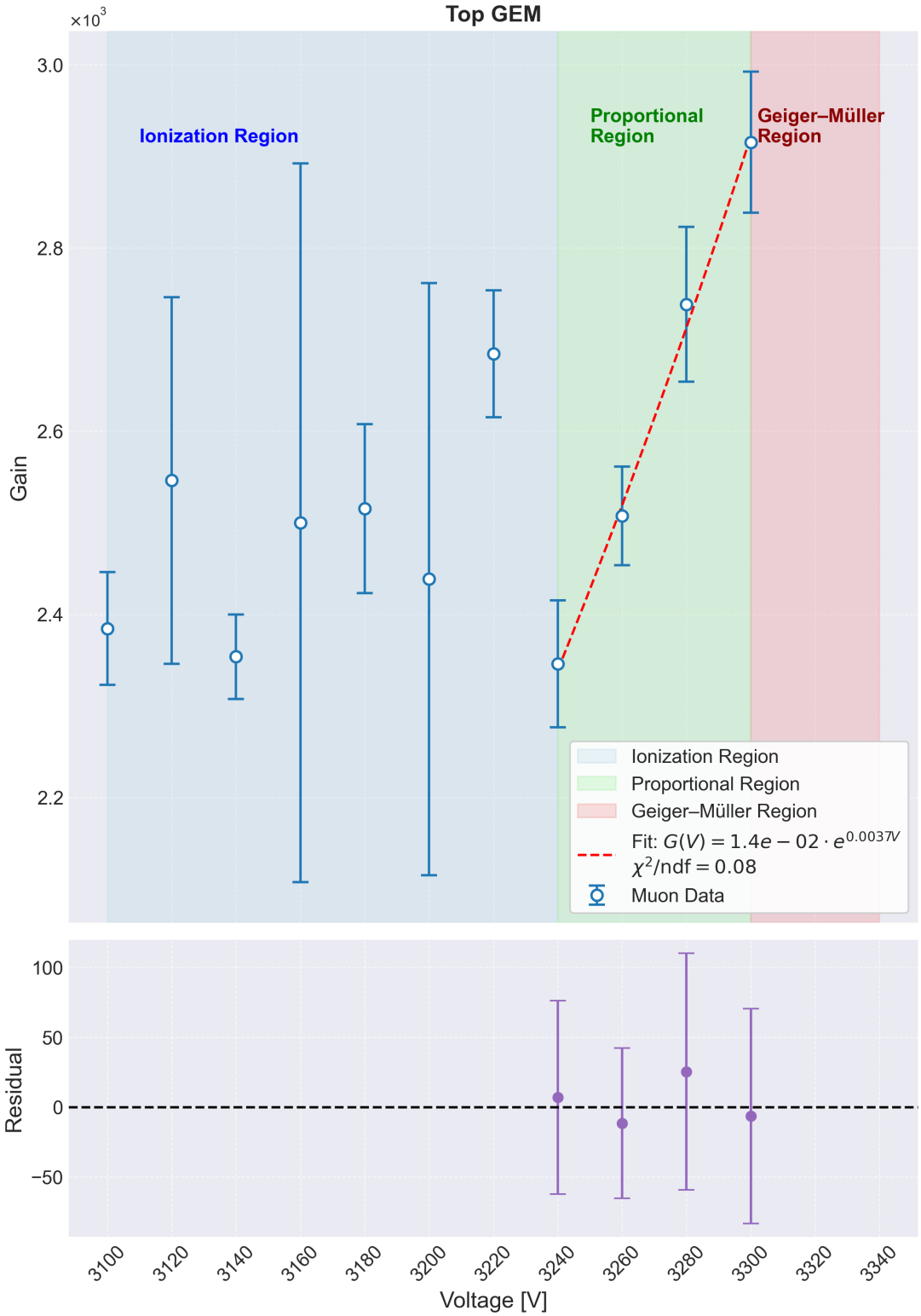

Figure 4.10: Gain curve for the top triple-GEM.

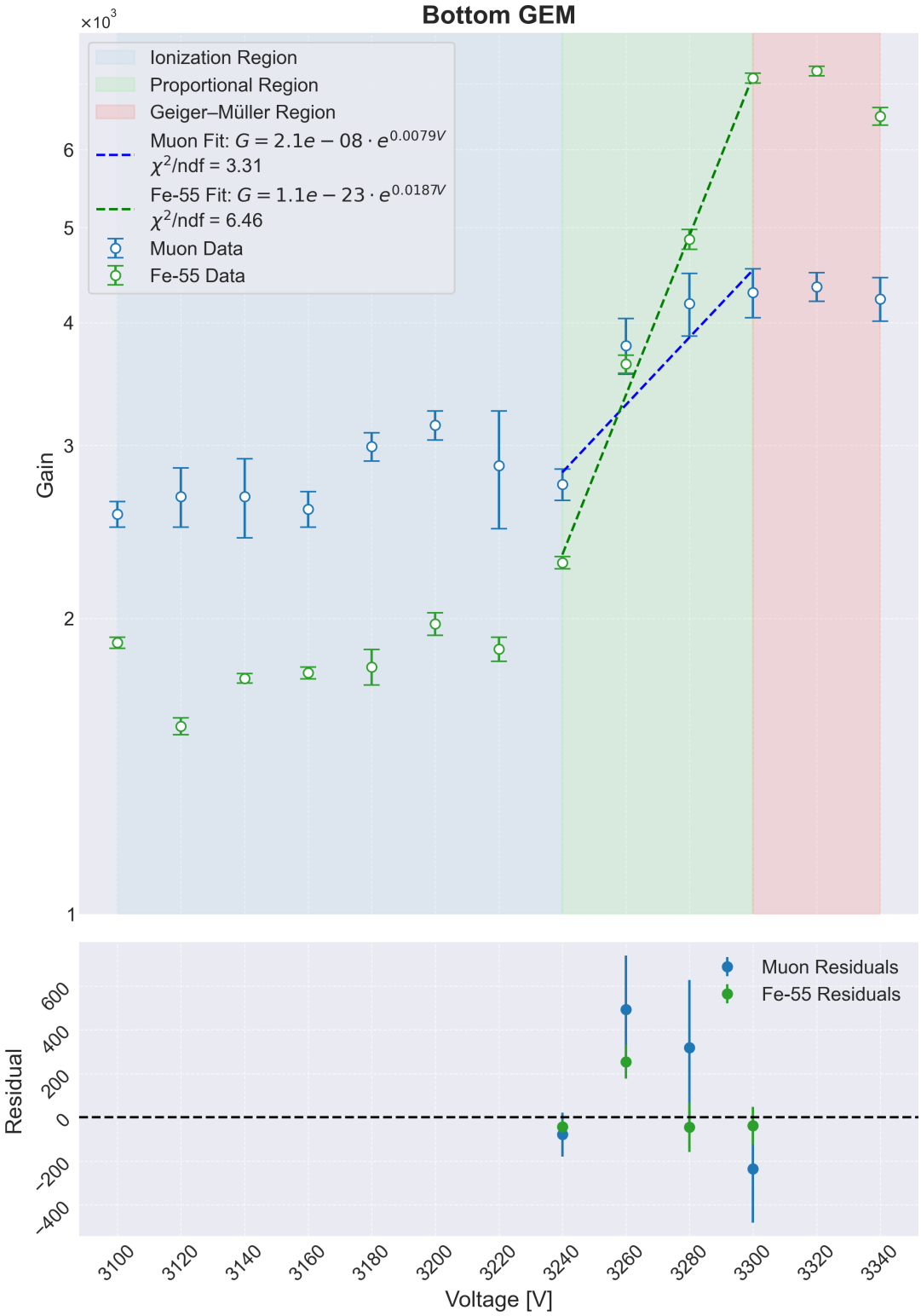

Figure 4.11: Gain curve for the bottom triple-GEM.

4.5 Detector Limitations

While proceeding with tests of the triple-GEM detectors using a Sr-90 source (to test sensitivity to β radiation) and aiming to explore the gas amplification curve for the **Ar/CO$_2$ 70/30** gas mixture, the bottom triple-GEM suddenly stopped responding and ceased to produce data. After extensive troubleshooting to isolate the cause of the malfunction, it was determined that the issue could not be resolved on-site. Consequently, the detector was shipped to Techtra® for inspection and repair.

Upon inspection, Techtra® technicians determined that the bottom triple-GEM was not functional. Their visual examination indicated that the detector had likely been damaged by microscopic dust particles, which caused repeated sparking (see Figure 4.12). These discharges compromised the internal GEM foils and rendered the detector unstable. As a result, no reliable data could be acquired from this detector, and it was excluded from subsequent analysis.

All results presented in this chapter—including the response to cosmic muons and Fe-55 X-rays, as well as the gas amplification curves—were obtained using the bottom triple-GEM detector and top triple-GEM while it remained fully operational throughout the experiment.

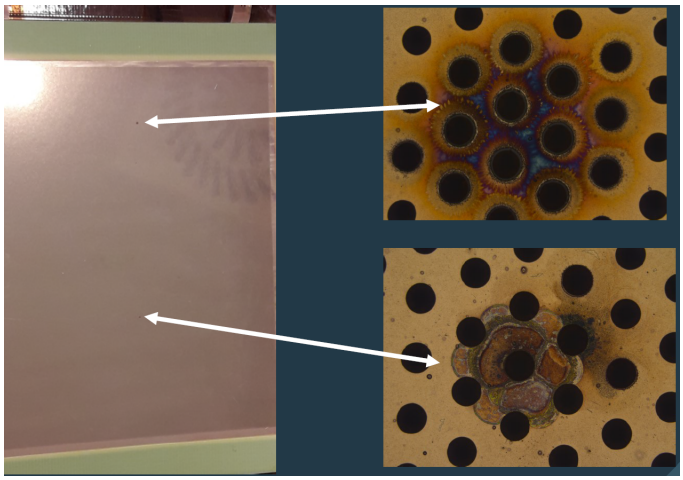

Figure 4.12: Microscopic inspection of the top triple-GEM revealed several visible defects in the GEM foils. As shown in the images on the left, localized thermal damage to the Kapton layer is apparent, which likely contributed to repeated sparking and operational failure (Figure courtesy of Techtra®).

Chapter 5

Conclusions and Future Work

A GEM stand, constructed using two commercial Triple Gas Electron Multipliers (triple-GEMs), has been commissioned and characterized using an Fe-55 X-ray monoenergetic source as well as cosmic muons. The experimental setup was assembled at the University of Manitoba. This test stand represents a novel configuration and remains under active development.

During the operation and commissioning phase with an $\mathbf{Ar/CO_2}$ **80/20** gas mixture, gas amplification curves were obtained for both triple-GEM detectors. A common proportional region was identified within the voltage range of 3240 V to 3300 V at an operating current of 15 μA. In this region, gains on the order of 10^3 were achieved. A breakdown voltage of approximately 3340 V was observed, beyond which spark discharges occurred.

To enhance the tracking and identification of cosmic muons, a coincidence unit has been acquired to interface with both triple-GEMs. This will enable unambiguous identification of cosmic muon events and facilitate not only their detection but also studies of the solid angle dependence of detectors placed in between—such as the HVMAPS detector shown in Figure 5.1. In addition, efforts are underway to improve the DBSCAN event clustering algorithm in order to enhance signal-to-background separation, reduce false positives, and achieve more accurate reconstruction of particle interactions within the triple-GEMs.

A pair of plastic scintillation detectors with photomultiplier readout is also planned for installation, to serve as a secondary trigger in coincidence with the GEM test stand and thus improve the ability to distinguish cosmic muons (see the proposed setup in Appendix C.1).

While the MOLLER collaboration anticipates the full assembly of its major subsystems by mid-2026 and the start of physics data-taking in fall 2027, the GEM test stand is on track to contribute to the spatial resolution characterization of the HVMAPS sensors within the main integration module—ensuring that the experiment's particle tracking and Møller scattering event reconstruction requirements are met.

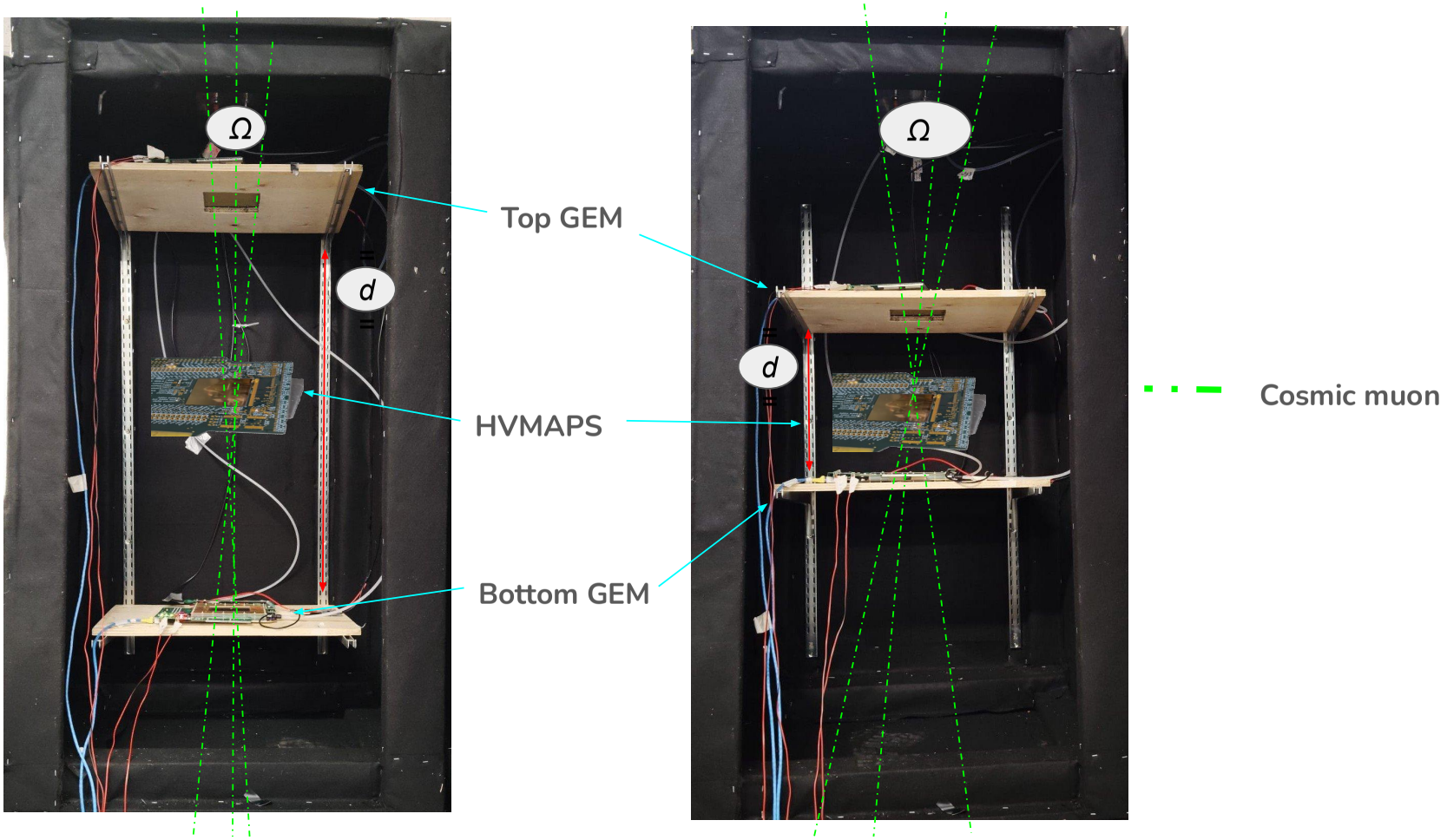

Figure 5.1: By varying the separation distance (d) between the triple-GEMs, we can investigate the solid angle dependence (Ω) of cosmic muons traversing both the triple-GEMs and the HVMAPS simultaneously. This will allow to analyze the muon scattering pattern, which can then be extrapolated to model electron scattering profiles in the HVMAPS.

References

[1] Symmetry Magazine, *The Deconstructed Standard Model Equation*, Accessed: 2024-09-19, 2023. [Online]. Available: https://www.symmetrymagazine.org/article/the-deconstructed-standard-model-equation?language_content_entity=und. 1

[2] F. H. et al., "Observation of Neutrino-like Interactions without Muon or Electron in the Gargamelle Neutrino Experiment," *Nuclear Physics B*, vol. 73, pp. 0–22, 1 1974, ISSN: 0550-3213. DOI: 10.1016/0550-3213(74)90038-8. 2, 7

[3] G. A. et al., "Experimental Observation of Lepton Pairs of Invariant Mass around 95 GeV/c2 at the CERN SPS Collider," *Physics Letters B*, vol. 126, pp. 398–410, 5 1983, ISSN: 0370-2693. DOI: 10.1016/0370-2693(83)90188-0. 2, 7

[4] CMS Collaboration, "Observation of a New Boson at a Mass of 125 GeV with the CMS Experiment at the LHC," *Physics Letters B*, vol. 716, no. 1, pp. 30–61, 2012, ISSN: 0370-2693. DOI: 10.1016/j.physletb.2012.08.021. 2

[5] ATLAS Collaboration, "Observation of a New Particle in the Search for the Standard Model Higgs boson with the ATLAS Detector at the LHC," *Physics Letters B*, vol. 716, no. 1, pp. 1–29, 2012, ISSN: 0370-2693. DOI: 10.1016/j.physletb.2012.08.020. 2

[6] S. Weinberg, "Essay: Half a Century of the Standard Model," *Phys. Rev. Lett.*, vol. 121, p. 220 001, 22 Nov. 2018. DOI: 10.1103/PhysRevLett.121.220001. [Online]. Available: https://link.aps.org/doi/10.1103/PhysRevLett.121.220001. 2

[7] A. Purcell, "Go on a Particle Quest at the First CERN Webfest," no. 35/2012, p. 10, 2012. [Online]. Available: https://cds.cern.ch/record/1473657. 2

[8] J. L. Feng, "Dark Matter Candidates from Particle Physics and Methods of Detection," *Annual Review of Astronomy and Astrophysics*, vol. 48, no. 1, pp. 495–545, 2010. DOI: 10.1146/annurev-astro-082708-101659. [Online]. Available: https://doi.org/10.1146/annurev-astro-082708-101659. 2

[9] M. C. González-García and Y. Nir, "Neutrino Masses and Mixing: Evidence and Implications," *Reviews of Modern Physics*, vol. 75, no. 2, pp. 345–402, 2003. DOI: 10.1103/RevModPhys.75.345. [Online]. Available: https://doi.org/10.1103/RevModPhys.75.345. 2

[10] A. Riotto and M. Trodden, "Recent Progress in Baryogenesis," *Annual Review of Nuclear and Particle Science*, vol. 49, pp. 35–75, 1999. DOI: 10.1146/annurev.nucl.49.1.35. [Online]. Available: https://doi.org/10.1146/annurev.nucl.49.1.35. 2

[11] D. P. A. e. al., "Measurement of the Positive Muon Anomalous Magnetic Moment to 127 ppb," *Phys. Rev. Lett.*, pp. –, Jul. 2025. DOI: 10.1103/7clf-sm2v. [Online]. Available: https://link.aps.org/doi/10.1103/7clf-sm2v. 3

[12] G. Ross, *Grand Unified Theories* (Frontiers in Physics). Benjamin-Cummings Pub Co, 1984, ISBN: 9780805369670,0805369678. 3

[13] Particle Physics Project Prioritization Panel (P5), *Exploring the Quantum Universe: Pathways to Innovation and Discovery in Particle Physics*, https://www.usparticlephysics.org/2023-p5-report/, Accessed: 2025-07-29, 2023. 3

[14] M. Thomson, *Modern Particle Physics*. Cambridge University Press, 2013, ISBN: 978-1-107-03426-6. 3

[15] H. Becquerel, *Nobel Lectures in Physics (Vol 1)*. World Scientific Pub Co Inc, 1998, ISBN: 9789810234010, 9810234015. 3

[16] J. Chadwick, "The Intensity Distribution in the Magnetic Spectrum of β Particles from Radium (B + C)," *Verhandlungen der Deutschen Physikalischen Gesellschaft*, vol. 16, pp. 383–391, 1914. 3

[17] T. D. Lee, M. Rosenbluth, and C. N. Yang, "Interaction of Mesons with Nucleons and Light Particles," *Physical Review*, vol. 75, no. 5, p. 905, 1949, ISSN: 0031-899X. DOI: 10.1103/PhysRev.75.905. 4

[18] T.-D. Lee and C.-N. Yang, "Question of Parity Conservation in Weak Interactions," *Physical Review*, vol. 104, no. 1, pp. 254–258, 1956. DOI: 10.1103/PhysRev.104.254. [Online]. Available: https://doi.org/10.1103/PhysRev.104.254. 4

[19] C. S. Wu, E. Ambler, R. W. Hayward, D. D. Hoppes, and R. P. Hudson, "Experimental Test of Parity Conservation in Beta Decay," *Physical Review*, vol. 105, no. 4, pp. 1413–1415, 1957, ISSN: 0031-899X. DOI: 10.1103/PhysRev.105.1413. [Online]. Available: https://doi.org/10.1103/PhysRev.105.1413. 4

[20] M. R. Francis, "Madame Wu and the Backward Universe," *Galileo's Pendulum*, [Online]. Available: https://galileospendulum.org/2014/03/08/madame-wu-and-the-backward-universe/. 5

[21] S. L. Glashow, "Partial-Symmetries of Weak Interactions," *Nuclear Physics*, vol. 22, no. 4, pp. 579–588, 1961, ISSN: 0029-5582. DOI: 10.1016/0029-5582(61)90469-2. [Online]. Available: https://doi.org/10.1016/0029-5582(61)90469-2. 6

[22] S. Weinberg, "A Model of Leptons," *Physical Review Letters*, vol. 19, pp. 1264–1266, 21 1967, ISSN: 0031-9007,1079-7114. DOI: 10.1103/physrevlett.19.1264. 6

[23] N. F. V. Svartholm, *Abdus Salam - Weak and Electromagnetic Interactions. Published in Elementary Particle Theory: Proceedings of the 8th Nobel Symposium*. Almqvist Wiksell, 1968. 6

[24] C. Y. Prescott, "Parity Violation in Inelastic Scattering of Polarized Electrons," *AIP Conference Proceedings*, vol. 51, no. 1, pp. 202–216, May 1979. DOI: 10.1063/1.31766. 8

[25] K. S. Kumar, "The E158 Experiment," *The European Physical Journal A / Hadrons and Nuclei*, vol. 32, pp. 531–532, 4 2007, ISSN: 1434-6001,1434-601X. DOI: 10.1140/epja/i2006-10429-5. [Online]. Available: http://doi.org/10.1140/epja%2Fi2006-10429-5. 8

[26] C. E. Bennett S. C.; Wieman, "Transition Polarizability in Atomic Cesium and an Improved Test of the Standard Model," *Physical Review Letters*, vol. 82, pp. 2484–2487, 12 1999, ISSN: 0031-9007,1079-7114. DOI: 10.1103/PhysRevLett.82.2484. [Online]. Available: http://doi.org/10.1103/PhysRevLett.82.2484. 8

[27] A. Khukhunaishvili, "Measurement of the Effective Leptonic Electroweak Mixing Angle and Drell-Yan Forward-backward Asymmetry using pp Collisions at $\sqrt{s} = 13$ TeV," *arXiv e-prints*, arXiv:2405.11484, arXiv:2405.11484, May 2024. DOI: 10.48550/arXiv.2405.11484. arXiv: 2405.11484 [hep-ex]. 8

[28] Emanuel Derman; William J Marciano, "Parity Violating Asymmetries in Polarized Electron Scattering," *Annals of Physics 1979-sep vol. 121 iss. 1-2*, vol. 121, 1-2 Sep. 1979. DOI: 10.1016/0003-4916(79)90095-2. 8

[29] J. Benesch *et al.*, "The MOLLER Experiment: An Ultra-Precise Measurement of the Weak Mixing Angle Using Møller Scattering," *arXiv preprint*, vol. arXiv:1411.4088, no. nucl-ex, 2014, JLAB-PHY-14-1986. [Online]. Available: https://arxiv.org/abs/1411.4088. 9, 13

[30] B. Blaikie, "The Main Detector System for the MOLLER Experiment," in *2023 CAP Congress Program*, University of New Brunswick, Jun. 2023. [Online]. Available: https://indico.cern.ch/event/1191895/contributions/5321234/. 10

[31] The MOLLER Collaboration, "The MOLLER Technical Design Report," The MOLLER Collaboration, Tech. Rep. Internal Draft, Nov. 2022. 11, 12

[32] M. Collaboration, "Conceptual Design Report for the MOLLER Experiment," Thomas Jefferson National Accelerator Facility, Tech. Rep. DocDB-630, Version 6, 2019, Accessed: July 2025. [Online]. Available: https://moller-docdb.physics.sunysb.edu/cgi-bin/DocDB/public/ShowDocument?docid=630. 14, 15

[33] Augustin, Heiko, et al., "The MuPix Sensor for the Mu3e Experiment," *Nuclear Instruments and Methods in Physics Research Section A: Accelerators, Spectrometers, Detectors and Associated Equipment*, vol. 979, p. 164 441, 2020, ISSN: 0168-9002. DOI: 10.1016/j.nima.2020.164441. [Online]. Available: http://doi.org/10.1016/j.nima.2020.164441. 15

[34] N. N. Shefali, M. Laheji, K. Isaak, and M. Gericke, "High Voltage Monolithic Active Pixel Sensors for the MOLLER Experiment," *Nuclear Instruments and Methods in Physics Research Section A: Accelerators, Spectrometers, Detectors and Associated Equipment*, vol. 1069, p. 169 874, 2024, ISSN: 0168-9002. DOI: 10.1016/j.nima.2024.169874. 16

[35] N. N. Shefali, M. Laheji, K. Isaak, and M. Gericke, *Cooling Analyses of HV-MAPS Detector in Compton Polarimeter*, https://inspirehep.net/literature/2940575, Accessed via InSPIRE-HEP, 2024. 16

[36] Nafis R. Niloy, "Detector Development for the MOLLER Experiment," M.S. thesis, The University of Manitoba, Winnipeg, Manitoba, 2023. 16

[37] R. L. Workman *et al.*, "Review of Particle Physics: Chapter 34 Passage of Particles Through Matter," *PTEP*, vol. 2022, p. 083C01, 2022. DOI: 10.1093/ptep/ptac097. 18, 19, 40

[38] W. R. Leo, *Techniques for Nuclear and Particle Physics Experiments: A How-to Approach*, 2nd. Springer, 1994, ISBN: 3540572805,9783540572800. 18, 25, 26, 29

[39] B. W. A. Westphal, "Energy Loss of Relativistic Heavy Ions in Matter," *Nuclear Instruments and Methods in Physics Research Section B: Beam Interactions with Materials and Atoms*, vol. 187, pp. 285–301, 3 2002, ISSN: 0168-583X. DOI: 10.1016/s0168-583x(01)01143-0. [Online]. Available: http://doi.org/10.1016/s0168-583x%2801%2901143-0. 18

[40] S. N. Ahmed, *Physics and Engineering of Radiation Detection*, 2nd ed. Elsevier, 2014, ISBN: 012801363X,9780128013632. 20

[41] F. Sauli, *Gaseous Radiation Detectors: Fundamentals and Applications (Cambridge Monographs on Particle Physics, Nuclear Physics and Cosmology, Series Number 36)*. Cambridge University Press, ISBN: 9781009291187. 22–24, 26, 45, 62

[42] S. Masciocchi, *Gaseous detectors – 1*, Lecture notes, Physikalisches Institut, Universität Heidelberg and GSI Darmstadt, Summer Semester 2017, retrieved from https://www.physi.uni-heidelberg.de/~sma/teaching/ParticleDetectors/GasDetectors_1.pdf, 2017. 22

[43] S. Tavernier, *Experimental Techniques in Nuclear and Particle Physics*. Springer, 2010, ISBN: 3642008283,9783642008283. 25

[44] F. Sauli, "The Gas Electron Multiplier (GEM): Operating Principles and Applications," *Nuclear Instruments and Methods in Physics Research Section A: Accelerators, Spectrometers, Detectors and Associated Equipment*, S0168900215008980, 2015, ISSN: 0168-9002. DOI: 10.1016/j.nima.2015.07.060. 27, 28

[45] G. D. D. Group, *Gaseous Electron Multiplier*, Jun. 2024. [Online]. Available: https://gdd.web.cern.ch/gem. 27

[46] B. S. Claus Grupen, *Particle Detectors, 2nd edition (Cambridge Monographs on Particle Physics, Nuclear Physics and Cosmology)*, 2nd ed. 2008, ISBN: 0521840066. 29

[47] TTA Techtra, *GEM Foils – Gas Electron Multipliers*, https://techtra.pl/technology/gem-foils/, Accessed: 2025-08-01. 31, 32, 36, 39

[48] F. Wang, B. Nachman, and M. Garcia-Sciveres, "Ultimate Position Resolution of Pixel Clusters with Binary Readout for Particle Tracking," *Nuclear instruments methods in physics research. Section A, Accelerators, spectrometers, detectors and associated equipment*, vol. 899, no. C, pp. 10–15, 2018, ISSN: 0168-9002. 32

[49] A. Pellecchia, P. Verwilligen, and A. Stamerra, "Performance of triple-GEM Detectors for the CMS Phase-2 Upgrade Measured in Test Beam," *Nuclear instruments methods in physics research. Section A, Accelerators, spectrometers, detectors and associated equipment*, vol. 1046, pp. 167 618–, 2023, ISSN: 0168-9002. 32

[50] P. E. Karchin, "Performance of a Large-Area Triple-GEM Detector in a Particle Beam," CERN, Tech. Rep. CMS-CR-2011-233, 2011. [Online]. Available: https://cds.cern.ch/record/1395458/files/CR2011_233.pdf. 32

[51] TTA Techtra, "High Voltage Divider for 10×10 cm GEM Detector V2.1," Techtra, Technical Report Rev. 1, 2016. [Online]. Available: https://techtra.pl/wp-content/uploads/High_Voltage_Divider.pdf. 32

[52] R. N. Patra, R. N. Singaraju, S. Biswas, Z. Ahammed, T. K. Nayak, and Y. P. Viyogi, "Measurement of Basic Characteristics and Gain Uniformity of a Triple GEM Detector," *Nuclear Instruments and Methods in Physics Research Section A: Accelerators, Spectrometers, Detectors and Associated Equipment*, vol. 862, pp. 25–30, 2017, ISSN: 0168-9002. DOI: 10.1016/j.nima.2017.05.011. 35

[53] M. Ester, H.-P. Kriegel, J. Sander, and X. Xu, "A Density-Based Algorithm for Discovering Clusters in Large Spatial Databases with Noise," in *Proceedings of the Second International Conference on Knowledge Discovery and Data Mining (KDD'96)*, AAAI Press, 1996, pp. 226–231. 49, 51

[54] J. Sander, M. Ester, H.-P. Kriegel, and X. Xu, "Density-Based Clustering in Spatial Databases: The Algorithm GDBSCAN and Its Applications," eng, *Data mining and knowledge discovery*, vol. 2, no. 2, pp. 169–194, 1998, ISSN: 1384-5810. 51

[55] E. R. Thomas K. Gaisser Ralph Engel, *Cosmic Rays and Particle Physics*, 2nd ed. Cambridge University Press, 2016, ISBN: 9780521016469; 0521016460. 54

[56] M.-M. Bé, V. Chisté, C. Dulieu, *et al.*, *Table of Radionuclides* (Monographie BIPM-5). Pavillon de Breteuil, F-92310 Sèvres, France: Bureau International des Poids et Mesures, 2016, vol. 8, ISBN: 978-92-822-2264-5. [Online]. Available: http://www.bipm.org/utils/common/pdf/monographieRI/Monographie_BIPM-5_Tables_Vol8.pdf. 58

[57] W. Guo, M. Dufault, S. B. Cahn, J. A. Nikkel, Y. Shin, and D. N. McKinsey, "Scintillation and Charge Yield from the Tracks of Energetic Electrons in Superfluid Helium-4," *Journal of Instrumentation*, vol. 7, P01002, 1 2012, ISSN: 1748-0221. [Online]. Available: https://doi.org/10.1088/1748-0221/7/01/P01002. 58

Appendix A

Setup of the Data Acquisition

A.0.1 Readout Board

Each of the triple-GEM readout boards requires both analog and digital power supplies (see Figure A.1 and Appendix B). The analog power input is labeled **J7-II** in Figure A.1 and is supplied by a *KORAD KA3305P* — Programmable DC Power Supply (30 V, 5 A $\times$ 2; 5 V, 3 A $\times$ 1) (not shown in the figures).

The digital power input is labeled **J8-II**. A 5 V input is provided to the board, which is internally regulated down to 3.3 V, 2.5 V, and 1.2 V using three dedicated voltage regulators to meet the requirements of the FPGA and DDC components. This digital power is supplied by a *KEYSIGHT E3631A* — Triple Output DC Power Supply (0–6 V, 5 A / $\pm$25 V, 1 A) (also not shown in the figures).

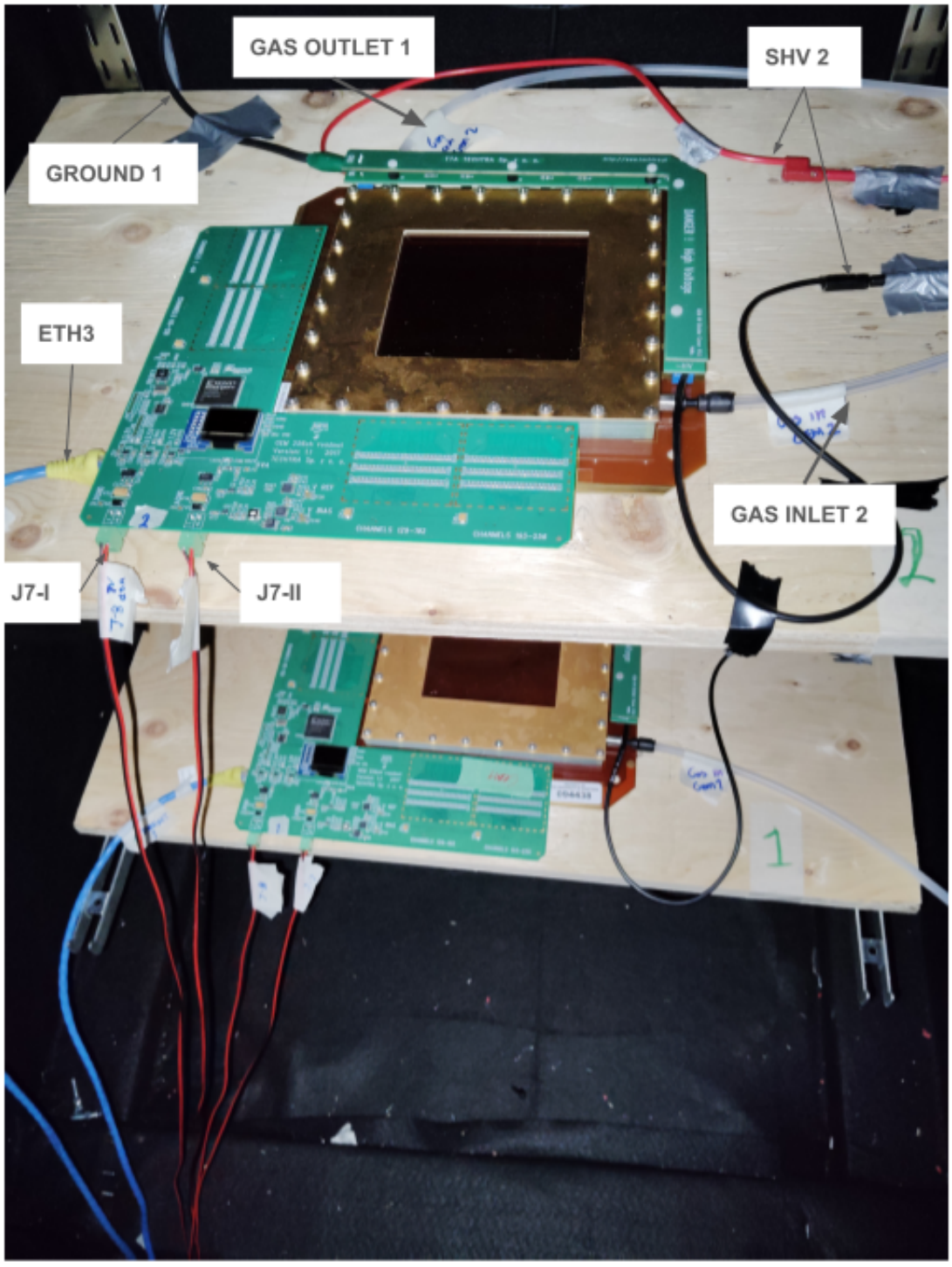

Figure A.1: Schematic diagram showing the peripheral components of the GEM stand. Only the peripherals associated with the top triple-GEM detector are labeled; the bottom triple-GEM is omitted for clarity, but follows a similar configuration.

A.0.2 Techtra® DDC software

The data acquisition is performed using the Techtra® DDC software, which establishes a connection with the triple-GEM detectors via the readout board using the Ethernet protocol (see Figure A.2). Techtra® DDC software can only run on PCs with Microsoft® Windows® system installed.

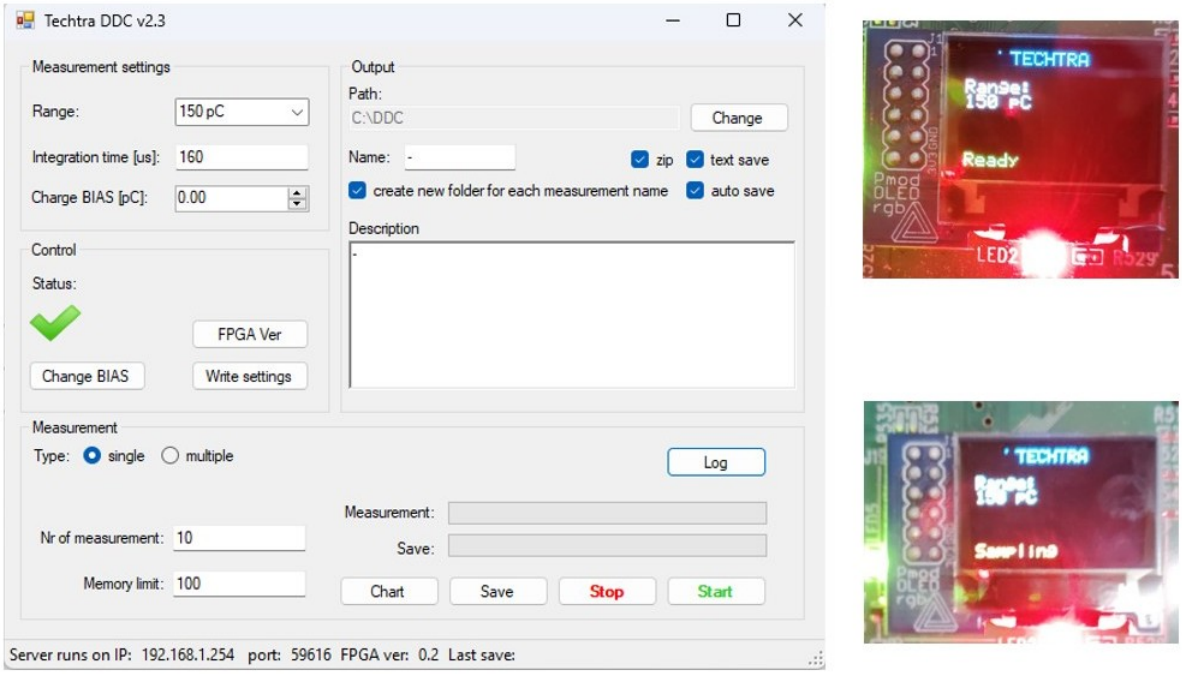

Figure A.2: *Left:* The Techtra® DDC software's main window displaying the status of a connected Ethernet communication.. *Upper right:* The LED screen indicates the "ready" status (the triple-GEM is ready to take data). *Lower right:* The LED screen indicates the "sampling" status (the triple-GEM is sending out data to PC).

Within the Techtra® DDC software installation folder, the file `config.ini` requires to set each triple-GEM with the values described in Table A.1. A set of LEDs on the readout board, helps to indicate the operational state of the board either the connection has been successful or not (see figure A.3).

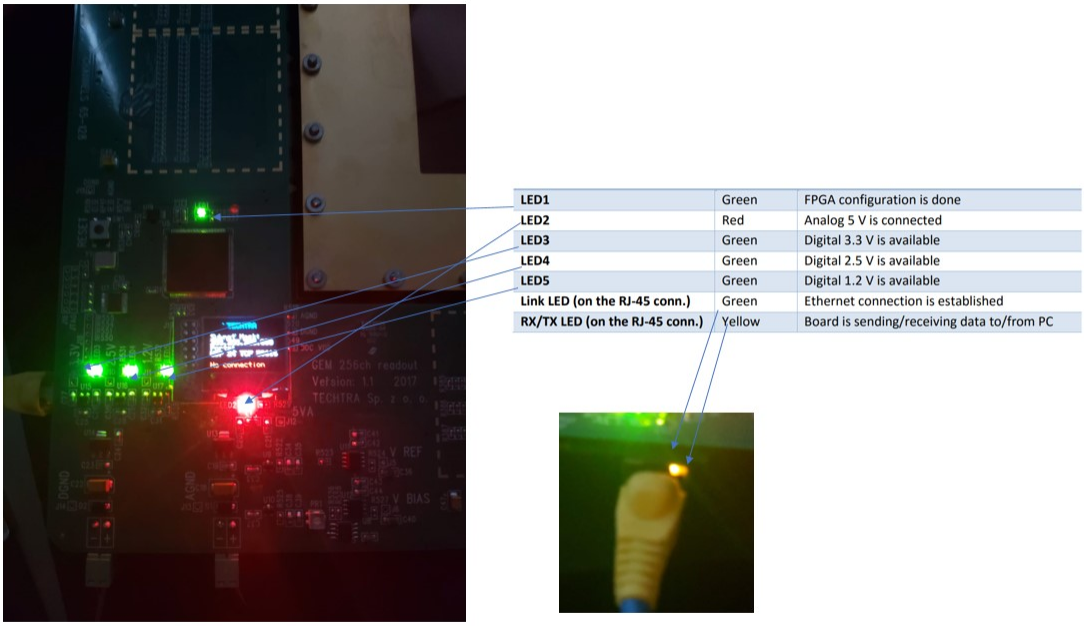

LED1	Green	FPGA configuration is done
LED2	Red	Analog 5 V is connected
LED3	Green	Digital 3.3 V is available
LED4	Green	Digital 2.5 V is available
LED5	Green	Digital 1.2 V is available
Link LED (on the RJ-45 conn.)	Green	Ethernet connection is established
RX/TX LED (on the RJ-45 conn.)	Yellow	Board is sending/receiving data to/from PC

Figure A.3: The LED indicators on the readout board helps to monitor the operational state of the board based on their color.

Bottom Triple-GEM	
Parameter	**Value**
container_size	512
measurement_delay	500
receive_timeout_tcp	1000
send_timeout_tcp	1000
server_tcp_ip	192.168.1.254
server_tcp_port	59615
server_udp_ip	192.168.1.254
server_udp_port	23
simulator_tcp_ip	192.168.1.254
simulator_tcp_port	12345
integration_time	160
calibrated_max_bias	4,0
calibrated_max_bias_integration_time	100,0
ddc_range	3
Top Triple-GEM	
Parameter	**Value**
container_size	512
measurement_delay	500
receive_timeout_tcp	1000
send_timeout_tcp	1000
server_tcp_ip	192.168.1.254
server_tcp_port	59616
server_udp_ip	192.168.1.254
server_udp_port	24
simulator_tcp_ip	192.168.1.254
simulator_tcp_port	12345
simulator_udp_ip	192.168.1.254
simulator_udp_port	12345
integration_time	160
calibrated_max_bias	4,0
calibrated_max_bias_integration_time	100,0
ddc_range	3

Table A.1: Ethernet configurations set to establish communication control between the GEM stand and the PC.

Appendix B

Technical Drawings of the Experiment

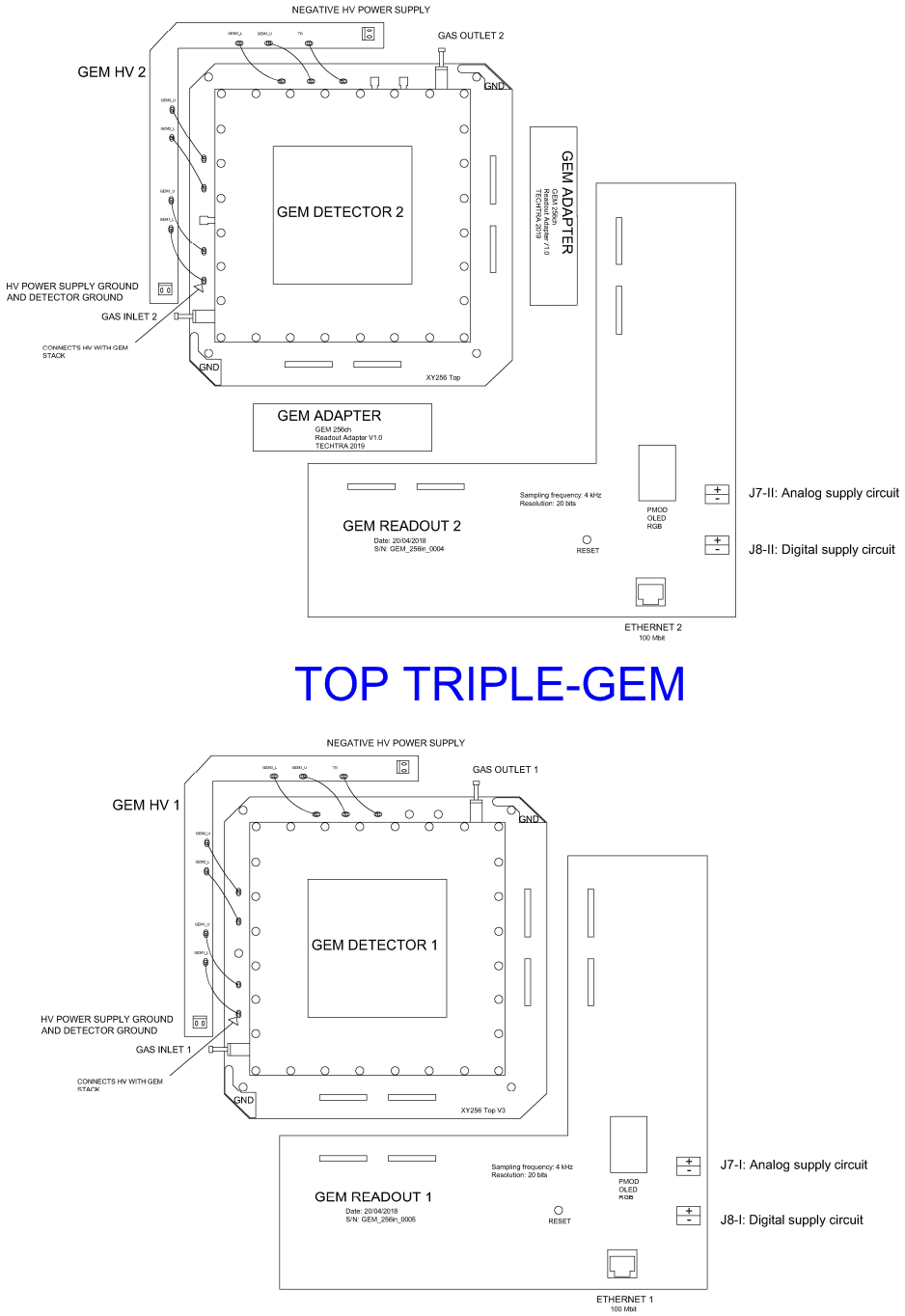

Figure B.1: Schematic representation of the main features of a triple-GEM detector, based on the standard factory design

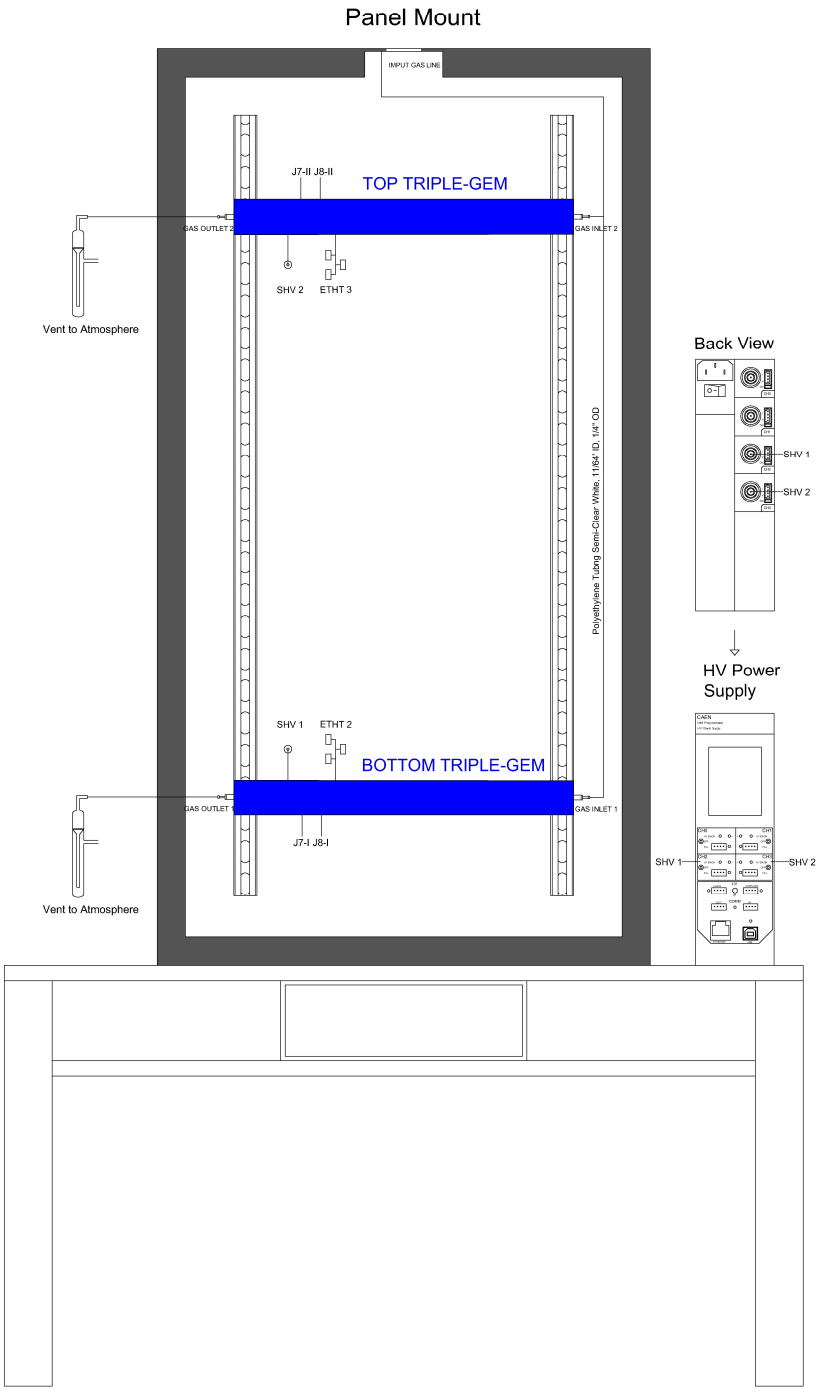

Figure B.2: Piping and Instrumentation Diagram (P&ID) of the GEM stand. This schematic highlights the primary peripheral components.

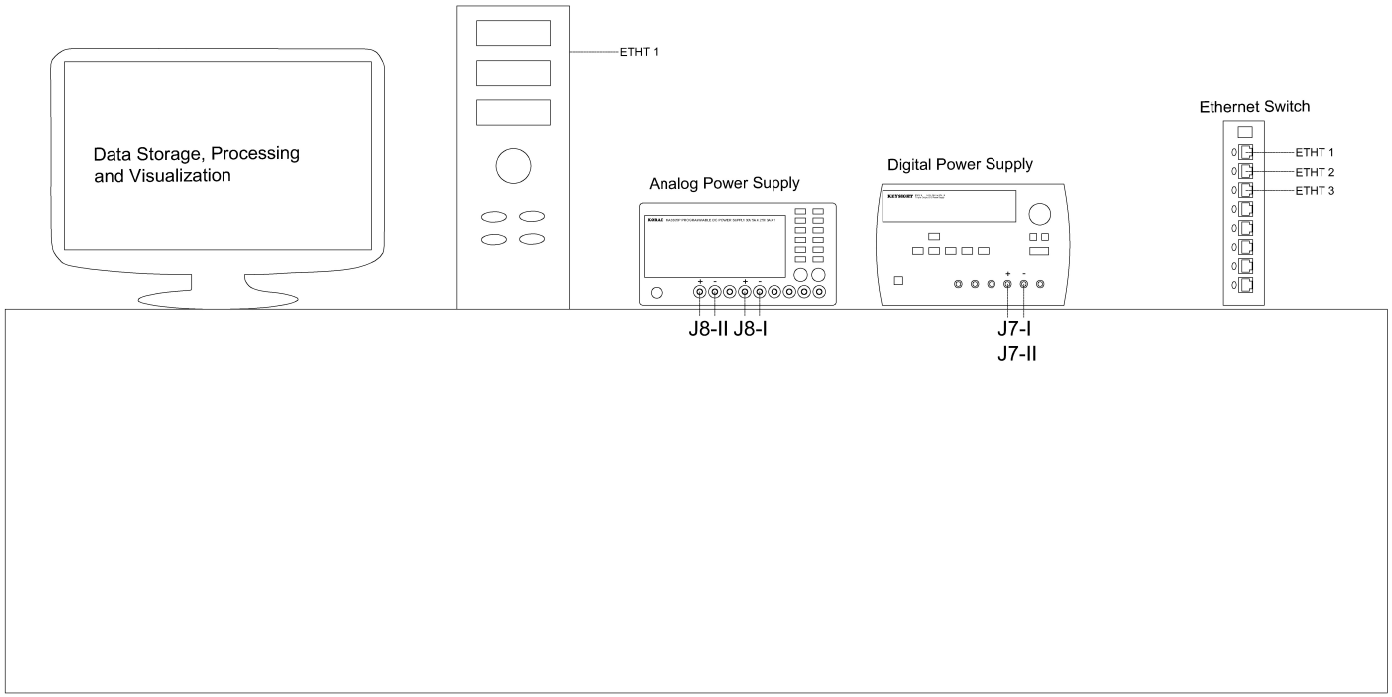

Figure B.3: Peripherals and components of the PC-based control and data acquisition system for the GEM stand.

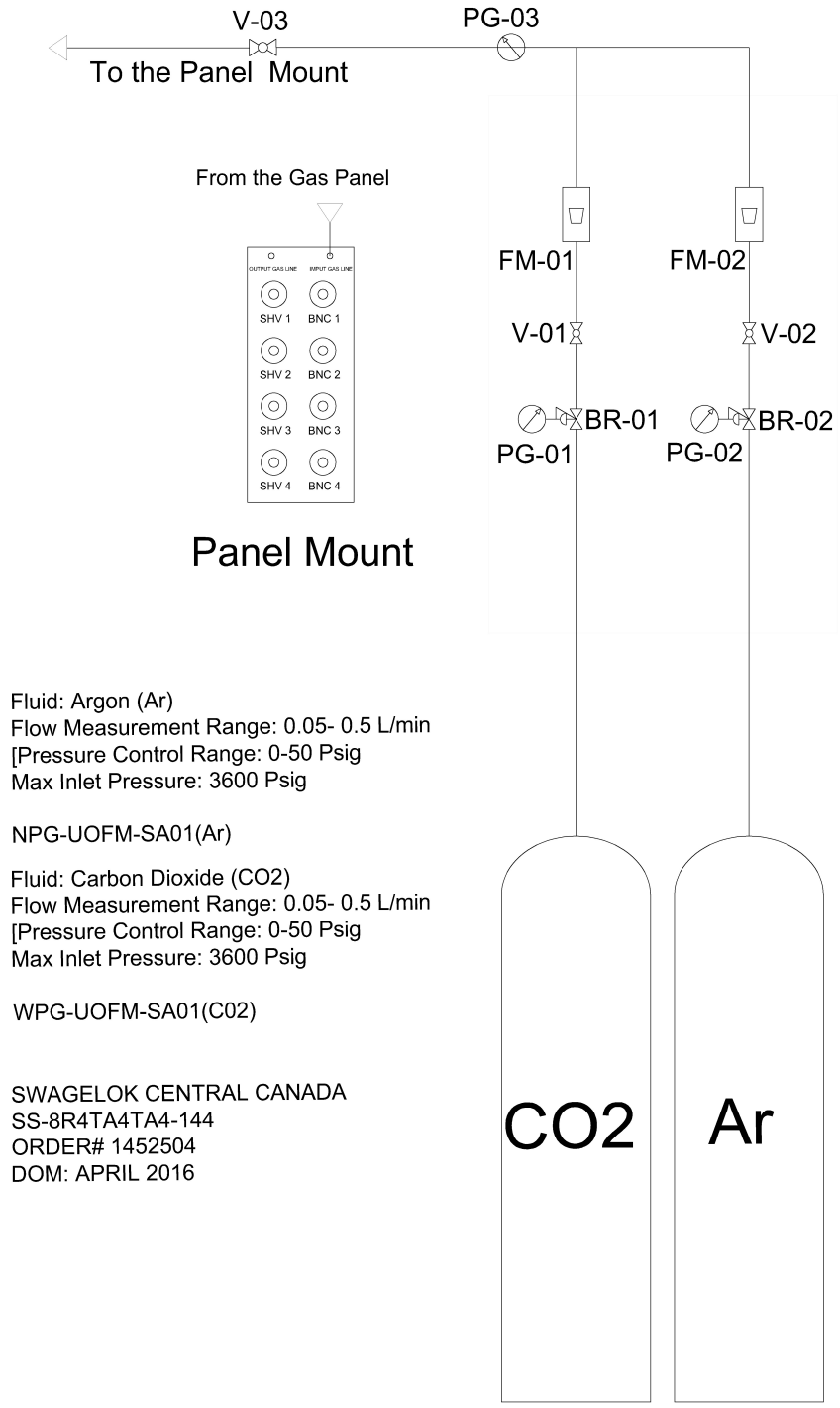

Figure B.4: Gas panel displaying the technical details of the panel mount, the gas cylinders, valves (V), pressure regulators (PR), breakaway valve (BR), and flow meters (FM).

Appendix C

Future Improvements to the Experiment

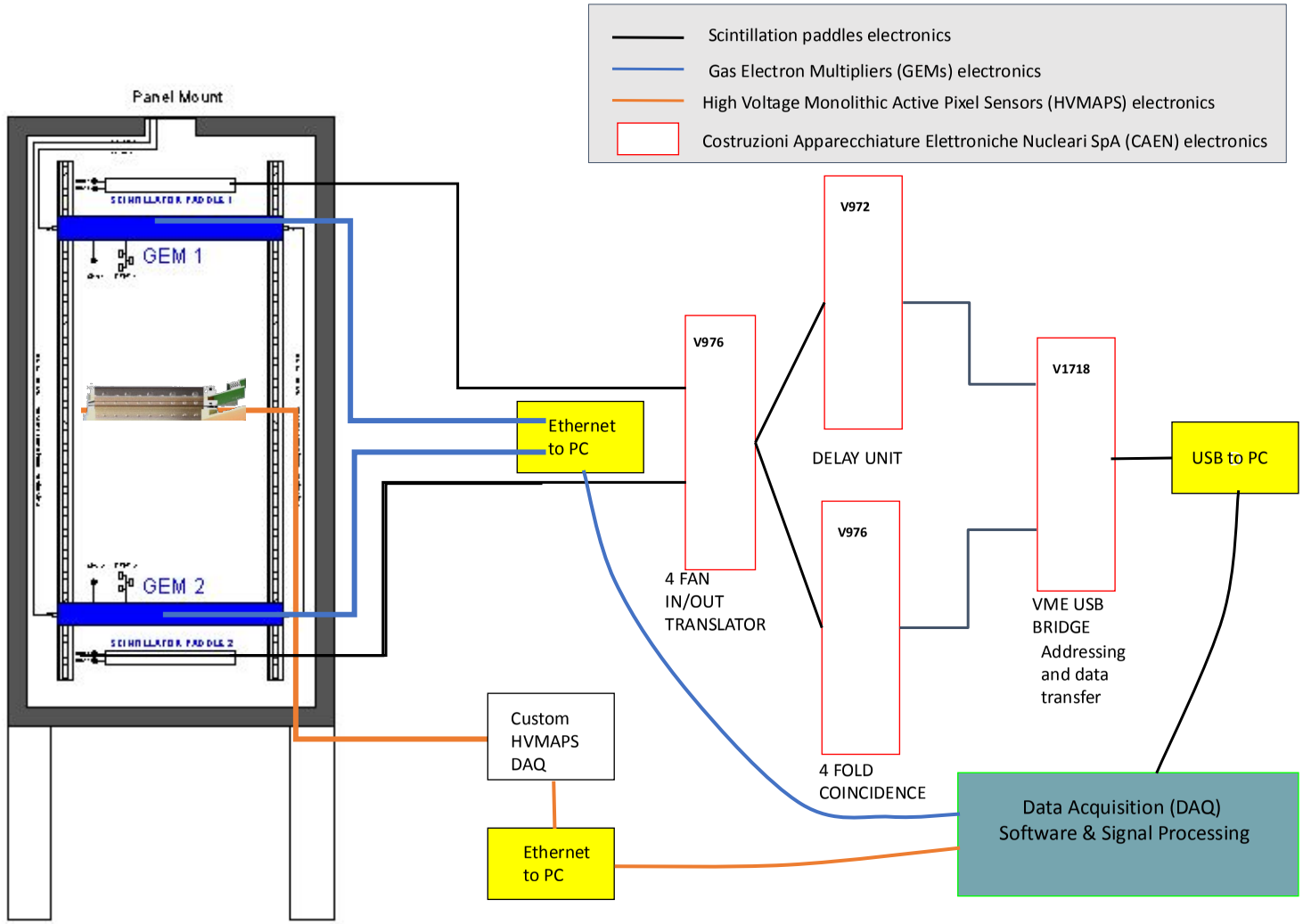

Figure C.1: This diagram presents a proposed design to upgrade the GEM stand for use as a characterization station for the spatial resolution of HV-MAPS. Implementing this functionality requires operation in coincidence mode and further development of both hardware and software.

Appendix D

Charge Collected in the GEM Stand

D.0.1 Bottom Triple-GEM (Muons)

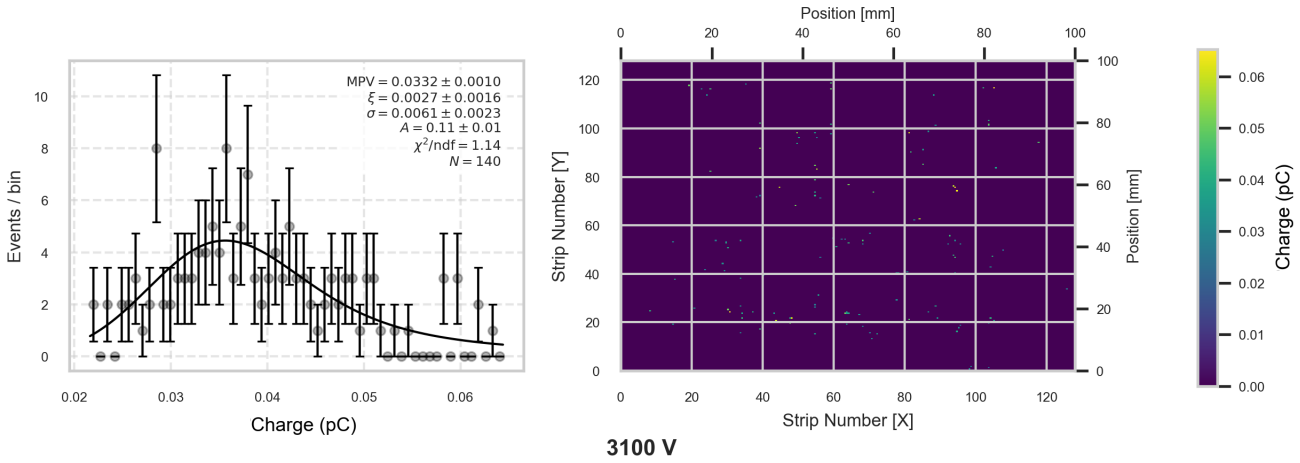

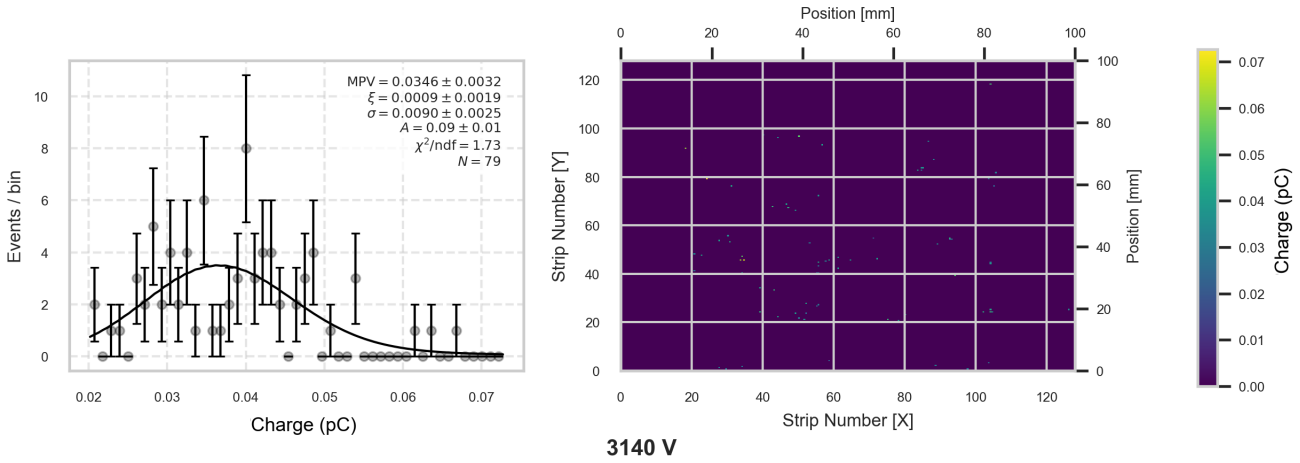

3140 V

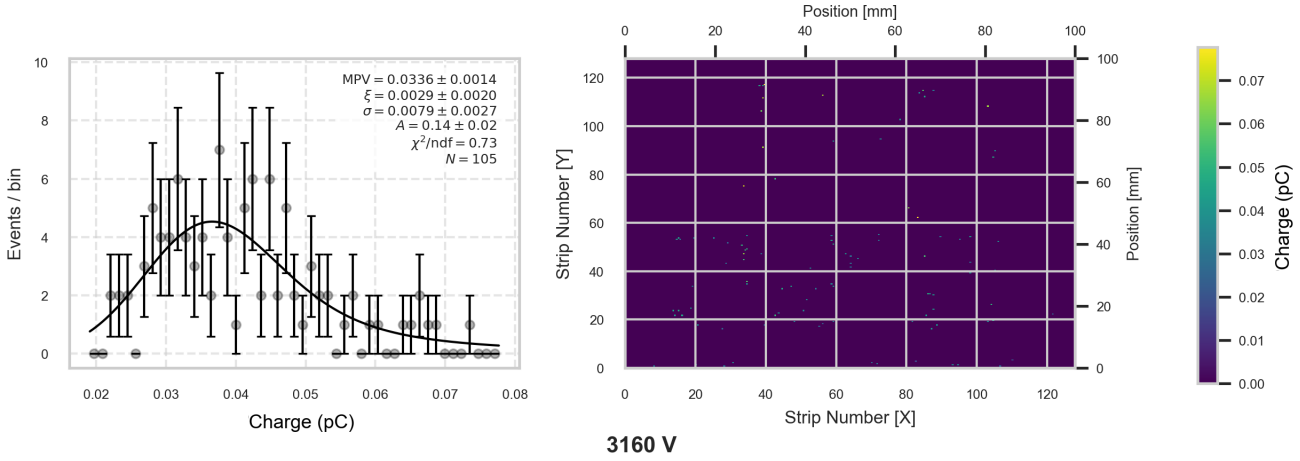

3160 V

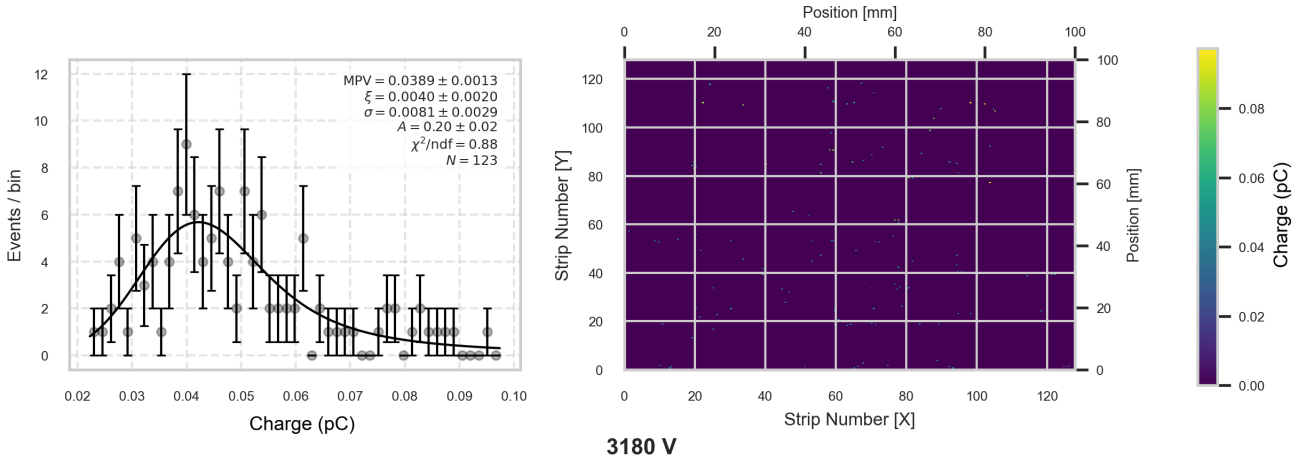

3180 V

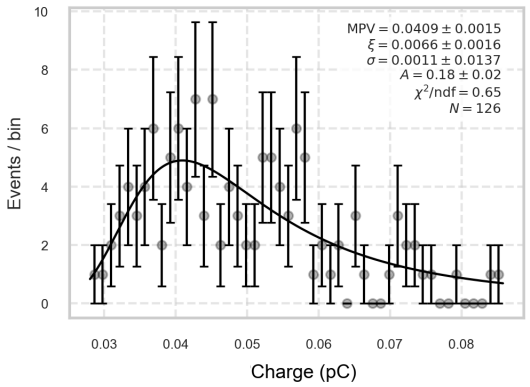

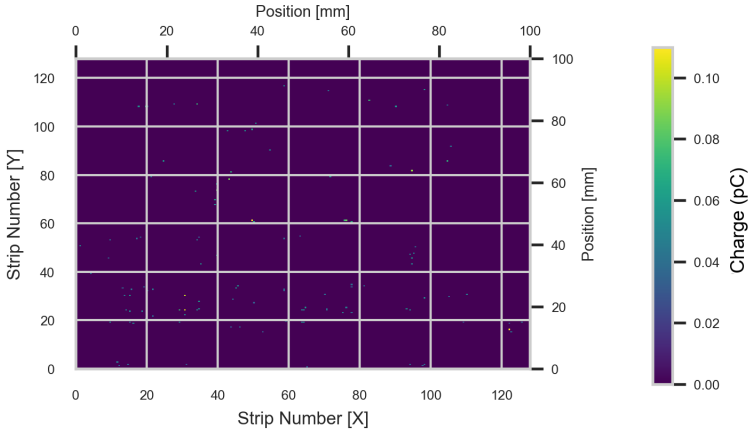

3200 V

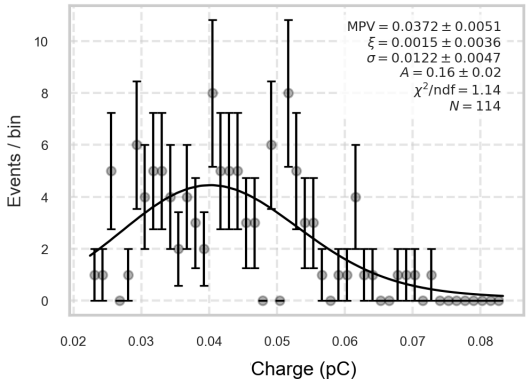

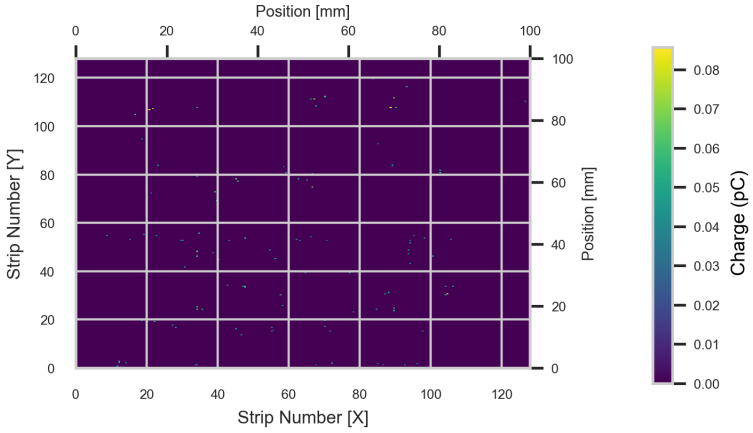

3220 V

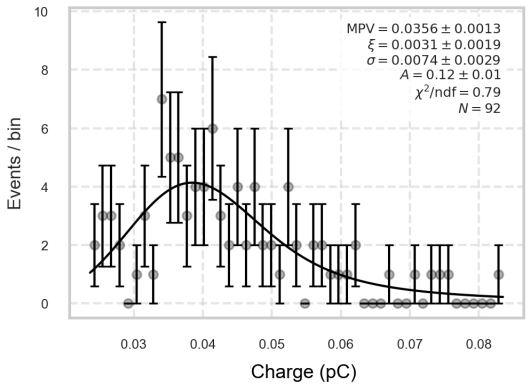

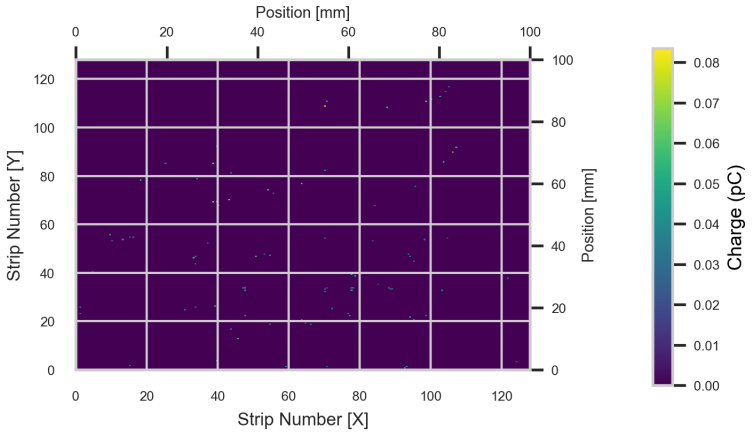

3240 V

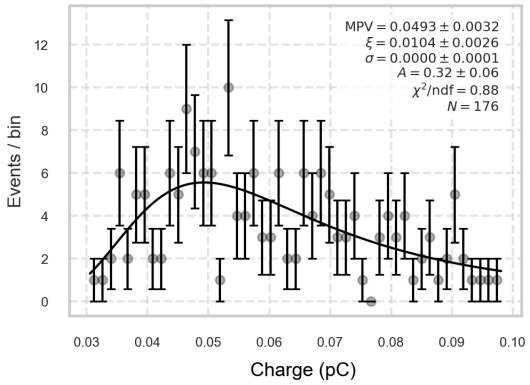

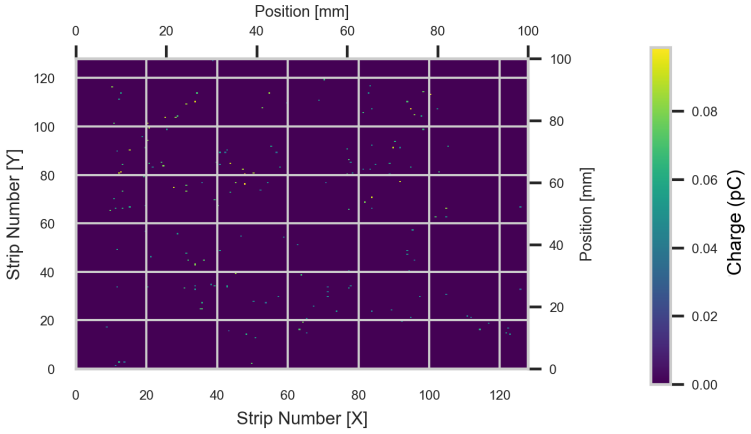

3260 V

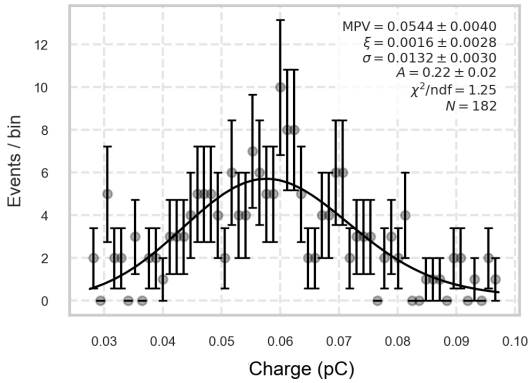

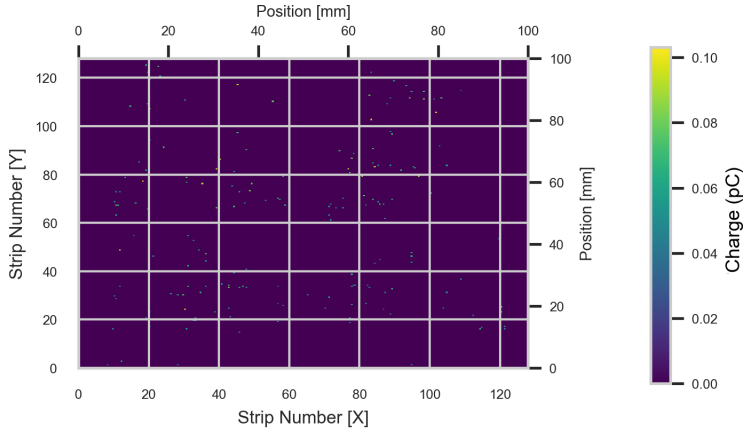

3280 V

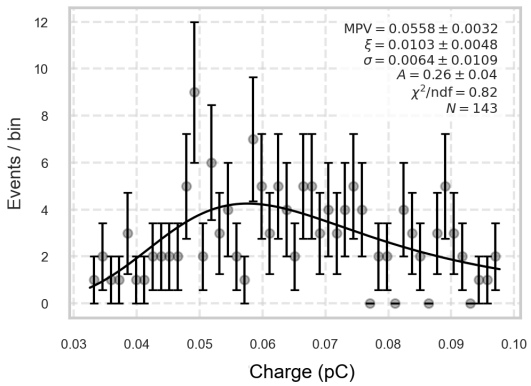

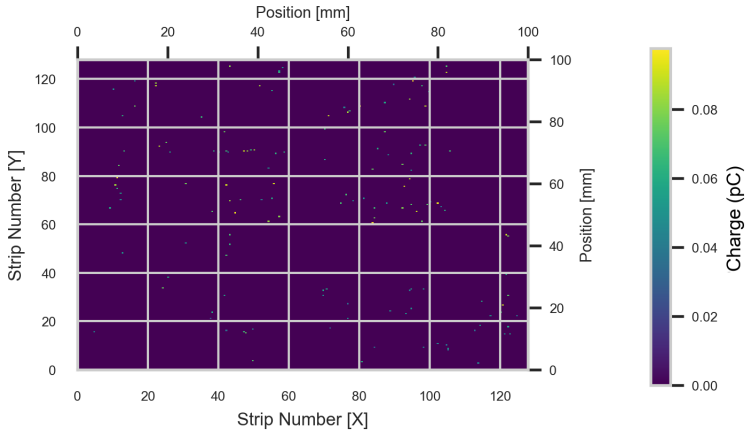

3300 V

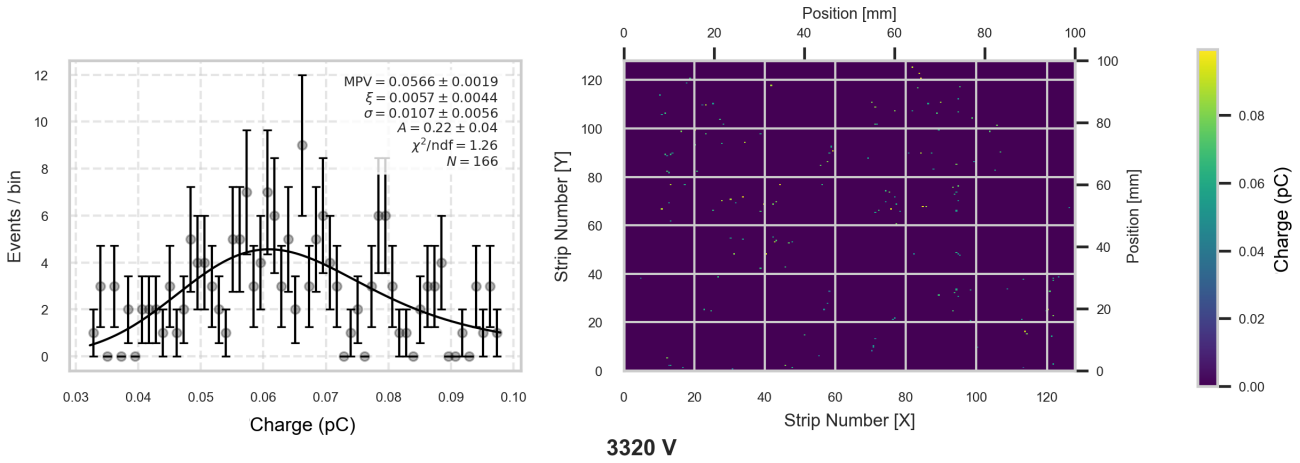
MPV = 0.0566 ± 0.0019
ξ = 0.0057 ± 0.0044
σ = 0.0107 ± 0.0056
A = 0.22 ± 0.04
χ²/ndf = 1.26
N = 166
Events / bin
Charge (pC)
Position [mm]
Strip Number [Y]
Strip Number [X]
Position [mm]
Charge (pC)

3320 V

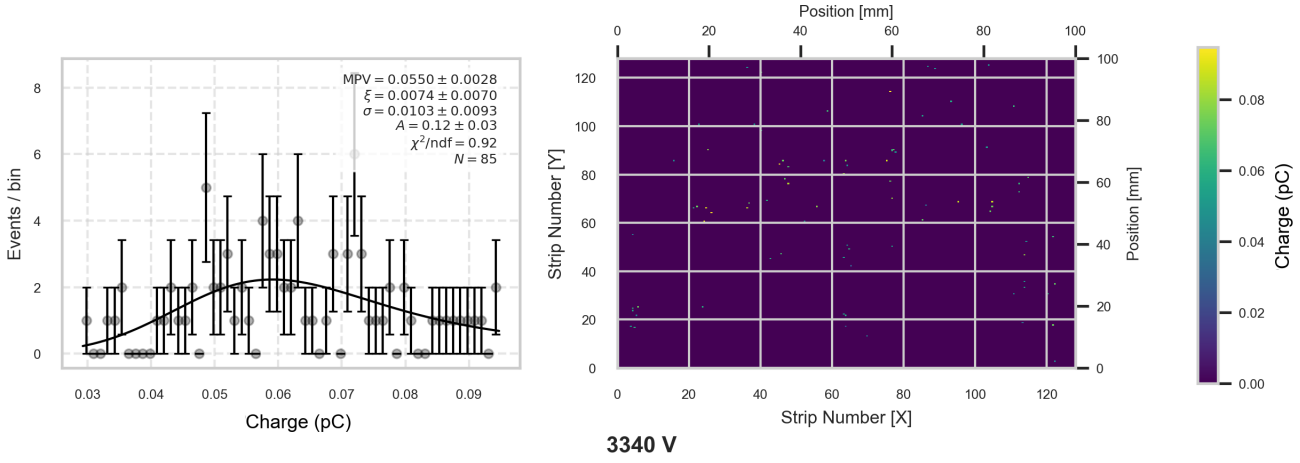
MPV = 0.0550 ± 0.0028
ξ = 0.0074 ± 0.0070
σ = 0.0103 ± 0.0093
A = 0.12 ± 0.03
χ²/ndf = 0.92
N = 85
Events / bin
Charge (pC)
Position [mm]
Strip Number [Y]
Strip Number [X]
Position [mm]
Charge (pC)

3340 V

D.0.2 Top Triple-GEM (Muons)

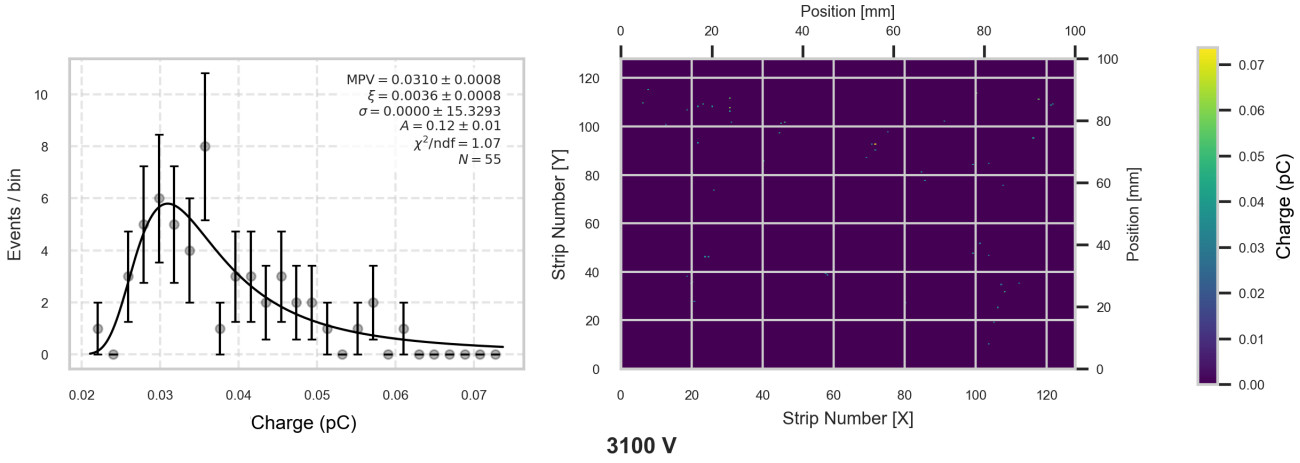

3100 V

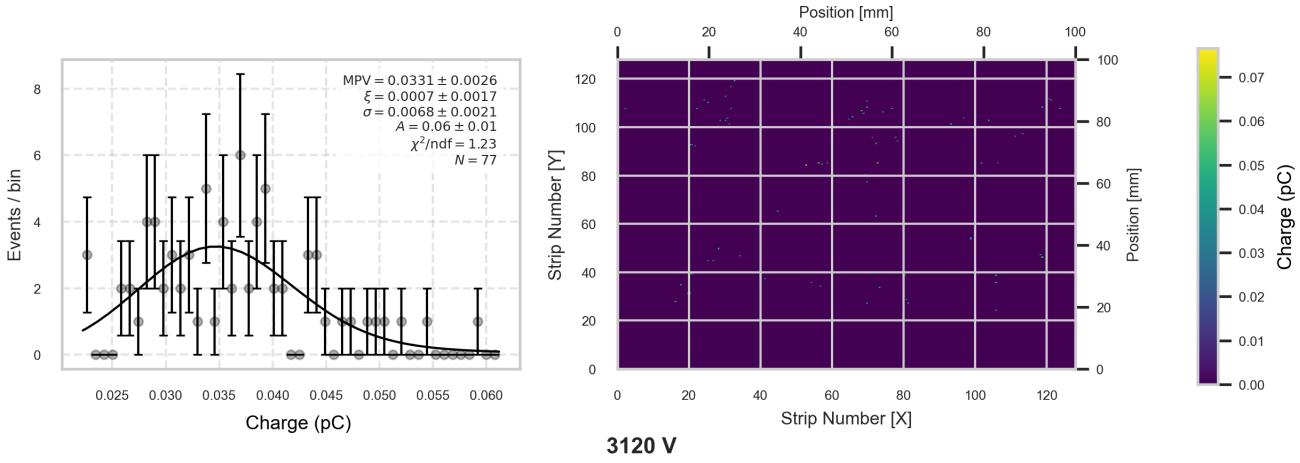

3120 V

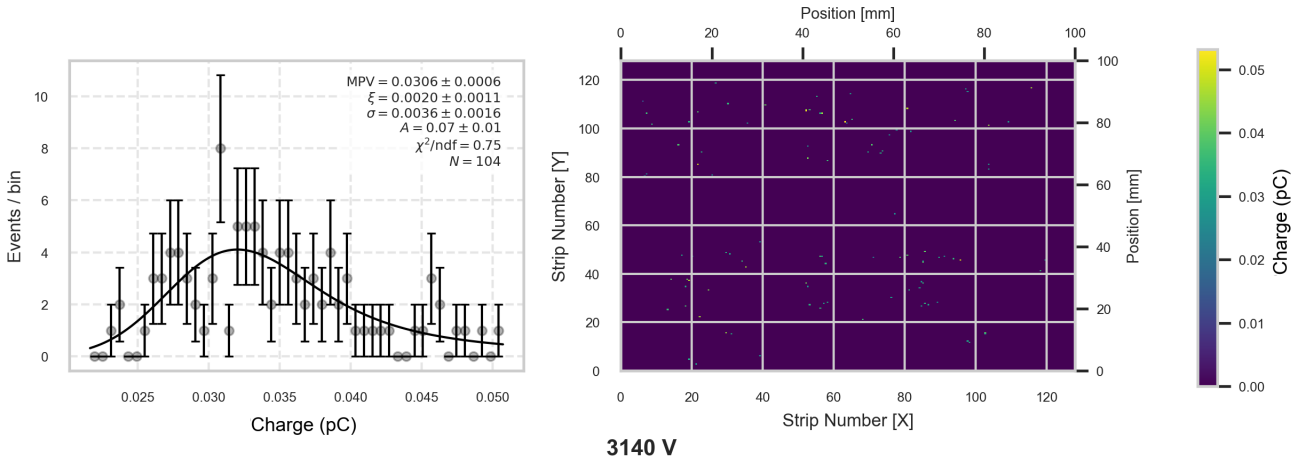

3140 V

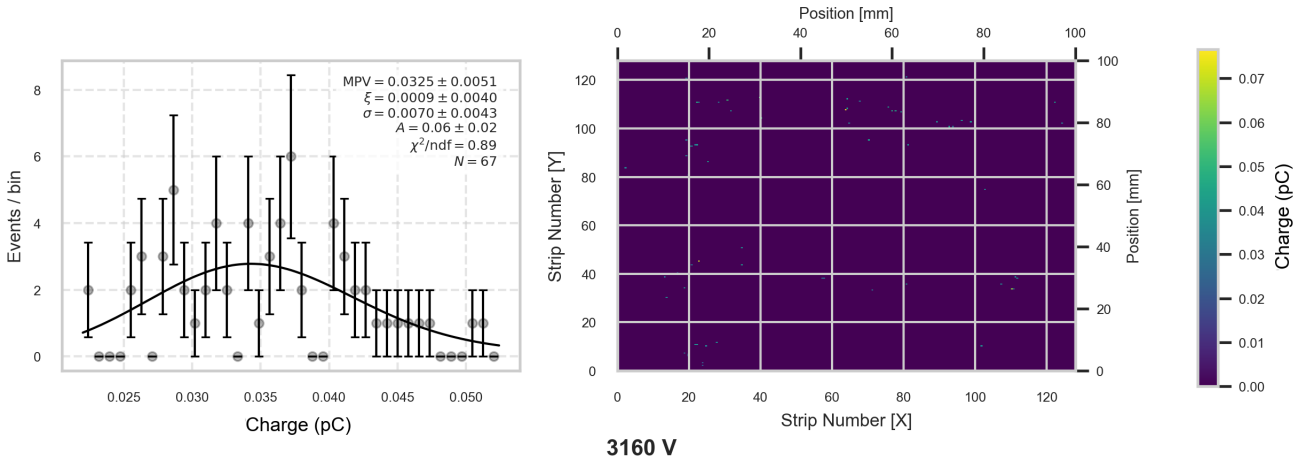

3160 V

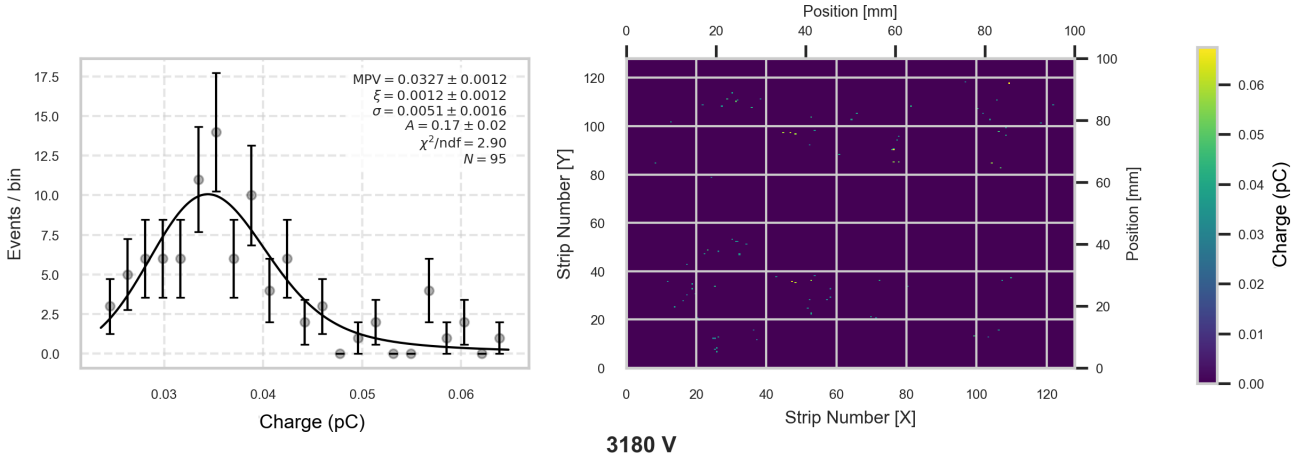

3180 V

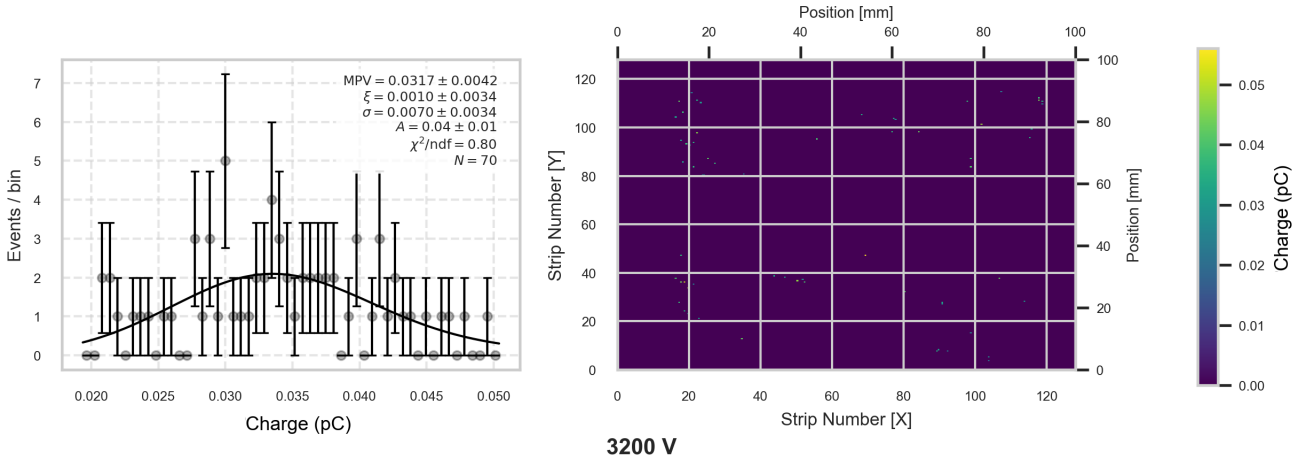

3200 V

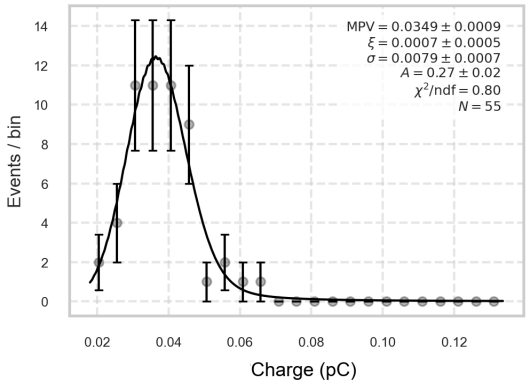

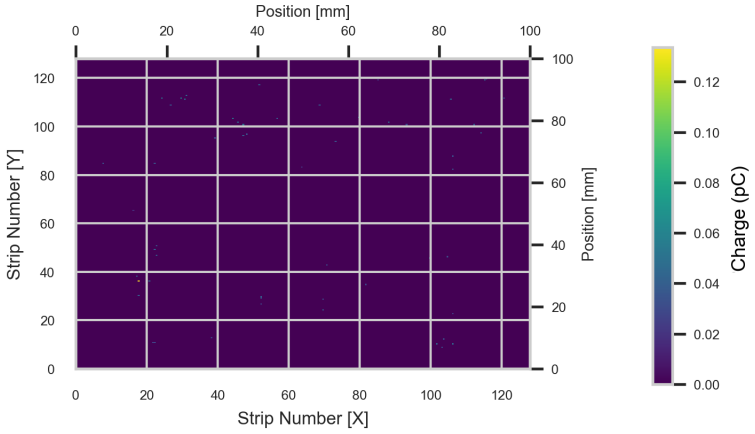

3220 V

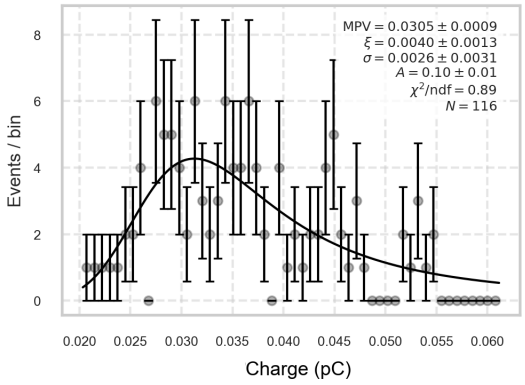

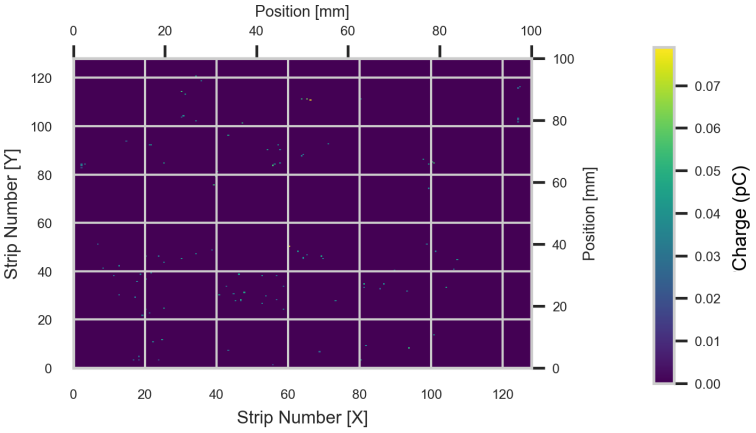

3240 V

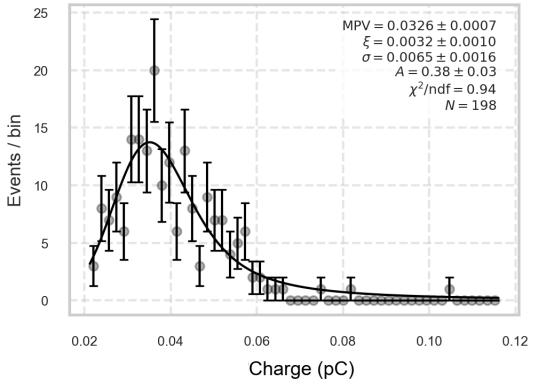

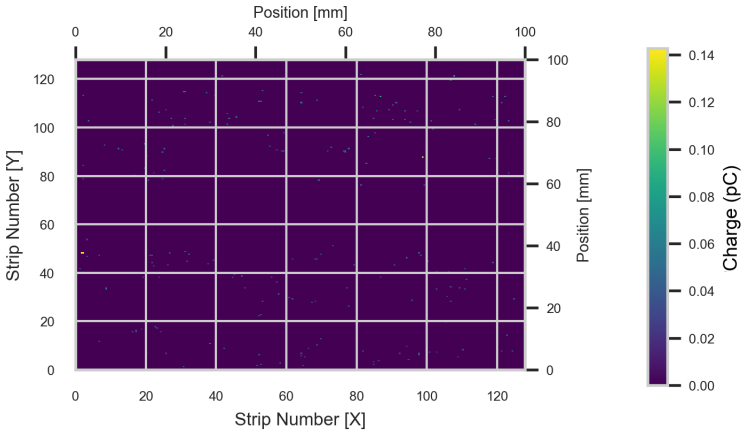

3260 V

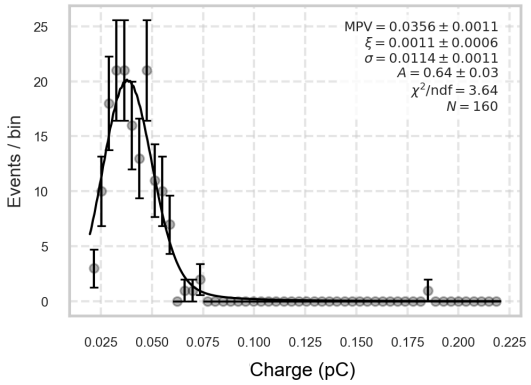
MPV = 0.0356 ± 0.0011
ξ = 0.0011 ± 0.0006
σ = 0.0114 ± 0.0011
A = 0.64 ± 0.03
χ²/ndf = 3.64
N = 160
Events / bin
Charge (pC)

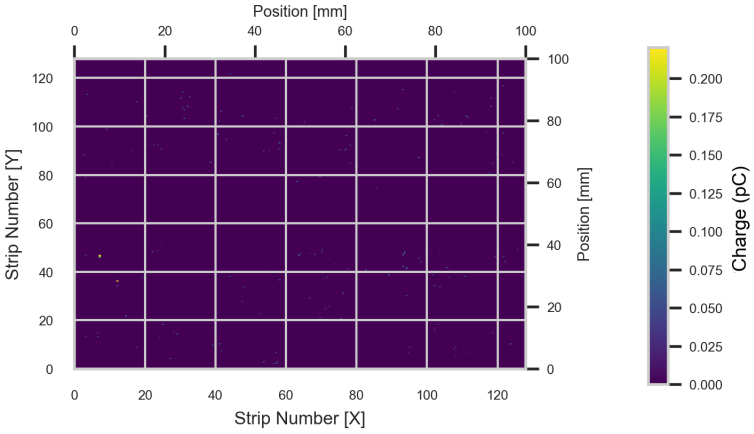
Position [mm]
Strip Number [Y]
Strip Number [X]
Position [mm]
Charge (pC)

3280 V

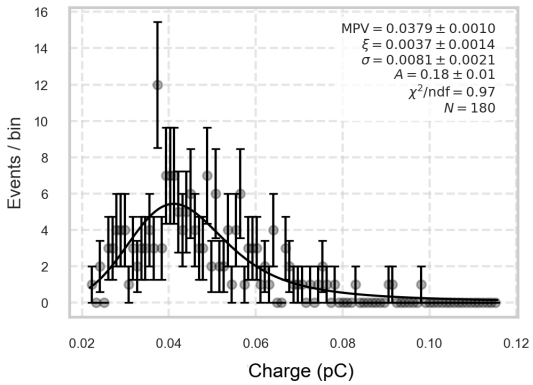
MPV = 0.0379 ± 0.0010
ξ = 0.0037 ± 0.0014
σ = 0.0081 ± 0.0021
A = 0.18 ± 0.01
χ²/ndf = 0.97
N = 180
Events / bin
Charge (pC)

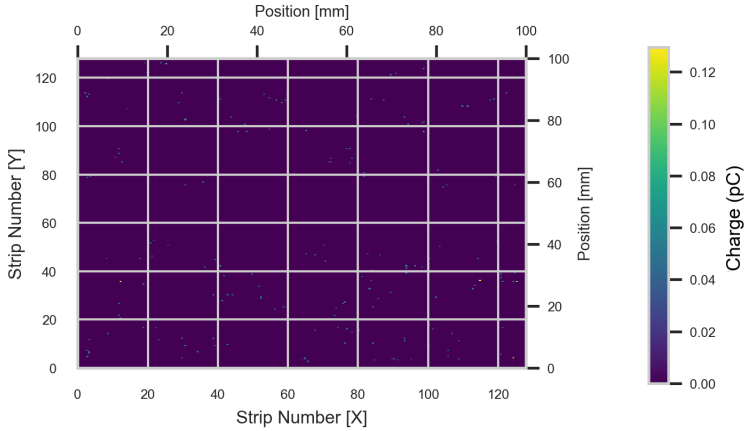
Position [mm]
Strip Number [Y]
Strip Number [X]
Position [mm]
Charge (pC)

3300 V

D.0.3 Bottom Triple-GEM (Fe-55)

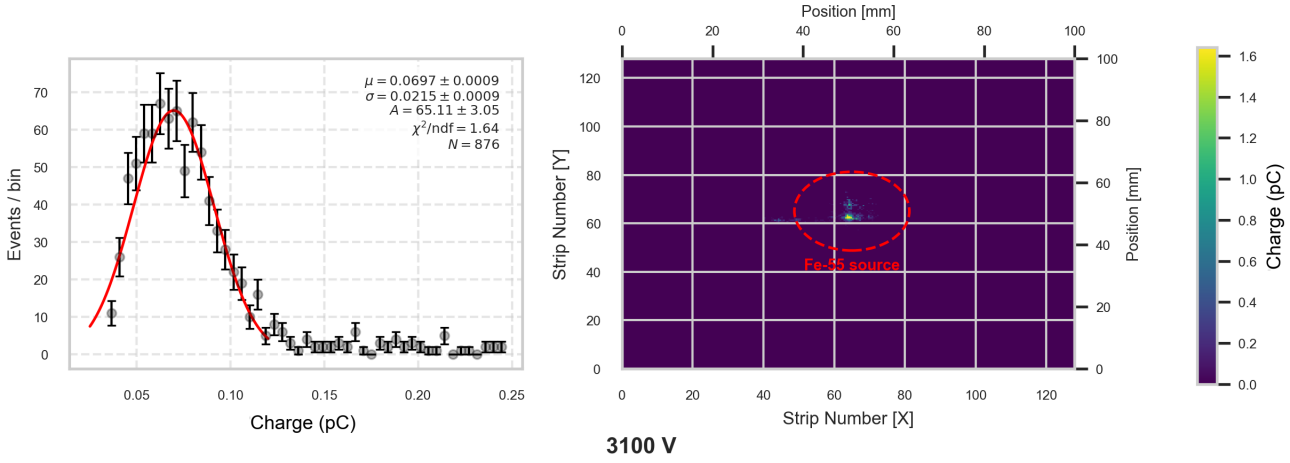

3100 V

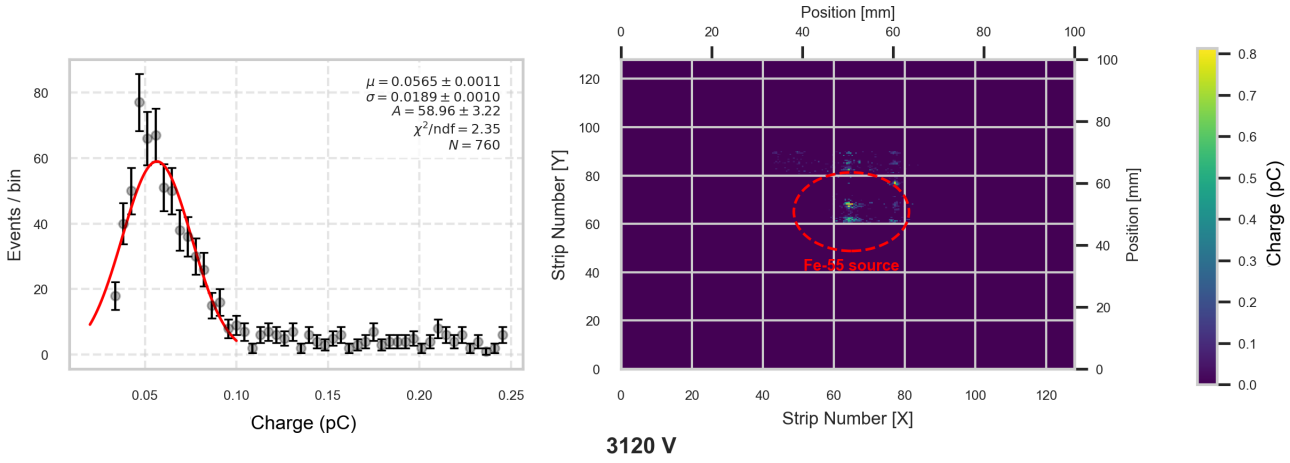

3120 V

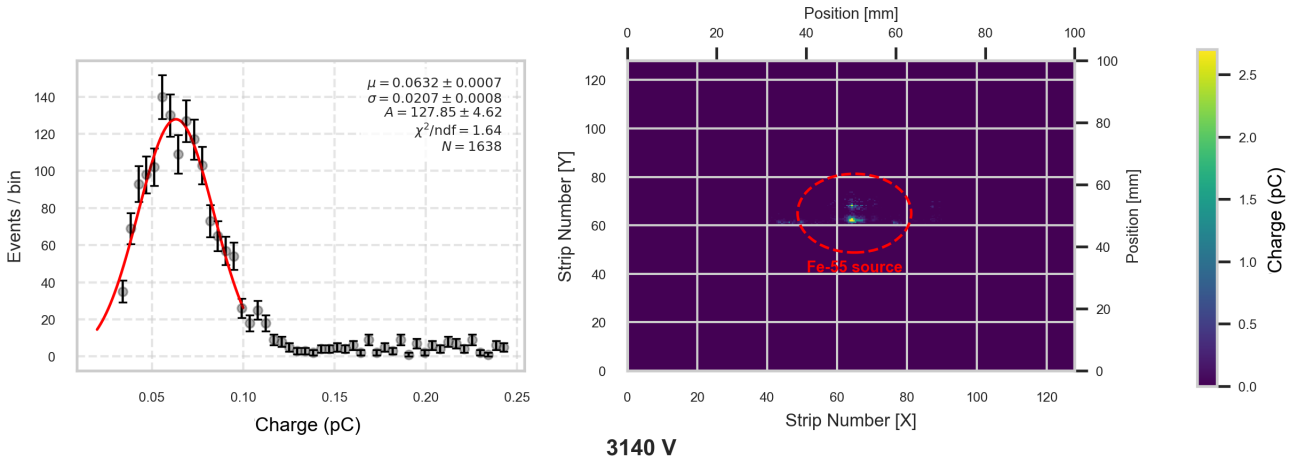

3140 V

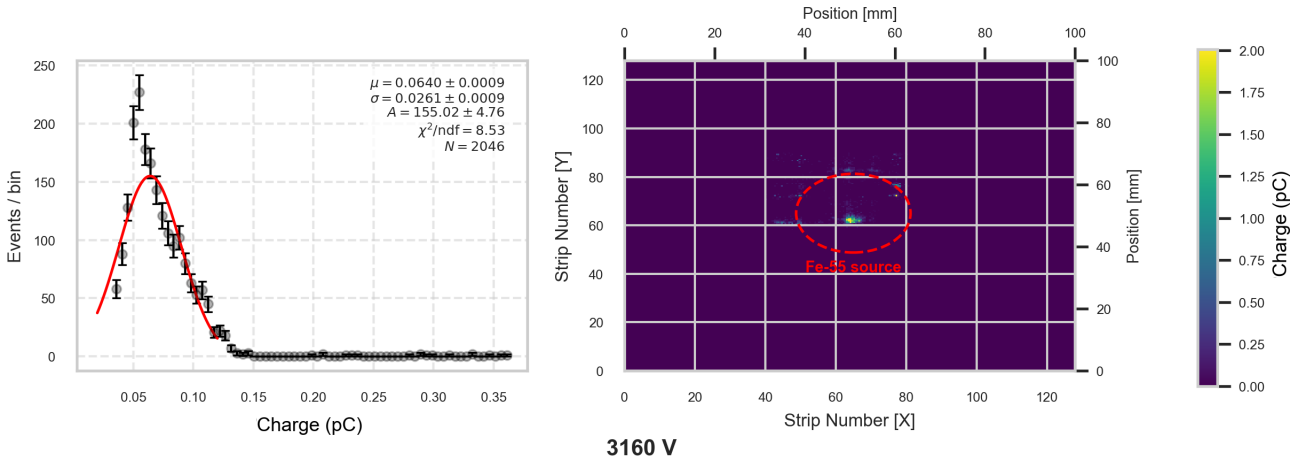

3160 V

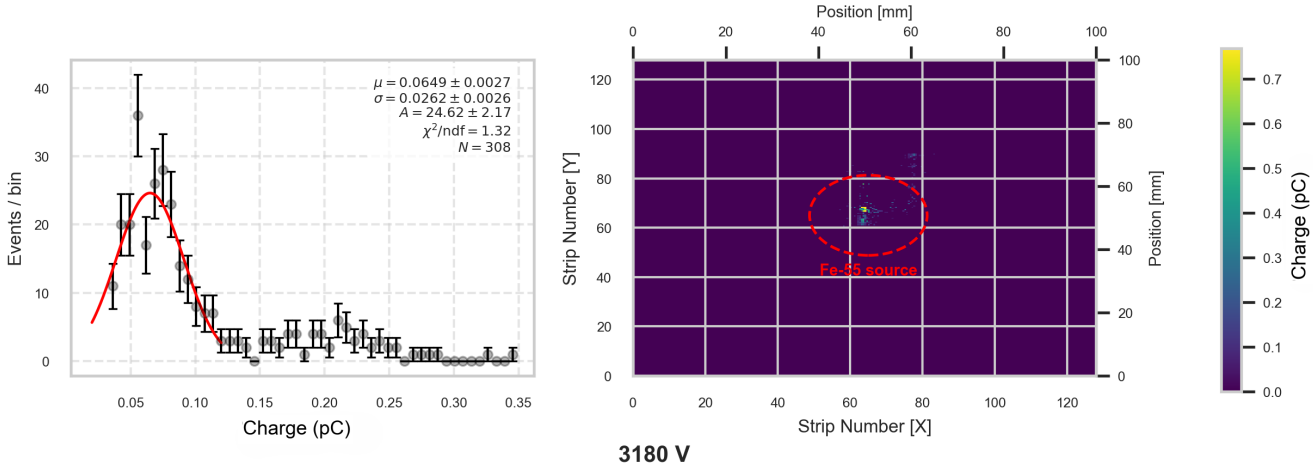

3180 V

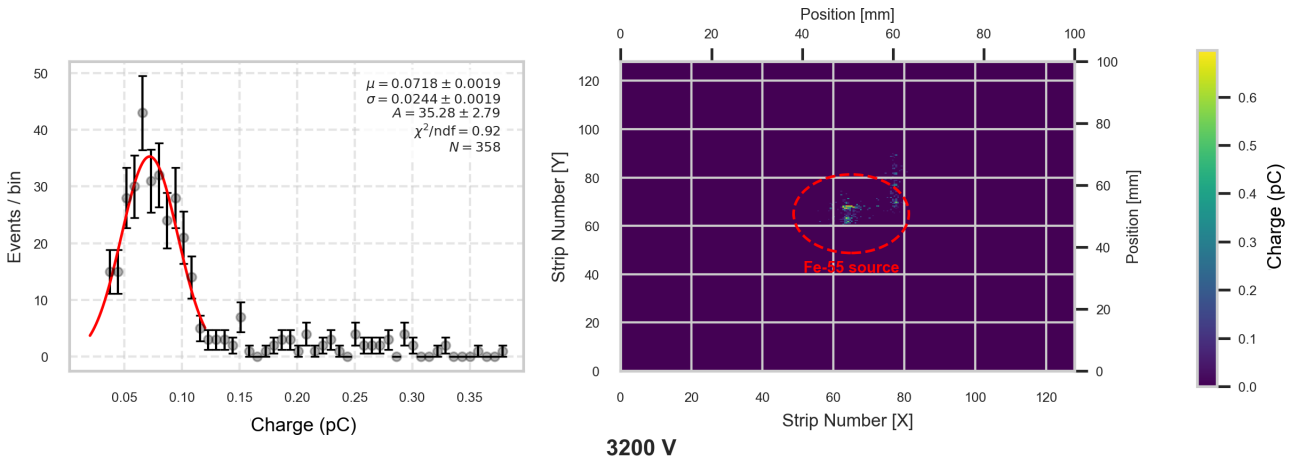

3200 V

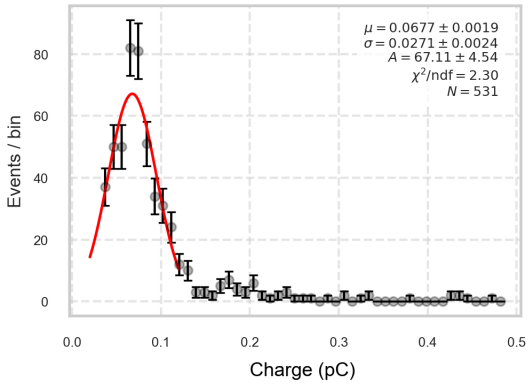

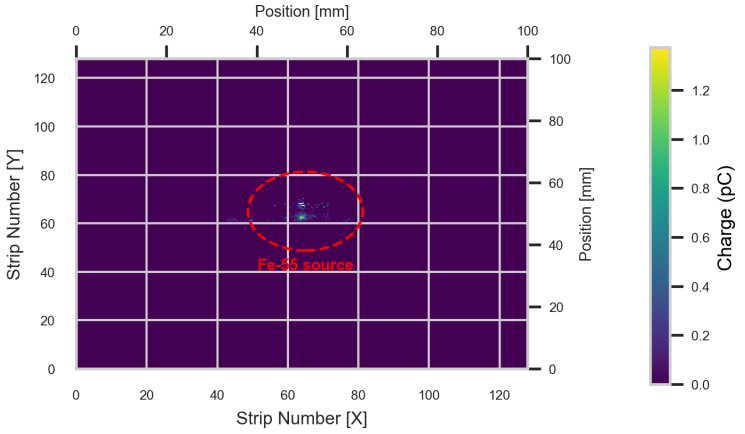

3220 V

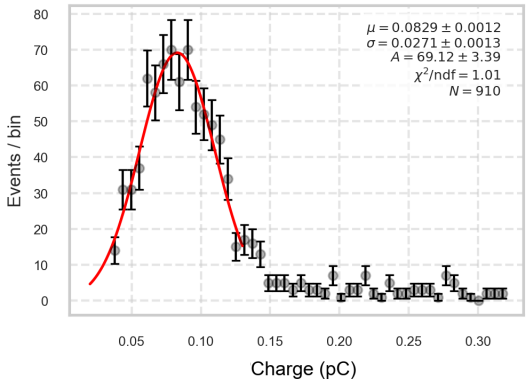

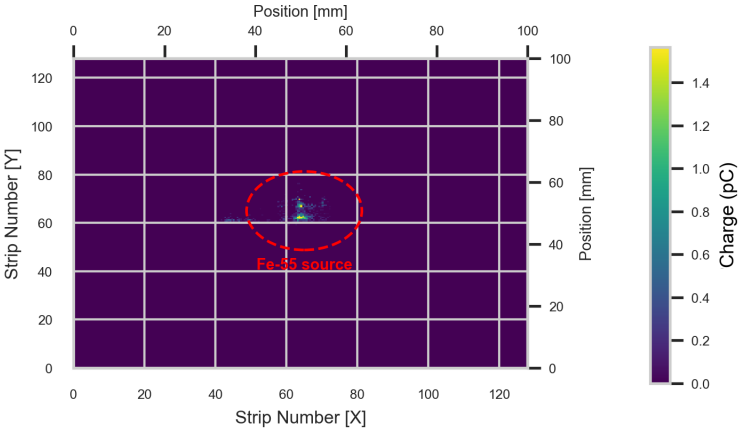

3240 V

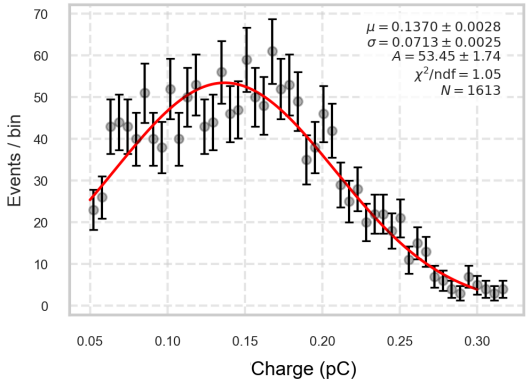

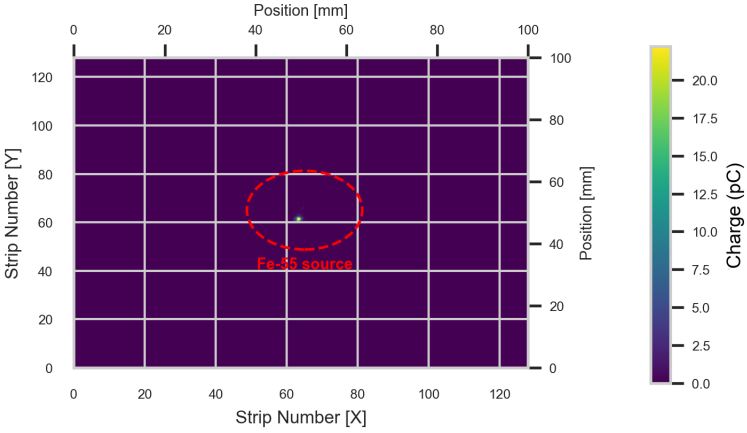

3260 V

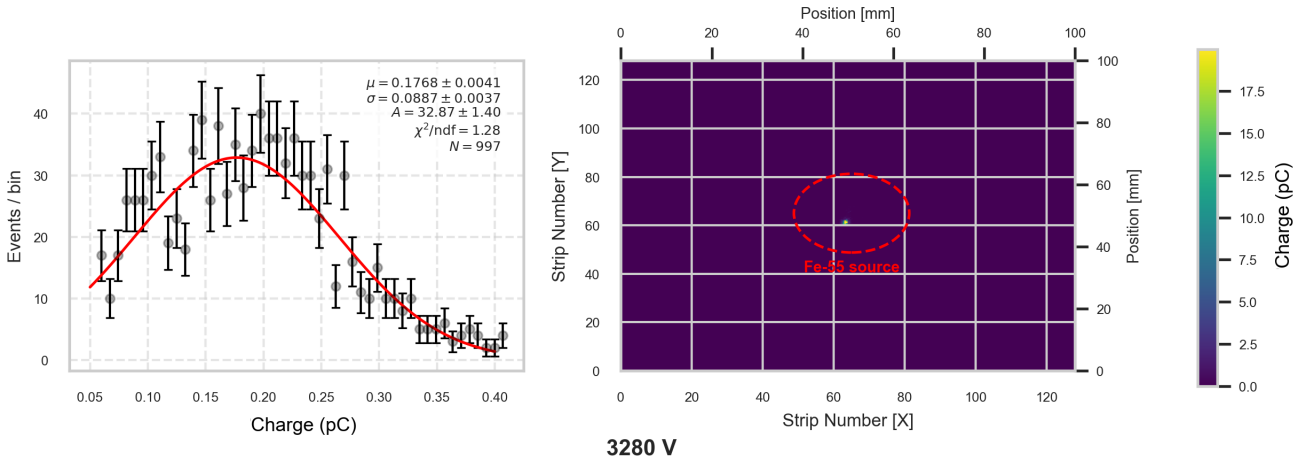

3280 V

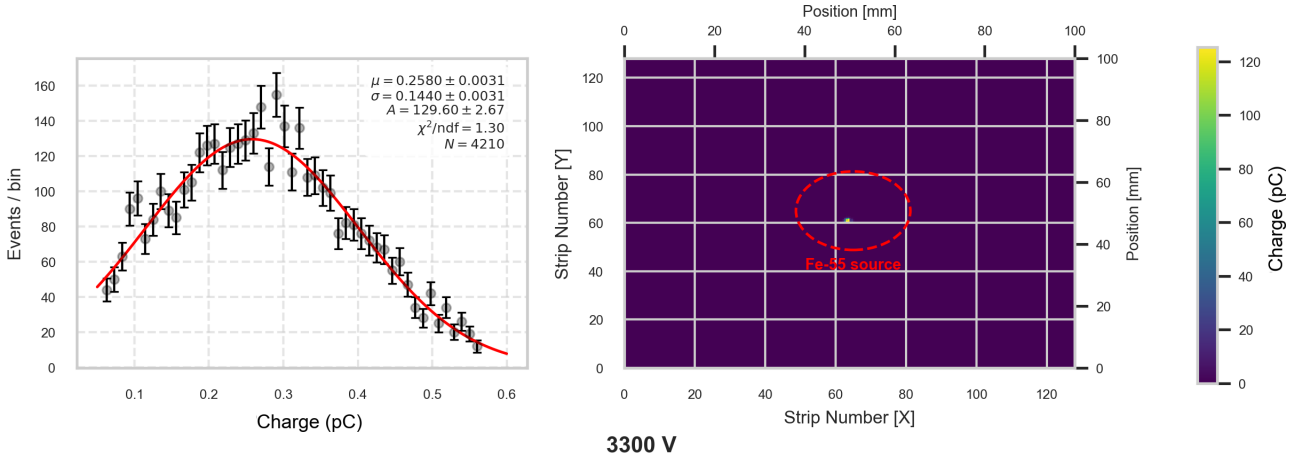

3300 V

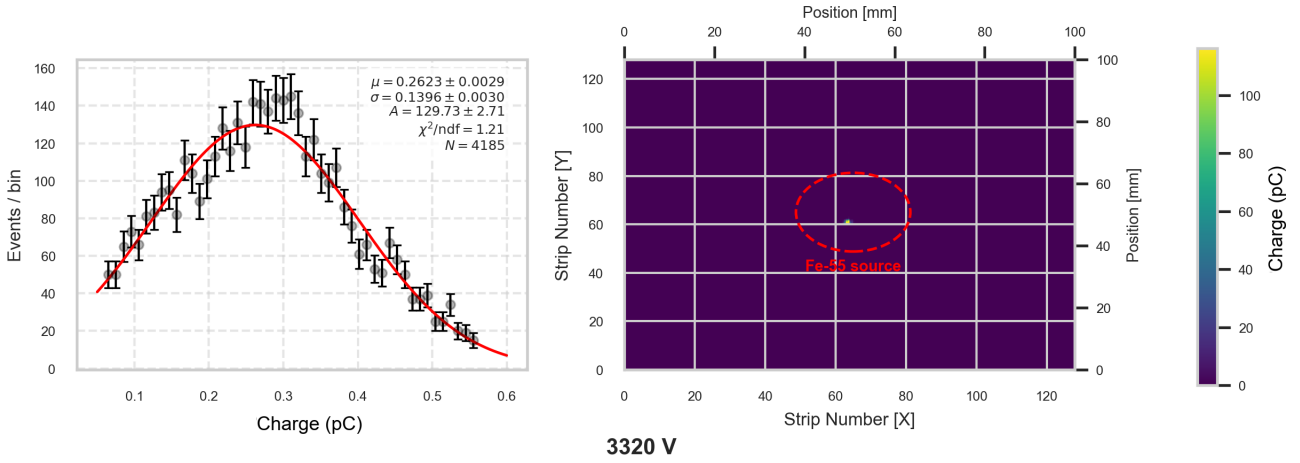

3320 V

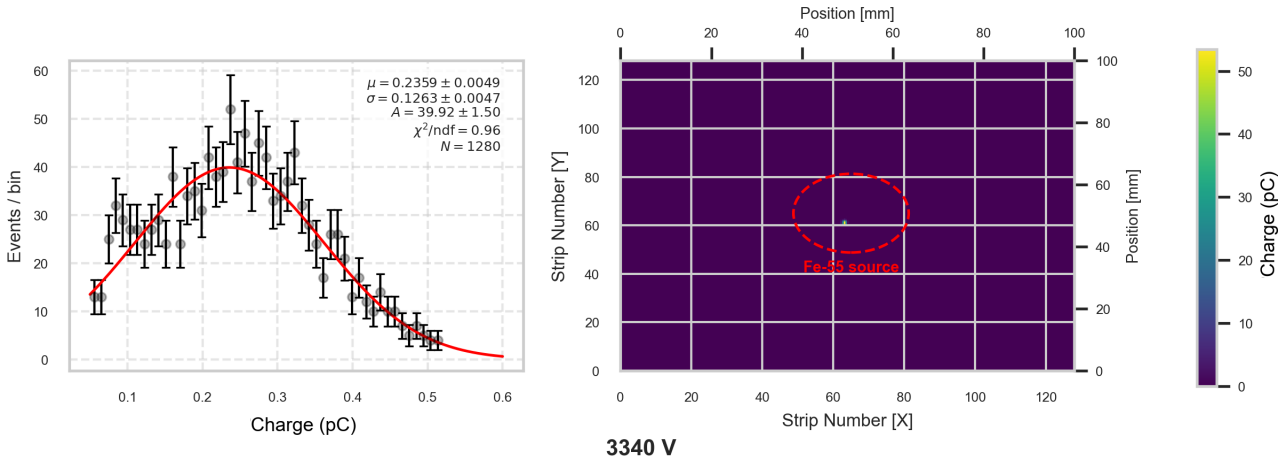
$\mu = 0.2359 \pm 0.0049$
$\sigma = 0.1263 \pm 0.0047$
$A = 39.92 \pm 1.50$
$\chi^2/\mathrm{ndf} = 0.96$
$N = 1280$
Events / bin
Charge (pC)
Position [mm]
Strip Number [Y]
Strip Number [X]
Position [mm]
Charge (pC)
Fe-55 source

3340 V

Appendix E

Spatial and Charge Distribution Maps of the GEM Stand Operated in the Proportional Region

E.0.1 3240 V

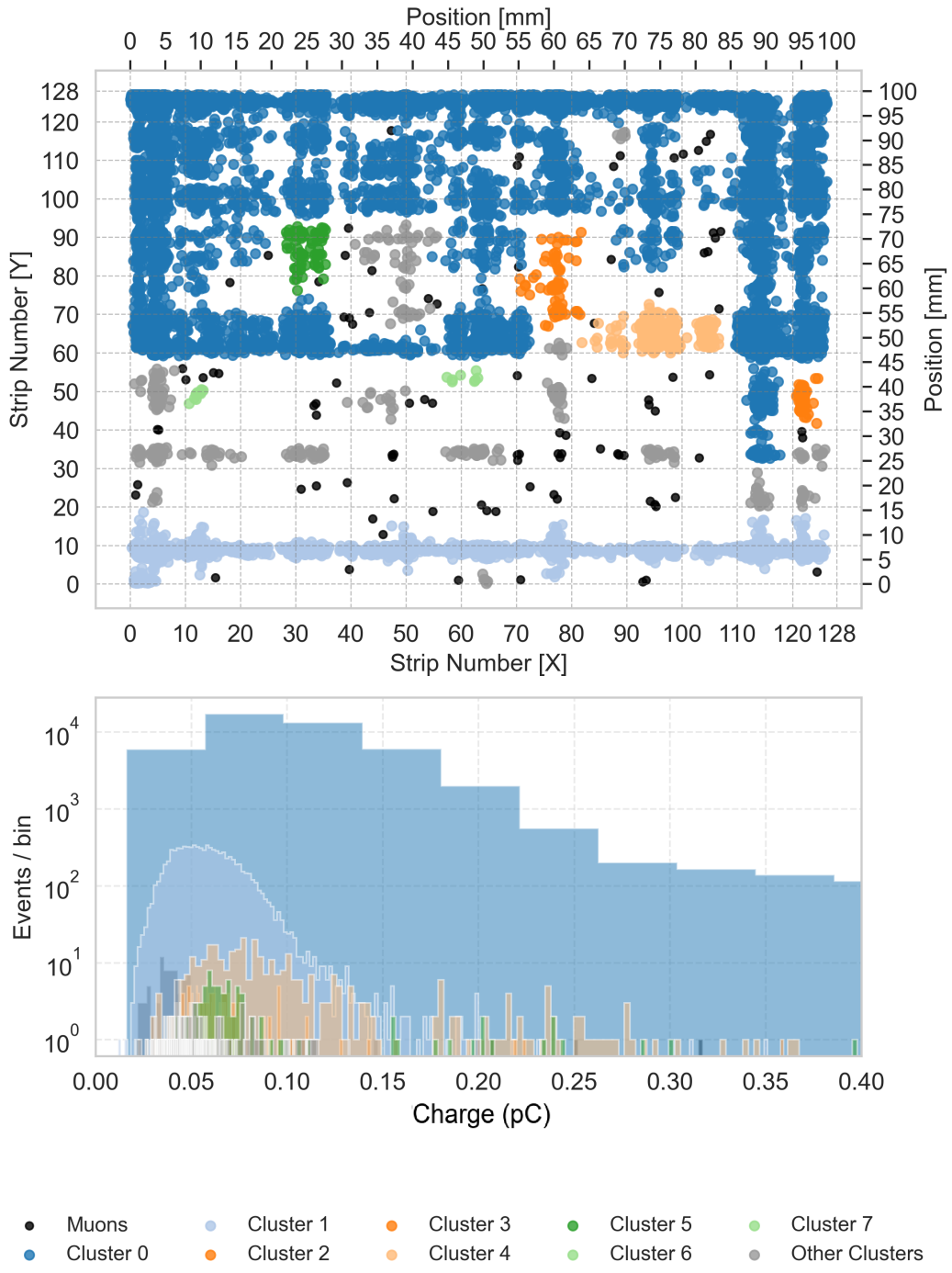

Figure E.1: Spatial and charge response of the **bottom triple-GEM** detector after applying the DBSCAN clustering algorithm. The spatial distribution shows the positions of identified clusters across the detector area, while the charge map represents the corresponding charge collected per cluster.

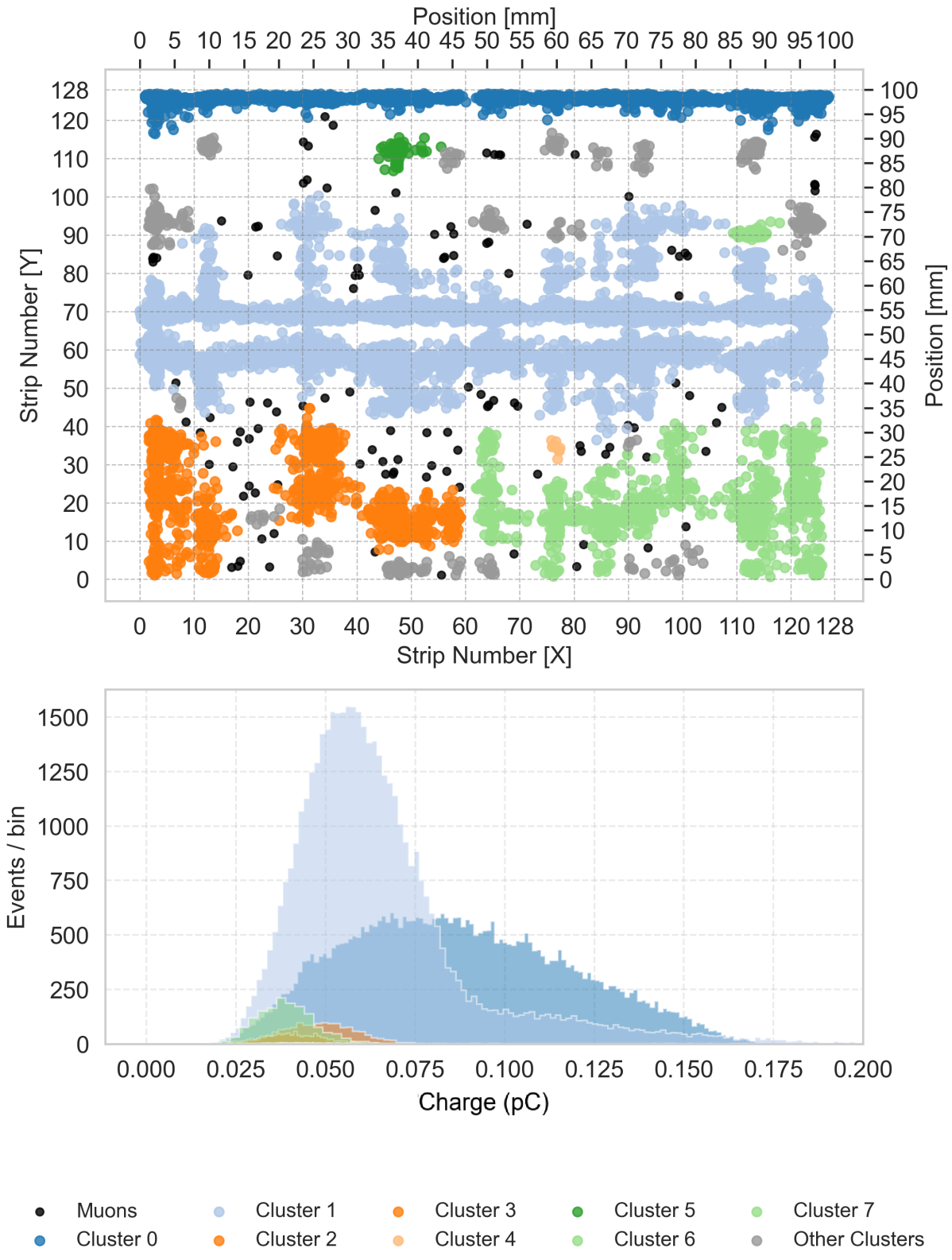

Figure E.2: Spatial and charge response of the **top triple-GEM** detector after applying the DBSCAN clustering algorithm. The spatial distribution shows the positions of identified clusters across the detector area, while the charge map represents the corresponding charge collected per cluster.

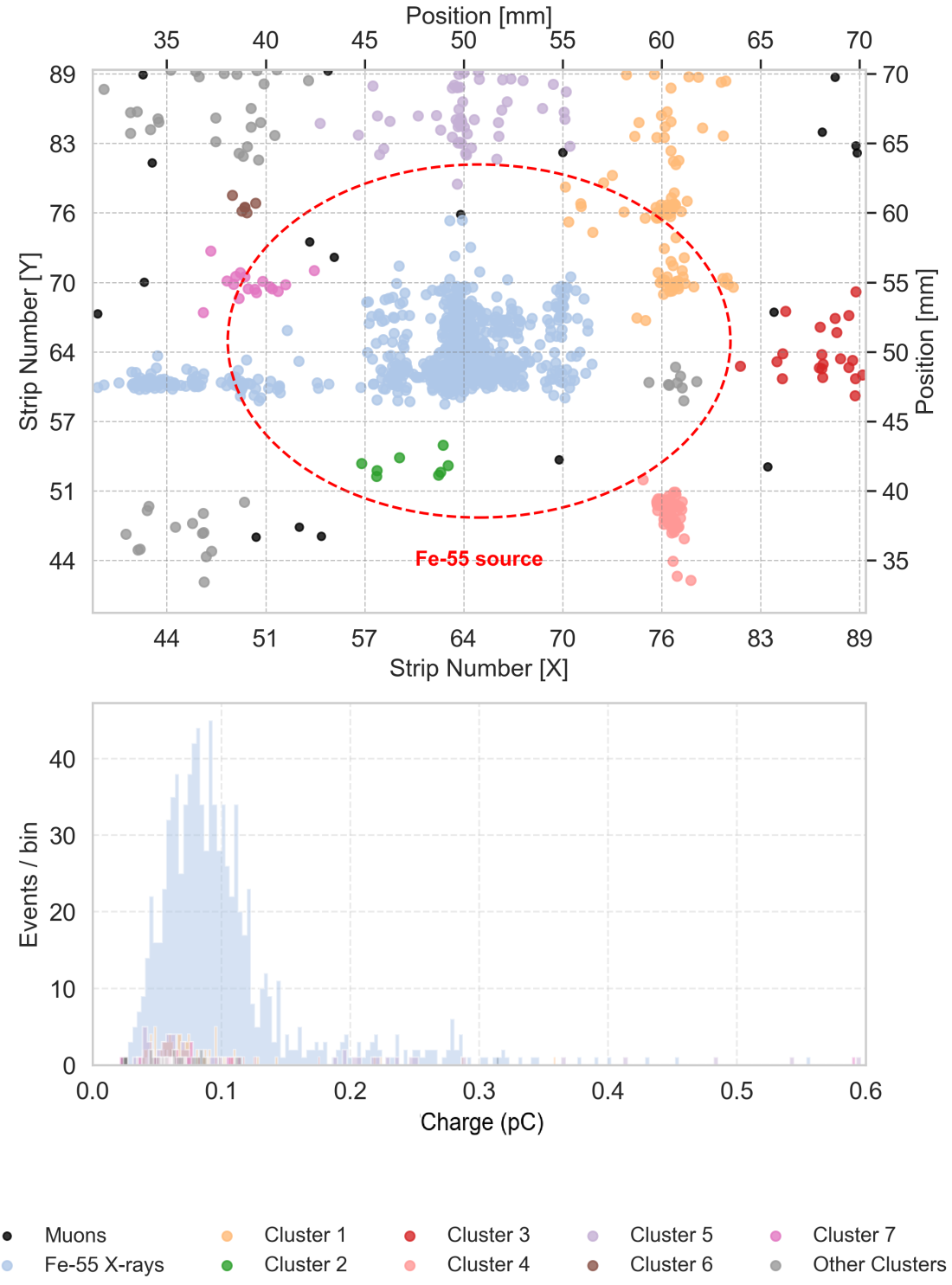

Figure E.3: Spatial and charge response of **the bottom triple-GEM** detector to Fe-55 X-rays, after DBSCAN clustering and the application of a fiducial cut. The red dotted circle marks the location of the Fe-55 source disk. The spatial distribution shows the positions of identified Fe-55 X-ray clusters and other events across the detector area, while the charge map represents the corresponding charge collected per cluster.

E.0.2 3260 V

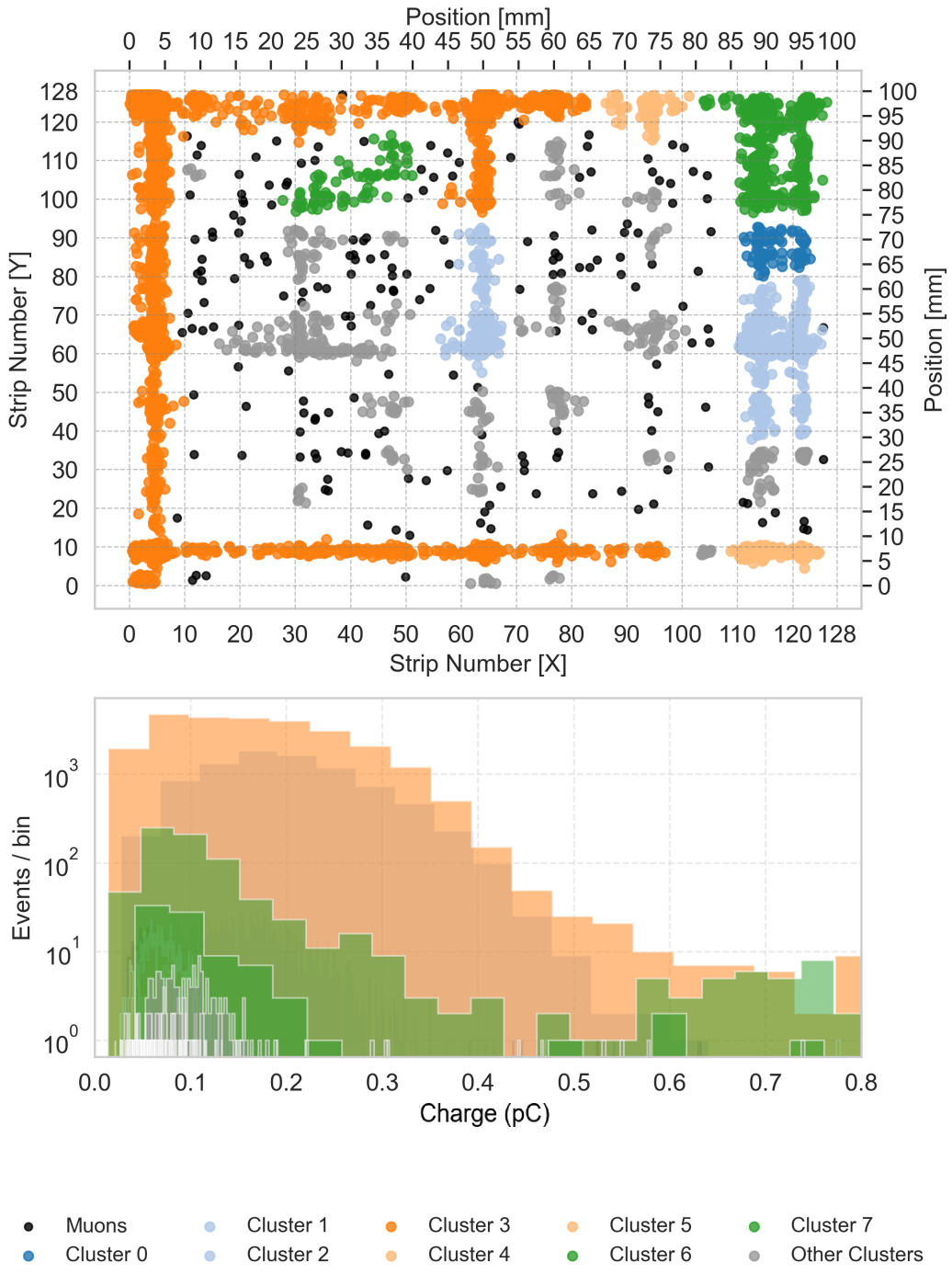

Figure E.4: Spatial and charge response of the **bottom triple-GEM** detector after applying the DBSCAN clustering algorithm. The spatial distribution shows the positions of identified clusters across the detector area, while the charge map represents the corresponding charge collected per cluster.

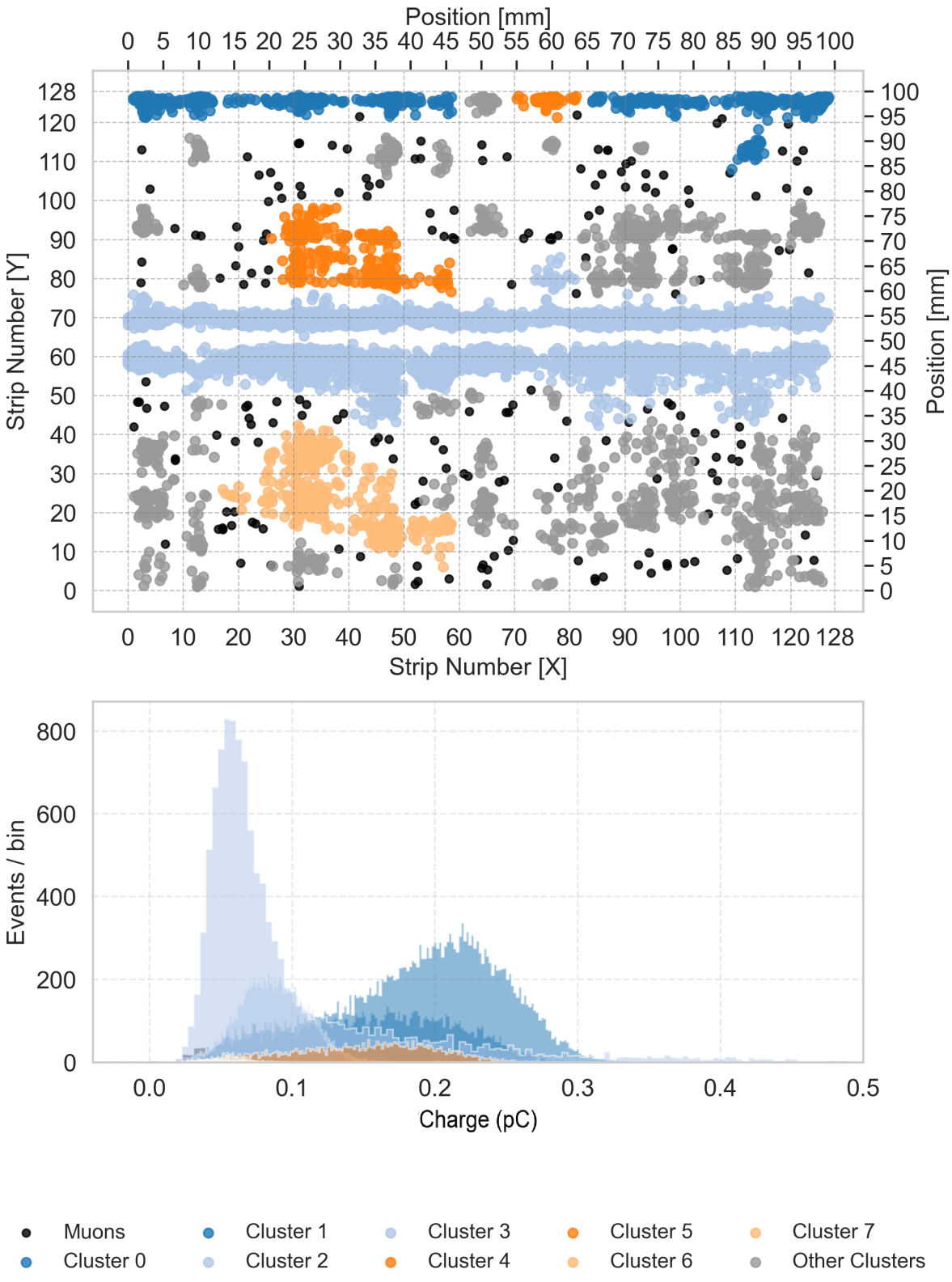

Figure E.5: Spatial and charge response of the **top triple-GEM** detector after applying the DBSCAN clustering algorithm. The spatial distribution shows the positions of identified clusters across the detector area, while the charge map represents the corresponding charge collected per cluster.

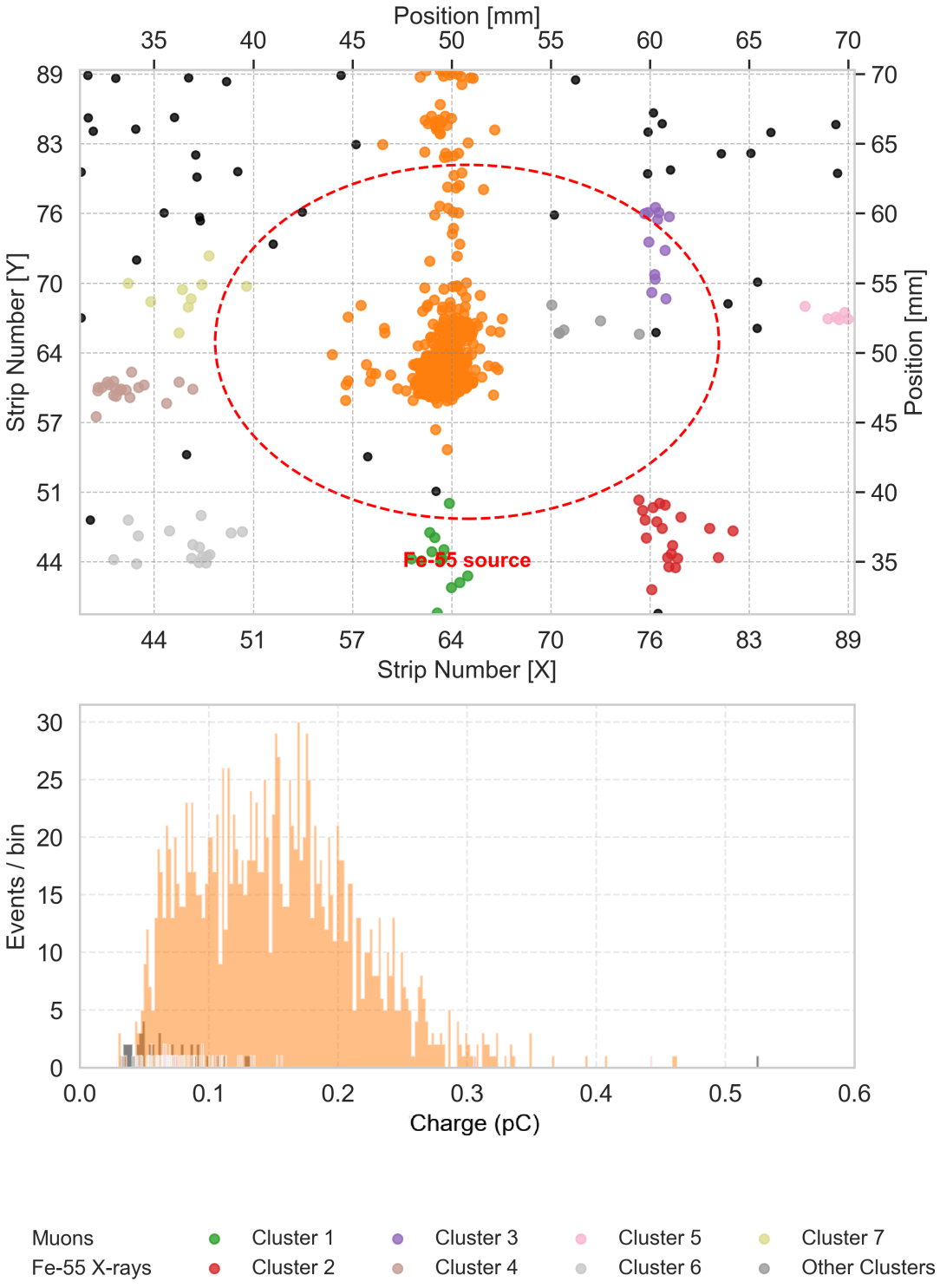

Figure E.6: Spatial and charge response of the **bottom triple-GEM** detector to Fe-55 X-rays, after DBSCAN clustering and the application of a fiducial cut. The red dotted circle marks the location of the Fe-55 source disk. The spatial distribution shows the positions of identified Fe-55 X-ray clusters and other events across the detector area, while the charge map represents the corresponding charge collected per cluster.

E.0.3 3280 V

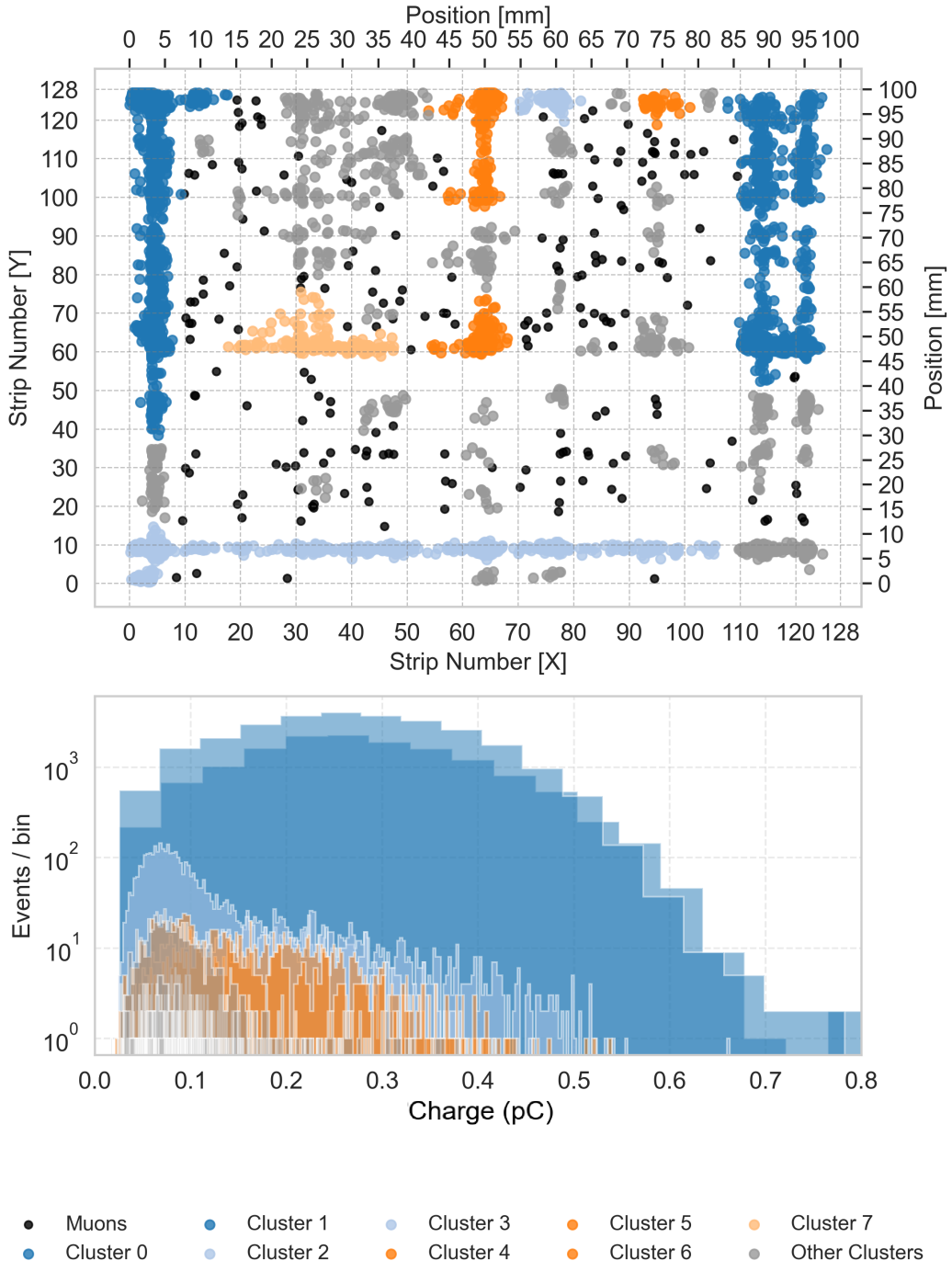

Figure E.7: Spatial and charge response of the **bottom triple-GEM** detector after applying the DBSCAN clustering algorithm. The spatial distribution shows the positions of identified clusters across the detector area, while the charge map represents the corresponding charge collected per cluster.

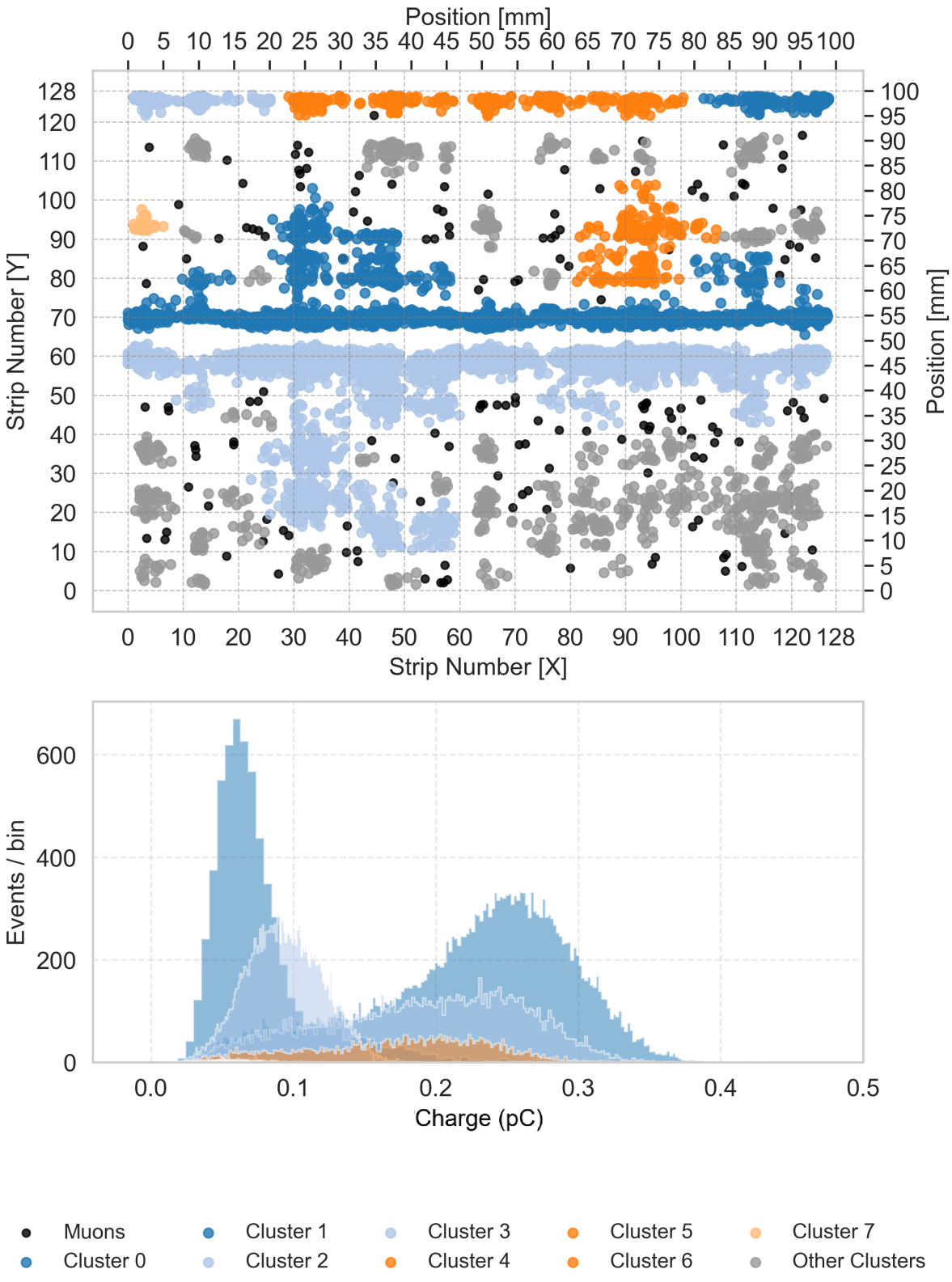

Figure E.8: Spatial and charge response of the **top triple-GEM** detector after applying the DBSCAN clustering algorithm. The spatial distribution shows the positions of identified clusters across the detector area, while the charge map represents the corresponding charge collected per cluster.

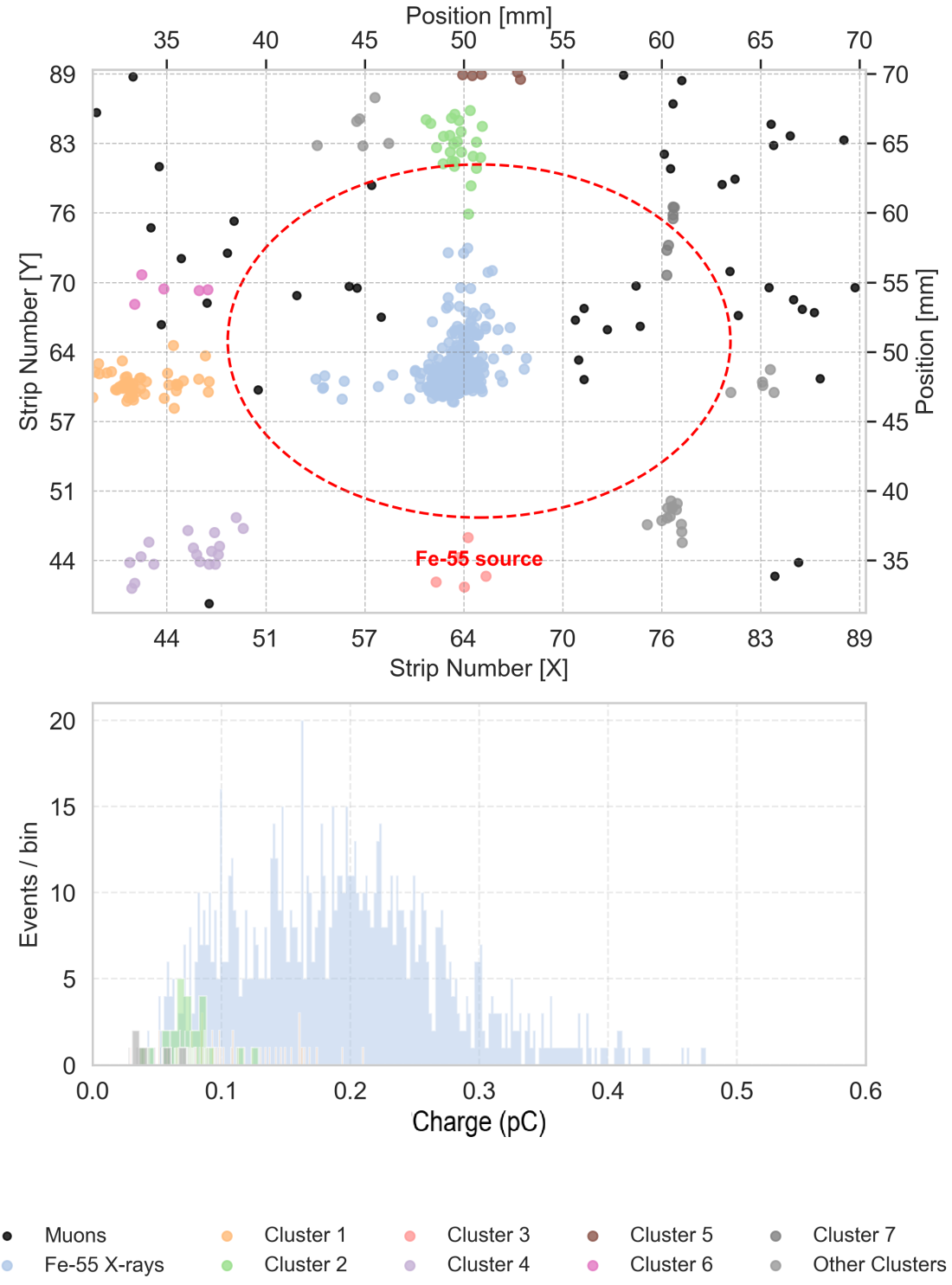

Figure E.9: Spatial and charge response of the **bottom triple-GEM** detector to Fe-55 X-rays, after DBSCAN clustering and the application of a fiducial cut. The red dotted circle marks the location of the Fe-55 source disk. The spatial distribution shows the positions of identified Fe-55 X-ray clusters and other events across the detector area, while the charge map represents the corresponding charge collected per cluster.

E.0.4 3300 V

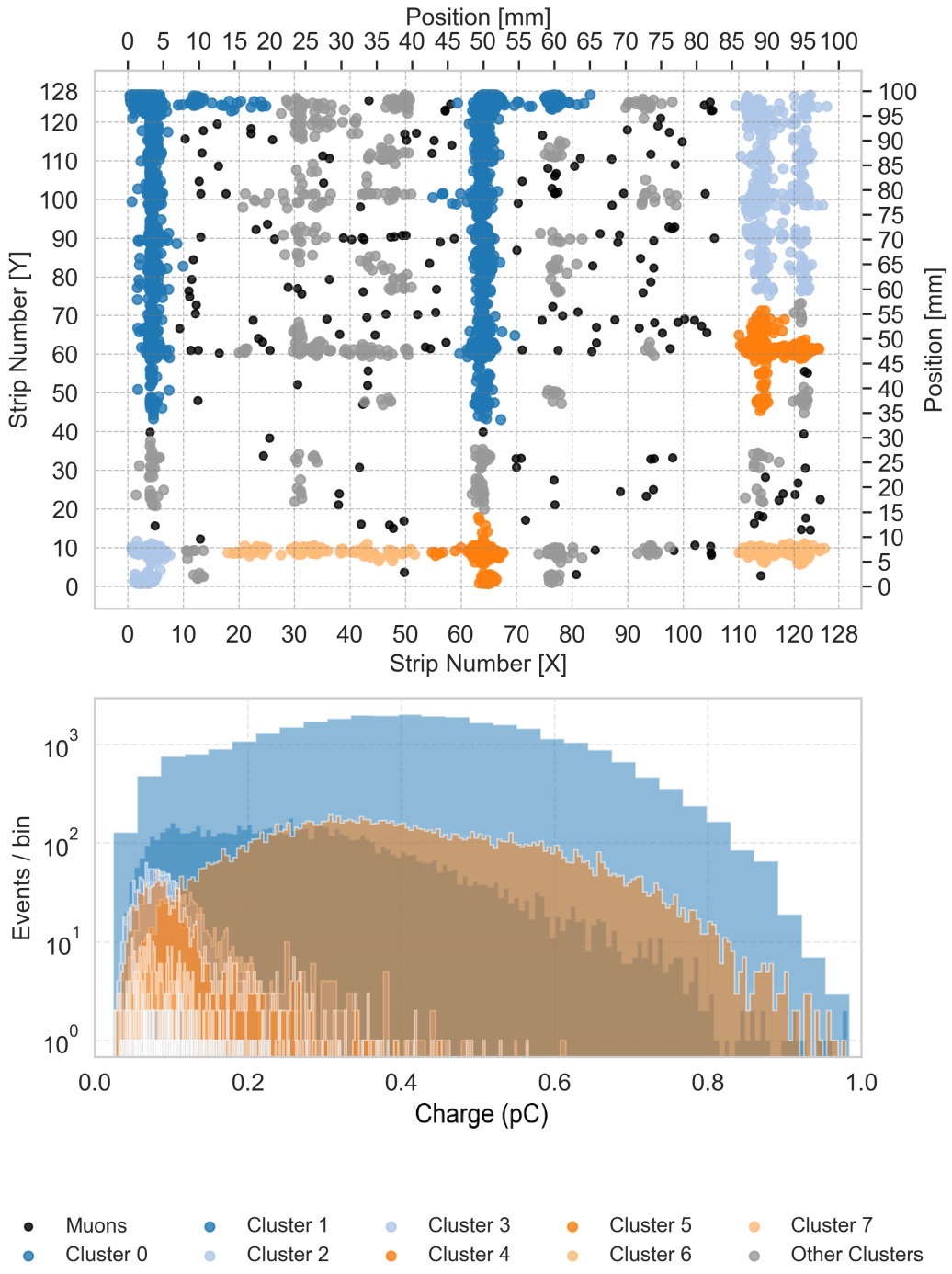

Figure E.10: Spatial and charge response of the **bottom triple-GEM** detector after applying the DBSCAN clustering algorithm. The spatial distribution shows the positions of identified clusters across the detector area, while the charge map represents the corresponding charge collected per cluster.

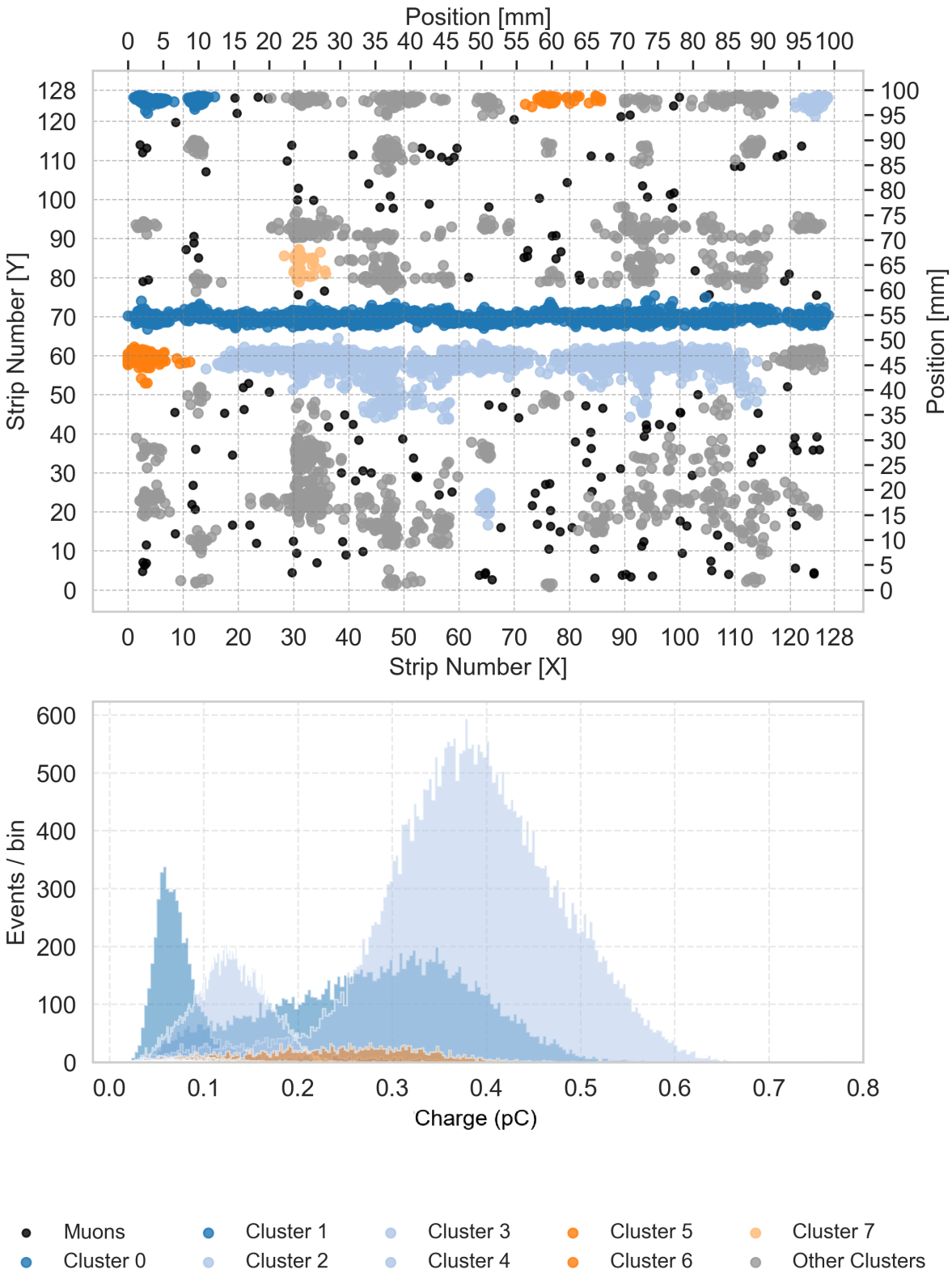

Figure E.11: Spatial and charge response of the **top triple-GEM** detector after applying the DBSCAN clustering algorithm. The spatial distribution shows the positions of identified clusters across the detector area, while the charge map represents the corresponding charge collected per cluster.

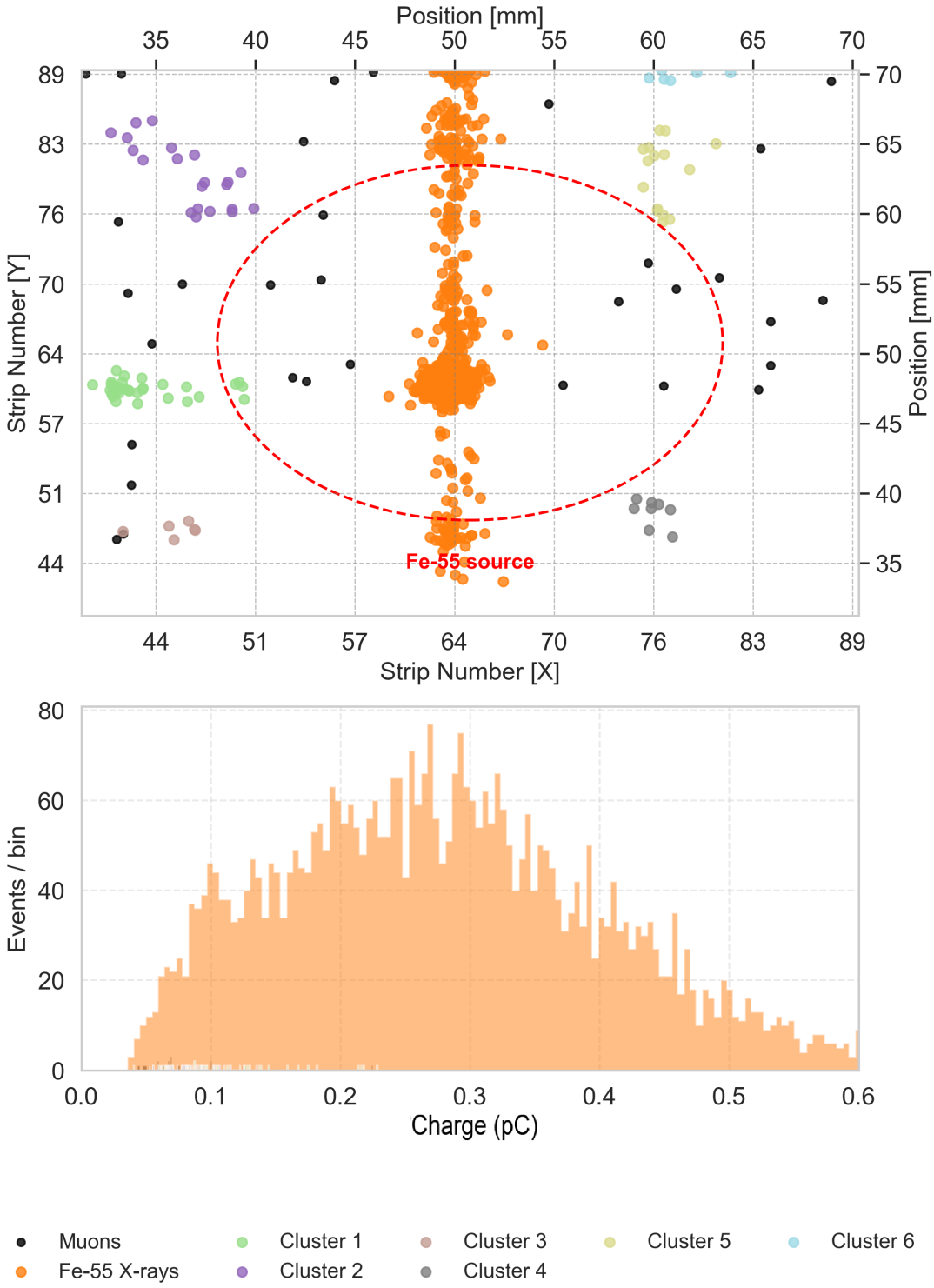

Figure E.12: Spatial and charge response of the **bottom triple-GEM** detector to Fe-55 X-rays, after DBSCAN clustering and the application of a fiducial cut. The red dotted circle marks the location of the Fe-55 source disk. The spatial distribution shows the positions of identified Fe-55 X-ray clusters and other events across the detector area, while the charge map represents the corresponding charge collected per cluster.